COMPUTATIONAL STUDY OF TRAILING-EDGE

GEOMETRY ON INLET GUIDE VANE FORCED

RESPONSE IN A TRANSONIC COMPRESSOR

By

ROBERT PHILLIP DARBE

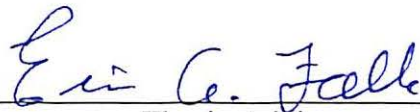Bachelor of Science

Oklahoma State University

Stillwater, Oklahoma

2002

COMPUTATIONAL STUDY OF TRAILING-EDGE

GEOMETRY ON INLET GUIDE VANE FORCED

RESPONSE IN A TRANSONIC COMPRESSOR

Thesis Approved:

_____
Thesis Advisor

_____

_____

_____
Dean of the Graduate College

ACKNOWLEGMENTS

TABLE OF CONTENTS

LIST OF TABLES

LIST OF FIGURES

NOMENCLATURE

Symbols

θ =   circumferential angle

θ_{BP} =   Circumferential angle between vanes/blades

$\Delta p'$ =   differential unsteady pressure

Δs =   axial grid spacing

Δt =   tangential grid spacing

η =   isotropic efficiency

c_r =   rotor chord

c_v =   vane chord

f =   frequency

f_{BP} =   blade passing frequency

i   =   axial grid index

j   =   radial grid index

k   =   circumferential grid index

LE   =   leading edge

M_{REL} =   relative Mach number

od =   outer diameter

p =   static pressure

P =   time-averaged static pressure

p' = unsteady static pressure

p_l' = lower-surface unsteady static pressure

P_t = time-averaged total pressure

p_t = total pressure

$P_{t,i}$ = area-time-averaged total pressure at the IGV inlet

p_u' = upper-surface unsteady static pressure

r = radial location

T = blade passing period

t_{BP} = time for one blade passing

TE = trailing edge

x = axial location

Acronyms

CFD = computational fluid dynamics

IGV = inlet guide vane

RANS = Reynolds-averaged Navier-Stokes equations

RPM = revolutions per minute

1 INTRODUCTION

Unsteady aerodynamic forcing of compressor blade rows is of significant interest in the jet engine and turbomachinery communities. For this reason, this thesis investigates rearward aerodynamic forcing of a vane row induced by a downstream transonic rotor.

1.1 OVERVIEW OF TURBINE ENGINE OPERATION

In aerospace applications, gas turbine engines provide one form of air breathing propulsion. The overall goal of such engines is to produce a maximum amount of thrust while keeping engine size and weight to a minimum. Engine thrust is achieved through two mechanisms: fluid acceleration through the engine, causing greater engine exit velocities than inlet velocities; and positive differential pressure change between the engine inlet and outlet. To foster these two mechanisms, gas turbine engines are comprised of a number of components. Typical components include: 1) an inlet to reduce the velocity of the air entering the compressor; 2) a compressor to increase the total enthalpy of the incoming air, facilitating combustion efficiency and power extraction; 3) a burner to promote fuel-air mixing and combustion processes releasing energy into the working fluid; 4) a turbine to extract energy from the working fluid for the purpose of driving the compressor and auxiliary components; 5) a nozzle to allow fluid expansion, increasing flow exit velocity. The present investigation focuses on axial-flow compressors.

1.2 COMPRESSOR DESIGN INTENT

Axial compressors are composed of a number of rotating blades for the purpose of turning and transferring energy to the passing fluid via work addition. This work addition process accomplishes a desired total enthalpy rise through the compressor. A set of rotating blades in a single row is referred to here as a blade row. A set of stationary vanes may lead, or follow, each blade row with the intent of increasing the fluid static enthalpy and directing the fluid in a specific direction; that direction typically satisfying the needs of the following blade row. A single row of stationary vanes is referred to here as a vane row. In modern engine designs, the total enthalpy rise achieved through a compressor requires several stages of blade and vane rows, each stage providing a portion of the overall thermodynamic change.

Given design goals to decrease engine size and weight, compressor size and weight is also of critical importance. A reduced number of compressor stages and decreased axial distance between stages helps accomplish this goal. However, a reduced number of compressor stages requires an increase in the time-averaged aerodynamic loading, or work, each stage must perform to produce the desired total enthalpy rise. In addition, decreasing stage-to-stage axial spacing leads to greater aerodynamic interactions between vane/blade rows. Such aerodynamic interactions come in the form of propagating fluid dynamic disturbances, or perturbations, caused by relative motion between rotor-blade and stator-vane rows. Such disturbances are unsteady, but periodic due the periodicity of the relative motion.

Unsteady disturbances in the aerodynamic field between rotor-blade and stator-vane rows occur in both the inertial and rotating reference frames (Fleeter, 1992 and

Kielb, 1992). These disturbances are both vortical and potential in nature, taking the form of convective wakes, tip-clearance vortices, hub-induced secondary flows, acoustically propagating pressure waves, and shocks. Depending on their type, such disturbances propagate upstream and downstream in the field, causing unsteady aerodynamic forcing, or unsteady loading, of the surrounding rotor-blade and stator-vane components in the form of surface-integrated unsteady lift, drag, and moment oscillations (Fleeter, 1992). Unsteady aerodynamic forcing of compressor blades and vanes results in dynamic stresses in the component structure. These stresses are periodic, or alternating, due to the periodic nature of rotor rotation and blade passing.

If aerodynamically induced alternating stresses possess certain amplitude and frequency characteristics, structural fatigue may occur within one or more compressor blades/vanes, increasing the possibility of crack initiation, crack propagation, and catastrophic failure. Fatigue is a process of cumulative damage to a structure caused by repeated load fluctuations, or stresses (Barsom, 1987). Fatigue occurs in regions where the structure plastically deforms under applied loads. Thus, a structure undergoing purely elastic stressing in the macro-domain must experience localized stress amplification in the micro-domain for fatigue to occur. In this case, the amplified micro-domain stresses must exceed the yield stress of the structural material. Prolonged exposure to stresses exceeding the yield stress can initiate and propagate a crack in the plastically deformed region. As a crack propagates to larger sizes, the chances for component catastrophic fracture increase.

Aerodynamically induced load fluctuations in modern compressors composed of high-strength blades and vanes are designed to produce purely elastic alternating stresses.

3

However, the occurrence of random material defects, foreign object damage (FOD), or blade-disk contact fretting can amplify stresses in the micro-domain, providing the proper conditions for crack initiation and propagation. Nonetheless, the number of aerodynamically induced load fluctuations typically required to form a crack within a compressor blade/vane is quite large. Thus, the cumulative structural damage process is often referred to as high-cycle fatigue (HCF). Despite current HCF-resistant design trends, continuing fatigue-related incidents make understanding and predicting compressor HCF important to the turbomachinery community.

1.3   IMPORTANCE OF HCF TO ENGINE COMMUNITY

High-cycle fatigue is of utmost importance in current compressor designs. As such, considerable amounts of experimental and computational research have been conducted for the purpose of predicting rotor and stator HCF failure. Nonetheless, HCF failures continue to occur in modern compressors. In fact, HCF failure presents a major readiness and monetary concern for both the U.S. Air Force and U.S. Navy (Fecke, 1998) where as much as 50% of all engine failures are related to component HCF. HCF-related problems are the leading cause of military engine failure, costing the U.S. government approximately $400 million per year (Garrison, 2001).

In an attempt to overcome reoccurring HCF problems in military engines, the U.S. Department of Defense established the National Turbine Engine High Cycle Fatigue Program in 1994. The goal of this ongoing program is to develop, implement, and validate damage tolerant design methodologies in order to avoid HCF-related engine failures. This is to be accomplished by increasing the level of understanding regarding HCF physics, as well as through the development of better HCF predictive capabilities.

4

1.4 PHYSICAL CONTRIBUTORS TO HCF

Compressor HCF is a direct result of modal forcing of rotor-blade and stator-vane rows, caused by unsteady aerodynamic loading. Improper prediction of either structural or aerodynamic characteristics of a blade/vane row may lead to incorrect HCF prediction. Unsteady aerodynamic forcing develops from disturbances propagating within the stage through-flow. Some of these unsteady disturbances are attributed to viscous, or vortical, wakes convecting downstream from upstream vane/blade rows. These wake disturbances directly impact all downstream components, causing what is referred to here as forward forcing, because the forcing stems from an upstream vane/blade row. For example, a rotating blade row behind a stationary vane row is subjected to a periodically unsteady flow as it passes through the vane wake regions. The periodically changing flow induces a change in the relative angle-of-attack for each rotating blade, causing periodic oscillations in blade aerodynamic loading.

Although the effects of propagating wake disturbances are of first-order importance to HCF, other non-wake-induced disturbances have been found to be just as important (Falk, 2000). For example, the presence of a rotor blade in an otherwise subsonic uniform throughflow causes fluid perturbations, or streamline curvature, around the blade. Such perturbations are denoted here as potential disturbances. In the rotating reference frame, rotor-induced potential disturbances are steady relative to the blade. In the absolute frame, however, rotor-induced potential disturbances rotate with the rotor and their presence is felt upstream and downstream at acoustic propagation speeds. Therefore, adjacent vane rows, in either upstream or downstream directions, experience periodic aerodynamic forcing from propagating potential disturbances. In transonic

flows, rotor-induced bow shocks develop in the rotating reference frame. In the absolute frame, these shocks represent upstream-propagating, rotating, periodic, potential disturbances that may aerodynamically force an upstream vane row; i.e., rearward forcing. In both subsonic and transonic flows, potential disturbances decay exponentially with distance, although the rate of decay depends on the disturbance strength (i.e., shock or subsonic pressure wave), acoustic speed, and rotor rotational speed (Falk, 2000).

With both downstream and upstream propagating disturbances, the flow inside a single compressor stage is unsteady, periodic in nature, and highly complicated. These unsteady aerodynamics lead to periodic unsteady loading of structural components in each stage. Thus, both blade and vane rows are subjected to periodic force and moment oscillations and alternating stresses. These alternating stresses are a main contributor to HCF.

1.5   CURRENT HCF-RELATED AERODYNAMIC PREDICTION CAPABILITIES

Current blade/vane forced-response predictions are limited by their applicability and accuracy. For example, contemporary numerical predictions of rotor and stator force-response often compare poorly with experimental data (Thompson, 1998). It has been purposed that discrepancies between computational and experimental data sets may be attributed to inaccurate models of aerodynamic forcing functions found in modern high-speed engines; existing models are often based and validated on classical analytical methods and low-speed experimental results (Fecke, 1998). Recently, however, a limited number of researchers have suggested existing data discrepancies may be accredited to previously ignored flow physics present in experimental data, but not modeled correctly

by computational algorithms. Such flow physics may have been considered second-order in past engine designs, due to slower throughflow speeds and more rudimentary flow considerations, but now are of first-order importance to the HCF problem.

Of particular concern is that of rearward forcing; i.e., upstream vane/blade row forced by disturbances emanating from a downstream row. Rearward forcing may account for some inaccuracies in existing aerodynamic forcing models. Recent compressor design trends include higher stage aerodynamic loading, smaller stage-to-stage axial spacing, and higher throughflow speeds. Decreased axial spacing promotes higher amplitude potential disturbance interaction with upstream vanes. This coupled with higher stage loading, increases aerodynamic forcing, possibly accelerating component HCF. With higher throughflow speeds, stronger shocks also develop amplifying potential disturbance forcing (Falk et al., 2003). Because of these design trends, the flow physics related to upstream propagating potential disturbance forcing may be under-predicted, possibly accelerating component HCF.

1.6 SCOPE OF CURRENT INVESTIGATION

The current research effort seeks to investigate aerodynamic forcing functions within a modern transonic compressor stage. A single vane/blade stage is numerically simulated and aerodynamic rearward forcing of the vane row by the rotor is analyzed, with particular interest paid to trailing edge and spanwise forcing phenomena. For these simulations, flow conditions in the Stage Matching Investigation (SMI) rig located at Wright Patterson Air Force Base (WPAFB) are replicated using the computational algorithm, MSU-TURBO.

2 PREVIOUS WORK

This chapter reviews previous rearward-forcing experiments and computational investigations. The intent is to establish the importance of rearward forcing to HCF and the continued need for the current research.

2.1 LITERARY REVIEW

Several experimental and computational investigations have attempted to understand the influence of aerodynamic forcing functions emitted by a downstream rotor on an upstream vane. For example, Sanders et al. experimentally observed rotor-induced pressure fluctuation on an upstream vane having a sharp trailing edge and non-zero time-averaged aerodynamic loading in the Purdue Transonic Multistage Research Compressor. The examined compressor allowed the investigation of unsteady inlet guide vane (IGV) and rotor aerodynamic interactions at several compressor-operating conditions, including both transonic and subsonic flows. The effects of varying axial spacing between the IGV and rotor-blade rows were also considered. Measurements were collected with embedded pressure transducers mounted axially along the suction surface of one vane and the pressure surface of an adjacent vane, at 90% span (Sanders et al., 1998).

The effects of increasing IGV-rotor axial spacing for both transonic and subsonic loading conditions resulted in a decrease in measured IGV static-pressure amplitude; pressure amplitude decay with increased spacing was more pronounced in the subsonic case. Overall, IGV unsteady aerodynamic loading was approximately six times larger for the transonic case than the subsonic case. This forcing difference was attributed to

increased nonlinear fluid-structure interactions caused by high levels of pressure unsteadiness generated by passing rotor shocks in the transonic case (Sanders et al., 1998).

Nonlinear fluid-structure interactions in the transonic case were also found to produce several higher-order harmonics in the IGV unsteady surface pressure, reaching as much as nine times the blade passing-frequency. These higher-order harmonics were not observed in the corresponding IGV aerodynamic forcing function, suggesting that the harmonics were caused by IGV-rotor nonlinear interactions. For the subsonic case, vane surface-pressure response was primarily related to the first-harmonic frequency, diminishing the role of nonlinear fluid-structure interactions at subsonic rotor operating conditions (Sanders et al., 2000).

Sanders et al. also reported IGV pressure-surface and suction-surface pressures to be nearly 180 degrees out of phase along most of the IGV chord. This was argued partially to be result of periodic rotor-shock impact on the IGV trailing edge, causing the IGV suction surface to reflect the shock while the pressure surface diffracted the shock (Sanders et al., 1999). As the initial shock propagated upstream through the IGV passage, reflected shock segments also propagated upstream and migrated toward the adjacent IGV pressure surface (Sanders et al., 2000), causing the observed phase difference.

Falk et al. and Kirk et al. examined IGV-rotor aerodynamic interactions by employing a Honeywell F109 turbofan engine with a single IGV installed forward of the axial single-stage fan. The examined IGV was characterized by a sharp trailing edge with no time-averaged aerodynamic loading. The vane was instrumented with eight

embedded pressure transducers in an attempt to capture the IGV unsteady surface-pressure phase and amplitude response at several rotor RPM.

The unsteady velocity field upstream of the rotor, in the absence of an IGV, was also measured, showing the IGV unsteady forcing function to be nearly sinusoidal and containing little spectral content beyond the first harmonic (Falk et al., 2000). In response to this forcing function, IGV pressure response measured on the IGV upper surface exhibited significant harmonic content. It was hypothesized that additional surface-pressure harmonic content, above that of the measured forcing function, could be attributed, in part, to a second potential disturbance (above that induced by the nominal rotor potential field). This second disturbance develops from rotor blades passing through the IGV wake, creating a stationary potential disturbance source. This stationary source created disturbances that propagated upstream through the IGV wake (Kirk et al., 2000), and across the IGV surface. Therefore, pressure response measured on the IGV upper surface resulted from a combination of rotating and stationary disturbances created by the rotor and IGV-wake rotor interaction, respectively.

A consistent phase difference observed between the pressures measured on the IGV upper and lower surfaces was justified via the argument that the two hypothesized potential disturbances, rotating and stationary, propagated at different phase velocities (Kirk et al., 2000). The phase on the IGV upper surface had characteristics similar to a previous velocity-field study (Falk, 2000), corresponding to disturbances produced by a rotating source.

IGV upper-surface pressures were also observed to increase exponentially with increasing rotor RPM, while lower-surface pressure amplification with RPM was less

pronounced (Falk et al., 2001). The pressure difference between the IGV upper and lower surfaces was attributed to the upper surface being directly impacted by the rotating rotor-induced disturbance field, while the lower surface was not directly impacted by these disturbances. The effect of disturbance impact on the IGV upper surface was to add additional dynamic pressure to the vane response, causing non-zero differential pressure across the vane. Corresponding to the amplitude difference between the IGV upper and lower surfaces, unsteady differential pressure across the IGV exhibited significant amplitude. As such, the vane experienced significant unsteady aerodynamic loading dependent on chord and rotor RPM (Falk et al., 2001).

At Wright Patterson Air Force Base, the Stage Matching Investigation (SMI) Rig in the Compressor Aero Research Laboratory allows transonic IGV-rotor aeromechanic investigations. The SMI rig consists of an IGV row followed by a transonic rotor and downstream stator row. The IGV row is characterized by blunt trailing-edge geometry and no time-averaged aerodynamic loading. The blunt-trailing-edge vane was designed to produce losses typical of those found in embedded stages of a modern jet engine compressor. The SMI facility has been employed for a number of different unsteady forcing experiments. The first HCF-related experiments examined the effects of the IGV-rotor axial separation, varied between "far", "mid", and "close" spacings (i.e., axial gaps of 56%, 26%, and 12% IGV chord, respectively). In these experiments, surface-pressure measurements were collected at two spanwise locations along an instrumented IGV, at both subsonic (Probasco et al., 1997) and transonic (Probasco et al, 1998) flow conditions. At both conditions, axial IGV-rotor spacing had a noticeable influence on

vane forced-response; IGV surface-pressure amplitude increased as axial separation decreased. The same effect was also reported by Sanders et al. (2000).

To aid understanding of phenomena observed in the transonic experiments, results from a computational fluid dynamic (CFD) analysis were compared to the experimental results (Probasco et al., 2000 and Koch et al., 2000). The CFD code Vane/Blade Interaction (VBI), which solves the full Navier-Stokes equations coupled with a Baldwin-Lomax turbulence model in two dimensions, was employed for this purpose. Numerical results exhibited similar harmonic content, as well as rotor-shock interaction, near the IGV trailing edge when compared to experimental results; however, the numerical results over-predicted rotor-shock strength. Using the VBI program, the effects of stage backpressure were also observed. Increasing stage backpressure at constant rotor speed increased bow-shock influence on IGV forcing amplitude (Probasco et al., 2000).

In following investigations, Gorrell et al. used the SMI rig to examine IGV-rotor axial-spacing influences on stage mass-flow capacity, total pressure ratio, and isentropic efficiency (Gorrell et al., 2002a). A rake of total pressure and total temperature probes were placed 93% rotor chords downstream of the rotor. Axial-spacing differences between the IGV and rotor imparted significant changes in stage performance; stage-mass-flow capacity, total pressure ratio, and isentropic efficiency all decreased as IGV-rotor axial distance was reduced. The effect IGV-row solidity was also considered, showing higher solidity to result in lower stage performance.

To assist the interpretation of mechanisms leading to the observed stage performance reductions with reduced IGV-rotor axial spacing, the CFD algorithm MSU-TURBO (Version 4.1) was employed (Gorrell et al., 2002b). This three-dimensional,

time-accurate CFD code solves the Reynolds-averaged Navier-Stokes (RANS) equations in a rotating reference frame. An implicit finite-volume algorithm using the k-ε turbulence model was applied. Simulation results showed at close IGV-rotor axial spacing rotor-induced bow shocks split at the IGV trailing edge as the shock propagated upstream. This shock "chopping" caused the oblique shock produced by the rotor to turn normal relative to the IGV. The normal shock moved upstream approximately orthogonal to IGV time-averaged flow, increasing entropy production and pressure loss across the shock. In the far IGV-rotor spacing configuration, the rotor bow shock degenerated into a pressure wave before reaching the IGV trailing edge. Therefore, no normal shock developed on the IGV that might cause performance loss (Gorrell et al., 2002b).

Fabian et al. used a compressible-flow cascade facility to investigate rearward forcing of a vane row, characterized by aerodynamically loaded vanes having sharp trailing edges. Vane unsteady forcing was created by von Karman vortex shedding from a set of circular cylinders placed downstream of the cascade. The forcing disturbances were potential in nature, and propagated upstream at acoustic speeds through the vane row (Fabian et al., 2001). Measured vane surface-pressure amplitudes at the first-harmonic disturbance frequency suggested the vane might experience a trailing-edge pressure singularity, similar to that observed at the leading edge when interacting with a downstream-propagating disturbance. This finding implied rearward-forced vanes might not conform to traditional notions of the Kutta condition; i.e., zero differential pressure at the trailing edge. Instrumentation restrictions, however, only allowed surface-pressure

measurements between 7% - 80% vane chord (Fabian et al., 2001), disallowing definitive surface-pressure measurements directly at the vane trailing edge.

2.2 SUMMARY OF REVIEW

Each of the aforementioned experiments agrees on certain generalities about the effects of upstream-propagating potential disturbances on vane rearward forcing. In all cases, as IGV-rotor axial spacing decreases, unsteady aerodynamic interactions increase. Furthermore, disturbances in transonic flow (i.e. shocks) have a greater effect on unsteady forcing magnitudes when compared to subsonic cases; however, all cases exhibit non-trivial vane-loading amplitudes. It is also generally agreed that as upstream propagating disturbances interact with an IGV, higher surface pressures are induced on the IGV surface facing into the rotor rotation direction. Significant unsteady pressure harmonic content also occurs toward the IGV trailing edge in the aforementioned cases; however, Sanders et al. (2000) observed higher-order harmonic content (above the blade-passing frequency) only for transonic flow regimes. Differential-pressure was found to have the most significant amplitudes near the IGV trailing edge, decreasing with upstream distance along the vane.

Unfortunately, not all results agree so nicely. Disagreement focused on the production of IGV surface-pressure harmonics in subsonic flows. Sanders and Fleeter reported only first-harmonic content in such cases, while Kirk et al. and Probasco et al. reported higher-order harmonic content to be present. Another area of disagreement relates to the phase shift in unsteady surface-pressure between the IGV lower and upper surfaces. Sanders and Fleeter attributed this phase shift to shock reflection and

diffraction near the IGV trailing edge, while Kirk et al. hypothesized a second stationary potential disturbance caused by the rotor as it cuts the IGV wake.

2.3   UNRESOLVED ISSUES

The aforementioned investigations provide essential improvements toward understanding rearward forcing in transonic compressors; however, several important aspects of the forcing environment remain unexamined. For example, Probasco et al. and Gorrell et al. each considered an IGV row having blunt-trailing-edge vanes, rather than the standard sharp-trailing-edge geometry. The influence of a blunt trailing edge on IGV forcing is unknown, but may be important as such profiles produce wakes via base drag. Modern, highly loaded, low-aspect-ratio, compressor blades primarily generate wakes through diffusion, not base drag. The effects of base drag on a body commute upstream in a subsonic flow, suggesting that wake unsteadiness caused by IGV-rotor interactions may create surface-pressure fluctuations not otherwise present on a sharp-trailing-edge geometry (McCormick, 1995). Falk and Darbe previously conducted two-dimensional RANS simulations of blunt-trailing-edge IGV interactions with a transonic rotor, finding blunt vanes to produce significant trailing-edge pressure amplification as compared to corresponding sharp-IGV profiles (Falk et al., 2003).

In addition to trailing-edge geometry, few investigations have examined IGV spanwise forcing in transonic compressors. Probasco et al. and Koch et al. considered span in their transonic IGV-rotor investigations, showing significant spanwise dependence; however, only two span locations were examined with no corresponding forcing-function information (Probasco et al, 2000, and Koch et al., 2000). A study by Koch et al. measured spanwise IGV-rotor characteristics in the same compressor, but

focused primarily on rotor forcing functions (Koch et al., 2000). Beyond span, the effects of IGV wake character on rotor potential fields (i.e., IGV forcing functions) have received minimal attention, likely due to the complexity of the IGV-rotor aerodynamic environment. Finally, a definitive investigation of IGV trailing-edge pressure "singularities" caused by rearward forcing, as first proposed by Fabian et al., has yet to be conducted (Fabian et al., 1999 and Fabian et al., 2000). Falk and Darbe disputed the existence of such pressure singularities; however, their evidence was based on two-dimensional RANS simulations conducted on a rotor not designed to support an IGV row (Falk et al., 2003).

2.4   CURRENT CONTRIBUTIONS

Given the apparent need for continued rearward-forcing examination, the current investigation employs three-dimensional, time-accurate, RANS simulations to study IGV trailing-edge geometry and IGV-rotor spacing influences on IGV forcing in a highly loaded transonic compressor at design speed. All simulations utilize the parallel, multi-block, computational flow-solver MSU-TURBO. The computations simulate conditions through the IGV-rotor stage in the Air Force Research Laboratory (AFRL) SMI rig, with the addition of a sharp-trailing-edge IGV geometry.

Preliminary results indicate: (1) IGV trailing-edge geometry significantly influences time-averaged IGV wake character, IGV chordwise forcing, and IGV spanwise forcing; (2) increased IGV-rotor axial spacing reduces IGV forcing amplitude, but also alters spanwise IGV forcing.

3 COMPUTATIONAL METHODOLOGY AND SETUP

This chapter details the methodology and setup employed in the current numerical investigation. In particular, it describes the SMI rig. A description of the computational algorithm MSU-TURBO is also given, followed by a discussion of the parameters specified for the computational grid and boundary conditions.

3.1 SMI RIG DESCRIPTION

The SMI rig is a 1.5-stage, high-speed, highly loaded compressor consisting of IGV, rotor-blade, and stator-vane rows. The intent of the test article is to simulate the second stage of a highly loaded, transonic, military core compressor, where impingent wakes from a fictitious upstream first stage are developed from a specially designed IGV, or wake generator, row. The rig possesses capabilities to simulate three IGV-rotor axial spacings, as well as three IGV counts (12, 24, and 40 vanes). For the present investigation, only far and close axial spacings are considered, with IGV and rotor-blade of counts of 24 and 33, respectively. The far IGV-rotor axial spacing represents a typical axial gap found in operational fans and compressors, while the close spacing corresponds to current design trends in high performance fans and compressors. The far and close axial spacings equal $0.56c_v$ and $0.12c_v$, respectively. Figure 3-1 provides a cut-away illustration of the SMI rig. Specific design parameters are given in Table 3-1.
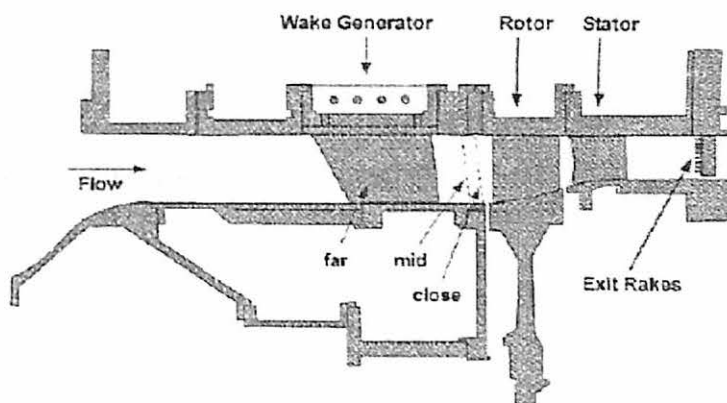
Figure 3-1 Cross-Sectional View of SMI Rig (Gorrell et al., 2001).

Table 3-1 SMI Aerodynamic Design Parameters (Gorrell et al., 2001).

Parameter	Blade Row
Number of Airfoils	33
Inlet hub/tip ratio	0.750
Flow/annulus Area	195.2991 kg/s/m^2
Flow/ unit area	85.4531 kg/s/m^2
Flow rate	15.6310 kg/s
Tip speed, corrected	341.3710 m/s
M_{REL} LE hub	0.963
M_{REL} LE tip	1.191
PR	1.880
η_{iso}	93.5%
LE tip diameter	0.4825 m (19 in)
LE hub diameter	0.3620 m (14.25 in)
TE tip diameter	0.4825 m (19 in)
TE hub diameter	0.3872 m (15.244 in)

The SMI rotor-blade row was designed by Law and Wennerstrom (1989). The SMI IGV row was designed to create a pressure loss coefficient consistent with modern, highly loaded, low-aspect-ratio fan and compressor front stages. In general, these wakes are turbulent and decay less rapidly than wakes from lightly loaded, high-aspect-ratio blade rows. The IGV design also attempted to reproduce two-dimensional wakes similar to those reported by Creason and Baghdadi (1988), allowing isolation and simplification of wake characteristics during experiments. To achieve a two-dimensional wake profile,

the vanes were designed as unloaded, uncambered, symmetric airfoils with a small leading edge and blunt trailing edge. This shape provides no flow turning, but creates wakes similar those of loaded upstream stages through base drag and no swirl. By increasing chord from hub to tip, a constant spanwise IGV solidity also minimizes loss and wake-width variability with vane span. Gorrell et al. (2001) details the blunt IGV design.
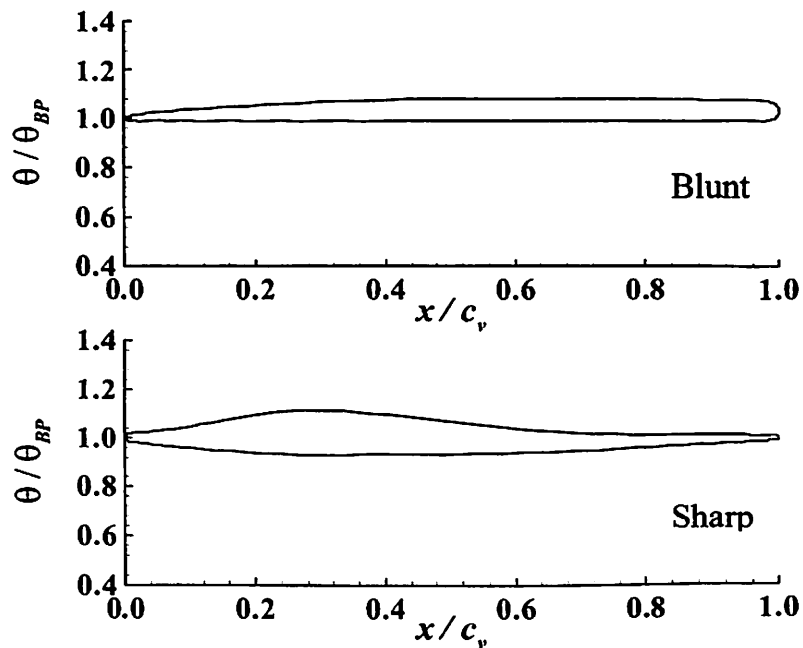
Figure 3-2 Blunt and Sharp IGV Profiles: 75% Span.

In addition to the blunt-trailing-edge IGV, a specially designed sharp-trailing-edge IGV is considered in this investigation. Figure 3-2 provides a two-dimensional representation of both blunt and sharp trailing-edge geometries at 75% span. The sharp IGV exhibits a large, non-symmetric, thickness increase from the leading edge to its maximum thickness location, causing rapid flow acceleration into each vane-row passage. Aft of the maximum thickness location, vane thickness decreases smoothly to a sharp trailing edge, resulting in an adverse pressure gradient through the passage.

19

Ensuing flow diffusion generates a wake. Wake generation via diffusion introduces no flow turning, consistent with the stage time-average flow design and velocity angles.

3.2 MSU-TURBO SOLVER DESCRIPTION

MSU-TURBO is an industry-capable three-dimensional flow solver developed specifically for unsteady turbomachinery analysis. MSU-TURBO solves the RANS equations in a rotating reference frame. The turbulence model MSU-TURBO utilizes was developed at the Center for Modeling of Turbulence and Transition (CMOTT), a focus group within the Institute for Computational Mechanics in Propulsion (ICOMP) at NASA Glenn Research Center. The CMOTT turbulence model employs a number of low Reynolds number k-ε eddy viscosity models, in addition to wall functions (Zhu et al., 1997), obviating the need for fine grid spacing near a wall to resolve viscous flow effects. The solution utilizes a second-order backward-difference time discretization and a third-order, characteristics-based, finite-volume spatial discretization. A modified flux-vector splitting technique properly transfers physical information throughout the flowfield, splitting the flux vector into two parts. Each part corresponds to a different characteristic direction; the upstream-propagating characteristic treated with a backward-difference discretization, and the downstream-propagating characteristic modeled with forward-difference discretization. The Beam and Warming technique (Beam and Warming, 1976) linearizes the conservative form of the nonlinear finite-volume governing equations by means of a Taylor series expansion of the spatial variables. An employed approximate factorization technique also arranges the finite-volume algorithm into tri-diagonal form, separating the three-dimensional equation system into three one-dimensional equations and solving for spatial derivatives in successive intermediate portions during a full time

step. Approximate factorization is similar to the alternating-direction-implicit (ADI) method described by Anderson (1995). Newton sub-iterations performed at each time step reduce linearization errors, where the Block-Jacobi symmetric Gauss-Seidel method is applied iteratively to solve each matrix "block" during a time-step. As used here, "block" indicates a three-dimensional tridiagonal matrix were all dependent variables are solved along three diagonals, one for each spatial dimension.

To allow for parallel processing, the solution domain is divided into sub domains, or partitions. Flow solutions in each partition are solved separately with one partition per processor, accomplished with single-program multiple-data (SPMD) parallelization. Under this strategy, a single algorithm is replicated on each processor, allowing more of the code from the previous serial version of MSU-TURBO to be usable for the parallel version (Chen et al., 2001). The parallel version uses Block-Jacobi updating of data at partition interface boundaries and symmetric Gauss-Seidel iterations within each partition (Chen et al., 2001). Bidirectional data exchange at partition interfaces occurs following each solution sub-iteration sweep. To maintain code portability across different parallel-computing platforms, a Message Passing Interface (MPI) library for interprocessor communications is employed (Chen et al., 2001).

A dynamic sliding-mesh model separates the stationary-vane and rotating-blade grid domain, since relative motion exists between them. This model uses phantom cells at the interface between blade rows, where fluid values in these cells are obtained by interpolation. The phantom cells create a data buffer ring containing a circumferential array of data related to each neighboring blade row (Chen et al., 2001). The values in the buffer ring are extracted to a data array and sent to the processor controlling the solution

in the neighboring partitions across the sliding-mesh interface. Data in the transferred array are then interpolated into the grid of the new partitions, thereby updating the partition inlet/outlet boundary conditions.

For a compressor containing an equal number of IGV and rotor blades, flow periodicity allows computational modeling of only one flow passage for each vane/blade row, respectively. When unequal vane/blade counts are present, however, computational simulations must model either the full annulus of vanes and blades, or a sector of the annulus containing the physical vane/blade count divided by the highest common denominator. For example, in its current configuration the SMI rig contains 24 inlet guide vanes and 33 rotor blades. As such, flow periodicity requires either modeling the full annulus containing 24/33 vanes/blades, or an annulus sector containing 8/11 vanes/blades (as 3 equals the highest common denominator between 24 and 33). Compressors containing unequal vane/blade counts therefore necessitate modeling significantly larger computational grids, drastically increasing computational expense.

Fortunately, phase-lagged boundary conditions available in MSU-TURBO allow modeling of compressors containing unequal vane/blade counts with only one flow passage per vane/blade row. In this case, different outlet/inlet areas will exist for each vane/blade row at the sliding-mesh interface. MSU-TURBO stores time-varying flow-history data at the sliding-mesh interface for each vane/blade row, where the amount of history MSU-TURBO retains is a user input. A sliding-mesh buffer ring is then constructed for each vane/blade row by extracting stored time-history data and interpolating it into the adjacent vane/blade row grid (Chen et al., 2001). Because of the data storage method, phase-lagged boundary conditions only approximate blade-row

interactions at the neighboring blade-passing frequencies and their harmonics, causing loss of flow information not related to blade-passing frequencies.

Standard pressure inlet and outlet boundary conditions are specified at the IGV inlet and rotor outlet, respectively, while wall boundary conditions are specified on the hub, casing, and vane/blade surfaces. Rotor tip clearance was modeled in all simulations as an open mesh with phase-lagged boundary conditions. The full physical clearance height and eight equally distributed radial grid points were used to model the tip-clearance gap.

3.3   COMPUTATIONAL GRID DESCRIPTION

3.3.1   Average Passage Grid (APG) software

The computational grids developed for the current investigation were created with Average Passage Grid (APG) software (Beach, 2003). APG was originally developed for grid generation used with CFD algorithm APNASA (Beach, 2003); however, MSU-TURBO can also employ APG grids. APG creates a structured H-type grid represented as a single, blade-passage centered, grid block. It employs user-defined geometry databases to create a two-dimensional axisymmetric (axial-radial) profile of the modeled blade rows. This axisymmetric grid is then rotated through the appropriate blade-row pitch to generate surfaces of revolution and eventually the final three-dimensional grid. During the grid generation process, the user controls grid density, grid distribution, sliding-mesh interface location, rotor-tip clearance properties, grid elliptical smoothing parameters, etc. These parameters are stored in text files that APG references during execution.

The grids simulated here utilize elliptically smoothing. Elliptically smoothing iteratively generates grid configurations possessing the least amount of skewed grid cells, thereby improving computational accuracy and convergence.

3.3.2 Grid Size, Grid Distribution, and Grid Dimension

Grid sizes employed in the current investigation are outlined in Table 3-2. The indices i, j, k represent the axial, radial, and circumferential directions, respectively. Table 3-3 shows corresponding grid distributions, where the tabulated Δs and Δt values represent grid spacing for the first grid point, at a specific location, in the axial and tangential directions, respectively. APG distributes grid points along each coordinate direction as successive ratios, matching end location spacings. Note that all grid points are non-dimensionalized by the outer-diameter of the SMI rig (0.4826 m).

Table 3-2 Grid Size Information.

Case	Grid Size	Leading Edge	Trailing Edge	Tip
Rotor	(i,j,k) = (189,71,81)	i = 19	i = 99	j = 63
IGV-Close	(i,j,k) = (138,71,61)	i = 31	i = 111	j = 71
IGV-Far	(i,j,k) = (190,71,61)	i = 23	i = 103	j = 71

Table 3-3 Grid Distribution Information.

Case	Δs Inlet	Δs Outlet	Δs LE	Δs TE	Δt Inlet	Δt Outlet
Rotor	0.05	0.05	0.002	0.002	0.005	0
IGV	0.05	0.05	0.002	0.002	0.01	0.0045

Table 3-4 contains physical dimensions related to the SMI geometry. Note that for the current case, the IGV-inlet, rotor-outlet, and IGV/rotor-casing (outer radius locations) are constant, while the rotor-hub radius and sliding-mesh interface locations change with axial position. In the present investigation, only one rotor grid was generated: this grid being used for all presented MSU-TURBO simulations. Conversely,

separate grids were created for the blunt-IGV and sharp-IGV configurations. The inputted grid parameter files employed for each case can be found in Appendix A. A proprietary code developed by Turner (2003) was used to shift the blunt-IGV and sharp-IGV grids to the appropriate far and close axial spacings. An example grid is illustrated in Figure 3-3, showing a two-dimensional cut at 75% spanwise location of the final blunt-IGV grid at the close-spacing condition.

Table 3-4 Grid Dimension Information.

Parameter	Value	
IGV-inlet location	$x/od =$	-0.225
Rotor-outlet location	$x/od =$	0.145
IGV-pitch	$\theta \quad =$	$15°$
Rotor-pitch	$\theta \quad =$	$10.909°$
IGV-hub radius	$r/od =$	0.375
Rotor-hub radius	Varies	
IGV-casing radius	$r/od =$	0.50
Rotor-casing radius	$r/od =$	0.50
Interface, 25% span location	$x/od =$	-0.0033
Interface, 50% span location	$x/od =$	-0.0041
Interface, 75% span location	$x/od =$	-0.0048

where, $od = 0.4826$ m
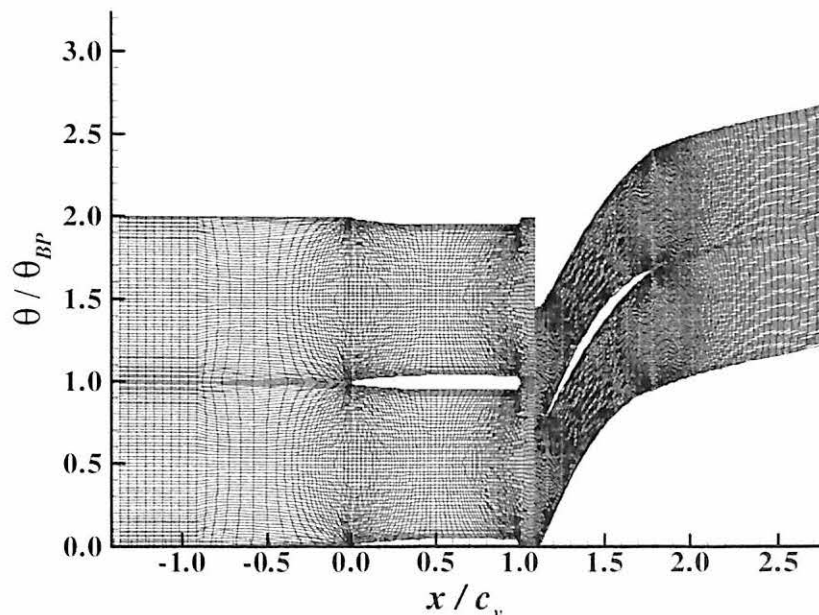
Figure 3-3 IGV-Rotor Grid: Blunt–Close, 75% Span.

No grid independence studies were performed in the current study; however, previous MSU-TURBO simulations conducted by Gorrell et al. (2001) used grids having nominal node distributions of 138×41×51 and 99×41×51 for the SMI far-spacing blunt-IGV and rotor geometries, respectively. These previous simulations adequately resolved the IGV unsteady forcing environment; therefore, grid distributions employed herein are considered sufficiently dense to achieve solution grid independence.

3.4   COMPUTATIONAL SETUP

All unsteady simulations were performed using 270 time steps per blade-passing period, with the rotor rotating at 13509 RPM. During each time step, six sub-iterations were performed to calculate dependent variables in the solution domain. Solution data corresponding to 100 time steps were stored for use in phase-lag boundary condition development. The computational domain was axially partitioned into 52 subdomains (e.g., 32-IGV and 20-rotor) for parallel processing. Computations were conducted on an IBM P3, scalable, distributed-memory parallel computer located in the Aeronautical Systems Center (ASC) Major Shared Resource Center (MSRC) at Wright-Patterson Air Force Base. Solutions were considered converged when inlet/outlet mass-flow rate and vane surface-pressure variations decreased below 0.1% of their respective steady-state values. Figure 3-4 illustrates mass-flow rate convergence history for the sharp-IGV at the close-spacing condition; this history is representative of all simulation conducted in this investigation. The area-averaged mass-flow rate at the inlet and outlet for both IGV and rotor grids are shown versus time-step iteration number. The mass-flow rate converges to around 15.5 k/m^3 between 20,000 and 25,000 iterations. The mass-flow rate at the rotor outlet periodically oscillates about the converged mass-flow rate value with constant

26

amplitude (i.e., periodic flow conditions are achieved). The sharp-IGV case approximately converged after 100 blade-passing periods. Each time-step required approximately 40 seconds to complete. Thus, the entire simulation required approximately 1.8 years to complete on an equivalent single processor.
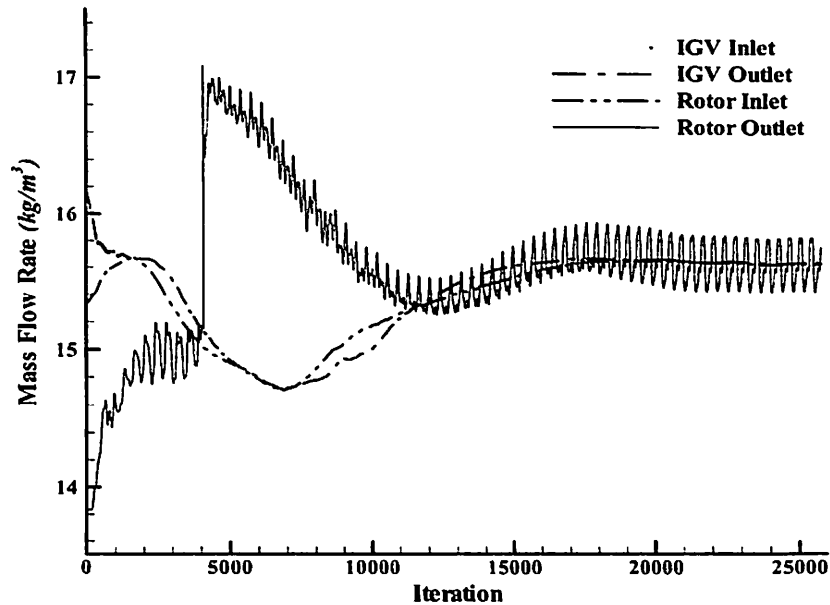
Figure 3-4 Convergence of Mass Flow Rate: Sharp-IGV, Close-Spacing.

3.4.1 Reference Values

During calculations, MSU-TURBO employs non-dimensionalized variables. All variables are non-dimensionalized using the reference values listed in Table 3-5.

Table 3-5 MSU-TURBO Reference Values.

Parameter	Value
Rotor Rotational Speed	1414.66 rad/s
Reference Pressure	101325.39 Pa
Reference Length (od)	0.4826 m
Reference Temperature	288.15 °K
Reference Velocity	287.60 m/s
Reference Gas Constant	287.04 N*m/kg*s
Gamma	1.40

3.4.2 Boundary Conditions

Inlet boundary conditions specified isentropic subsonic inflow with radial profiles of total pressure; all other inlet flow variables were held constant with radius. Total pressure values were specified at various spanwise locations, simulating hub and casing boundary-layer behavior. The employed inlet total-pressure profile versus percent span is illustrated in Figure 3-5. Outlet boundary conditions maintain radial equilibrium of characteristic flow variables for a subsonic outflow. Specific values for both the inlet and outlet boundary conditions are summarized in Table 3-6. Input text files used to control MSU-TURBO reference values and boundary conditions are provided in Appendix B.

Table 3-6 MSU-TURBO Boundary Conditions.

Parameter	Value
Inlet Boundary Conditions	
Total Temperature	288.15 °K
Turbulence Intensity	0.02
Turbulence Length Scale	0.001
Outlet Boundary Conditions	
Static Pressure	117243.3 Pa
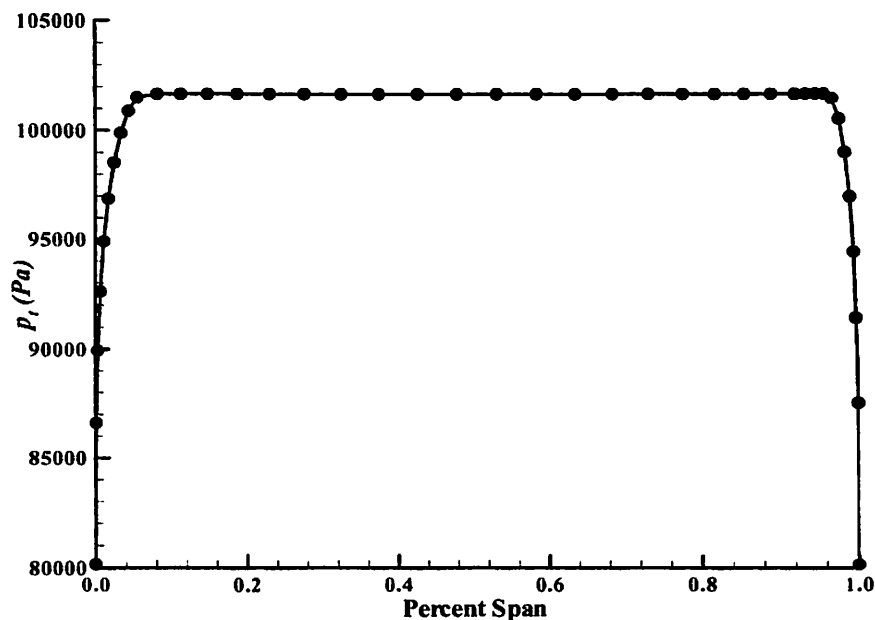
Figure 3-5 Inlet Total-Pressure Profile.

28

3.4.3 Operating Conditions

The stage mass-flow rates, total pressure and temperature ratios, and isentropic efficiencies for the four IGV-rotor cases investigated are listed in Table 3-7. Note that total pressure and total temperature ratio calculations are performed between the IGV-inlet and rotor-outlet locations.

Table 3-7 Operating Condition

Case	Mass Flow Rate (kg/s)	Total Pressure Ratio	Total Temperature Ratio	Efficiency, η (%)
Blunt-IGV, Far-Spacing	15.8	1.77	1.20	87.5
Blunt-IGV, Close-Spacing	15.7	1.77	1.20	87.2
Sharp-IGV, Far-Spacing	15.7	1.76	1.21	85.1
Sharp-IGV, Close-Spacing	15.6	1.75	1.20	86.1

3.5 REVIEW OF PREVIOUS MSU-TURBO PAPERS

MSU-TURBO has been previously employed by several researchers, including Gorrell et al. (2001), Turner (1996), Van Zante (1997), Barter et al. (1998), and Panovsky et al. (2000). Most notably, Gorrell et al. (2001) used MSU-TURBO to simulate the SMI rig, producing results accurately describing experimentally measured flow behavior. Barter et al. (1998) directly compared experimental results to MSU-TURBO simulations, generally finding good agreement between the two, while noting accurate rotor-blade surface-pressure magnitude and phase at the first-harmonic and second-harmonic frequencies. Van Zante (1997) found time-averaged MSU-TURBO simulation results to agree excellently with time-averaged experimental results, but computed higher vane-wake dissipation rates than those in corresponding experiments. Panovskey et al. (2000)

29

also compared experimental and MSU-TURBO results, concluding that MSU-TURBO predicted the measured three-dimensional flowfield with encouraging accuracy. These previous code validations attest to the relative accuracy of MSU-TURBO for the current time-accurate blade-row simulations.

4 TIME-AVERAGED FLOWFIELD RESULTS

This chapter explores various aspects of the time-averaged numerical results. The time-averaged flowfield represents an important aspect of the overall unsteady-forcing simulations for two reasons. First, unsteady results develop by subtracting the time-averaged flowfield from the instantaneous solution at each time step, thus giving a perturbation about the time-average field. Second, the time-averaged flow may be examined to determine if MSU-TURBO provides reasonable results, similar to that expected for flow through a transonic blade/vane row.

4.1   TIME-AVERAGING METHODOLOGY

The time-averaged flowfield for each simulation is computed by summing each flow parameter (i.e., velocity, pressure, etc.) at each grid location over 60 time steps (two blade-passing periods), respectively. The resulting summations are then divided by 60, giving an average value for each fluid parameter at each grid point. All pressure results shown herein are non-dimensionalized by $P_{t,i}$, the area-averaged total pressure calculated at the IGV inlet plane.

4.2   IGV TIME-AVERAGED STATIC-PRESSURE DISTRIBUTIONS

Figure 4-1 displays the time-averaged static pressure computed along the IGV chord for the far-spacing condition at 75% span, where the term "upper" denotes the vane upper surface (surface-normal direction opposes rotor rotational motion), and "lower" denotes the vane lower surface (surface-normal direction corresponds to rotor motion).

31
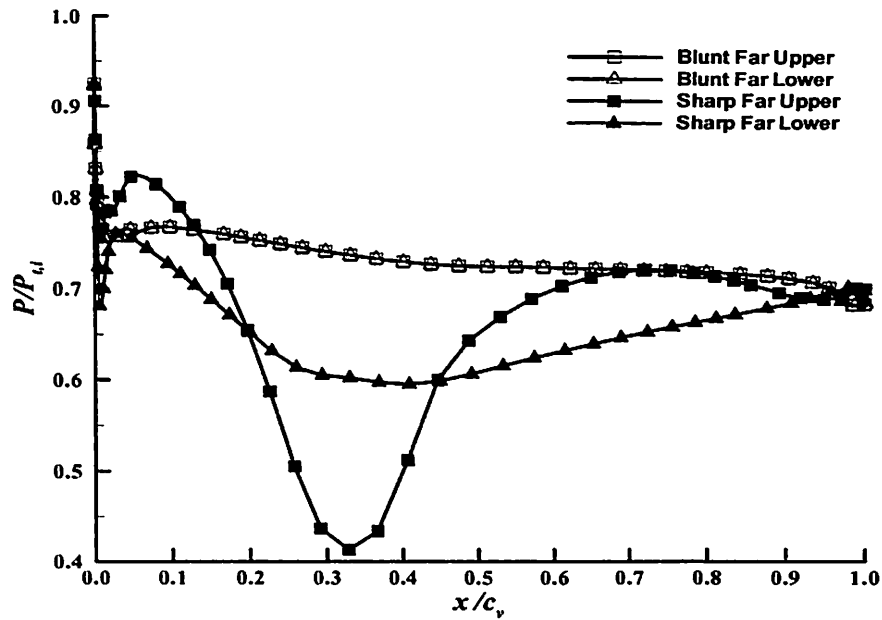
Figure 4-1 Time-Averaged IGV Static Pressure: Far-Spacing, 75% Span.

As expected, the symmetric blunt-IGV profile has equivalent time-averaged static pressure distributions on the upper and lower surfaces. Thus, the blunt IGV has no time-averaged aerodynamic loading. Conversely, the sharp IGV shows non-matching pressure distributions on the upper and lower surfaces, indicating an aerodynamically loaded vane, as expected. Both blunt and sharp IGV geometries exhibit zero time-averaged differential static pressure at the trailing edges, suggesting no evidence of a trailing-edge singularity, as proposed by Fabian et al. (2001). For the sharp IGV, static pressure distributions indicate fluid acceleration through the vane passage from approximately x/c_v = 0.0 - 0.3. At x/c_v = 0.3, however, the vane passage reaches its minimum throughflow area, beyond which the passage area increases causing a static pressure rise and fluid deceleration, or diffusion. This diffusion process leads to wake development on the sharp IGV, as discussed later.

32
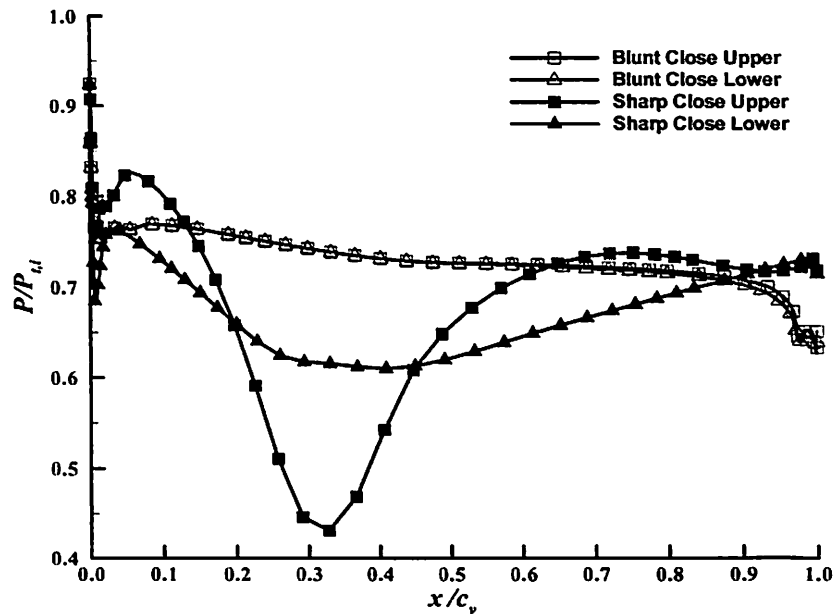
Figure 4-2 Time-Averaged IGV Static Pressure: Close-Spacing, 75% Span.

Figure 4-2 shows the time-averaged IGV static pressure distributions for the close-spacing condition at 75% span. Comparing Figure 4-1 and Figure 4-2, the only notable change may be observed at the blunt-IGV trailing edge. At this location, the time-averaged static pressure decreases significantly for the blunt-close IGV, indicating rapid flow acceleration not exhibited in the far-spacing data. This decrease in trailing-edge static pressure for the blunt IGV at close spacing is attributed to nonlinear fluid-structure interactions, as discussed below. The sharp IGV does not exhibit a significant difference in static pressure distribution between the two axial spacings.

Figure 4-3 and Figure 4-4 show time-averaged static pressure contours for the blunt-IGV and sharp-IGV geometries at the far-spacing condition, respectively. The symmetry of the static pressure distribution for the blunt IGV, and non-symmetric distribution for the sharp IGV, may be easily seen. Again, note the minimal static pressure change through the blunt-IGV passage, as compared to the sharp-IGV geometry showing a dramatic pressure drop near $x/c_v = 0.3$.
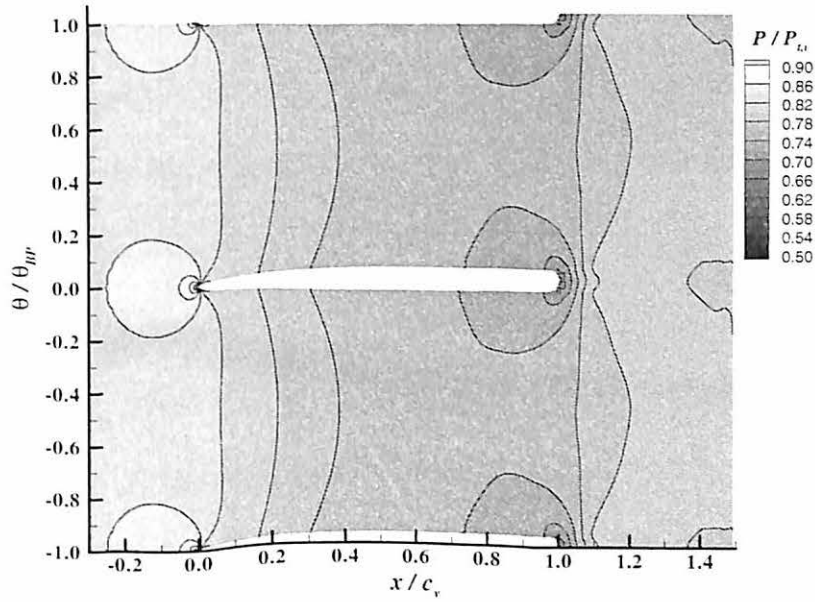
Figure 4-3 Time-Averaged IGV Static Pressure Contours: Blunt-Far, 75% Span.
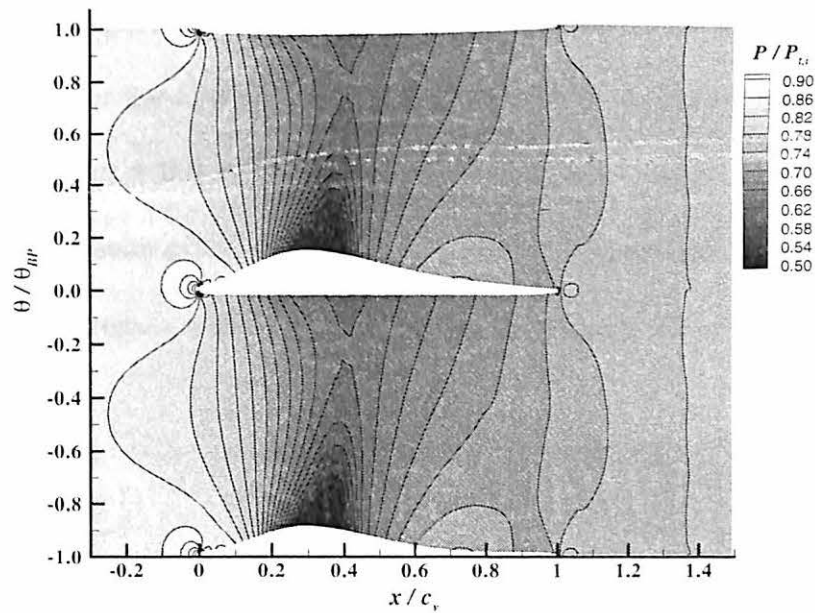
Figure 4-4 Time-Averaged IGV Static Pressure Contours: Sharp-Far, 75% Span.

Figure 4-5 shows time-averaged blunt-IGV static pressure at three different spanwise locations for the far-spacing condition. Clearly, static pressure increases with increasing span between $x/c_v = 0.0 - 0.6$, indicating a time-averaged radial pressure gradient through the blunt-IGV row. The only spanwise effects for the blunt-far IGV occur upstream of the trailing edge.

34
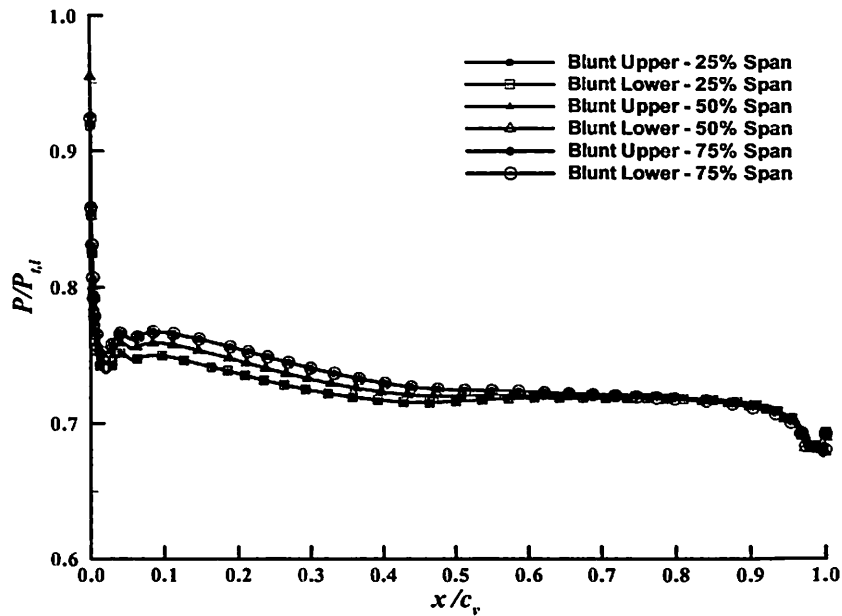
Figure 4-5 Time-Averaged Spanwise IGV Static Pressure: Blunt-Far.

In contrast, Figure 4-6 shows time-averaged blunt-IGV static pressure at different

spanwise locations for the close-spacing condition. Static pressure increases with span at

locations between $x/c_v = 0.0 - 0.6$, similar to the blunt-far condition; however, near the

trailing edge the opposite effect is observed. Higher time-averaged static pressure occurs

near the hub and decreases with span between approximately $x/c_v = 0.7 - 1.0$.

Figure 4-6 Time-Averaged Spanwise IGV Static Pressure: Blunt-Close.

35

This change in trailing-edge pressure behavior at the close-spacing condition may be attributed to unsteady blade-row aerodynamic interactions. For example, at close spacing IGV aerodynamic forcing by the downstream rotor bow shock is amplified, causing a non-linear fluid-structure interaction influencing the time-averaged flow. This interaction is expected to be span dependent, as near the hub rotor bow-shock strength is significantly reduced relative to the blade-tip shock. Thus, the 25% span results at close spacing are similar to all span results for the blunt-IGV at the far-spacing condition, but the 50% and 75% span results differ due to stronger rotor bow-shock interactions. Such interactions also contribute to the discussed blunt-IGV trailing-edge static pressure differences at 75% span noted between Figure 4-1 and Figure 4-2.

Figure 4-7 displays time-averaged IGV static pressure distributions at different spanwise locations for the sharp-far case. Once again, note the vane loading, where the upper-surface pressures do not match those along the lower surface. Similar to the blunt-far case, the upper surface generally experiences higher static pressure with increasing span, except between $x/c_v = 0.3 - 0.45$. The lower surface also experiences static pressure amplification with increasing span, but this effect remains limited to the $x/c_v = 0.0 - 0.4$ chord locations. Notably, the sharp-close case exhibits very similar behavior to the sharp-far data of Figure 4-7, and is thus not depicted here. The sharp-close case does not indicate a change in trailing-edge static pressure like the blunt-close case, suggesting that non-linear fluid-structure interactions caused by rotor bow-shock impingement on the IGV in the blunt-close case are dependent on IGV geometry.
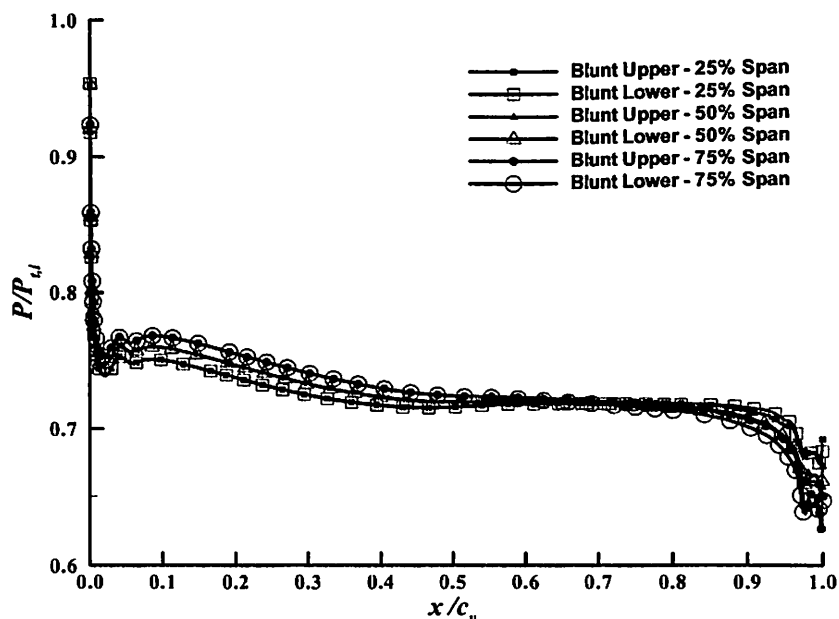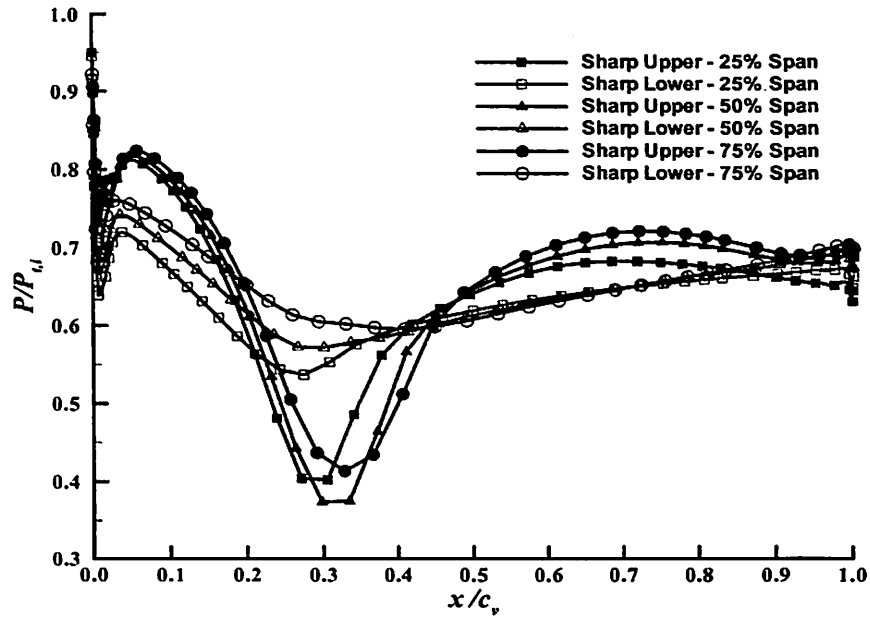
Figure 4-7 Time-Averaged Spanwise IGV Static Pressure: Sharp-Far.

4.3 ROTOR TIME-AVERAGED STATIC-PRESSURE DISTRIBUTIONS

Figure 4-8 displays time-averaged static pressure computed along the rotor chord for the far-spacing condition at 75% span. A mid-passage rotor shock is observed, as characterized by the dramatic increase in pressure along both the rotor upper and lower surfaces; rotor upper and lower surfaces denote the blade suction and pressure surfaces, respectively. Rotor shock first develops on the lower surface around $x/c_r = 0.3$ and then on the upper surface around $x/c_r = 0.7$. The rotor passage-shock orientation is further illustrated by the large static-pressure gradient near mid-passage in Figure 4-9.

In general, IGV trailing-edge geometry has little effect on rotor-shock location, as seen in Figure 4-8. However, around the leading-edge region of the rotor, differential pressure increases for the blunt-IGV case. The same leading-edge differential-pressure amplification occurs for the blunt IGV at close-spacing condition, shown in Figure 4-10. The difference in leading-edge differential-pressure amplification for the blunt-IGV case is less for the close-spacing condition as compared to the far-spacing condition. Beyond

the leading edge, the upper and lower surfaces, for both sharp and blunt IGV cases, show similar static pressure distributions at both close-spacing and far-spacing conditions.
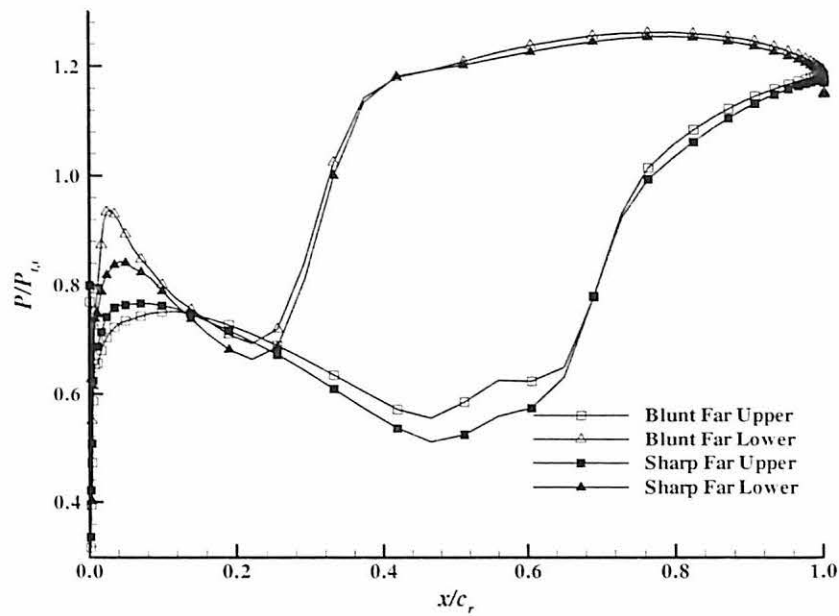
Figure 4-8 Time-Averaged Rotor Static Pressure: Far-Spacing, 75% Span.
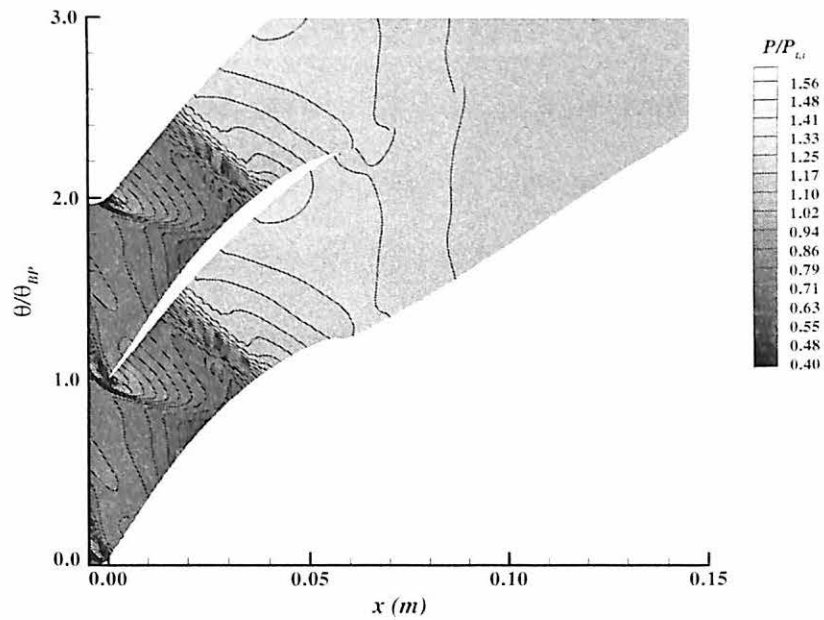
Figure 4-9 Time-Averaged Rotor Static Pressure Contours: Blunt-Far, 75% Span.

38

Figure 4-10 Time-Averaged Rotor Static Pressure: Close-Spacing, 75% Span.

Figure 4-11 shows time-averaged rotor static pressure at three different spanwise locations for the blunt-IGV, far-spacing condition. The rotor mid-passage shock is less pronounced at 25% span, occurring further upstream in the rotor passage. At 75% span, the shock is most pronounced, as expected due to rotor relative velocity amplification with span. Notably, the upper-surface static pressure at 25% span experiences a local minimum around $x/c_r = 0.03$, this phenomenon is not observed at the other spanwise locations. Figure 4-12 shows rotor static pressure at different spanwise locations for the blunt-IGV, close-spacing condition. The observed leading-edge local minimum on the blunt-IGV upper surface is not as pronounced as at the close-spacing condition (compared with Figure 4-11).

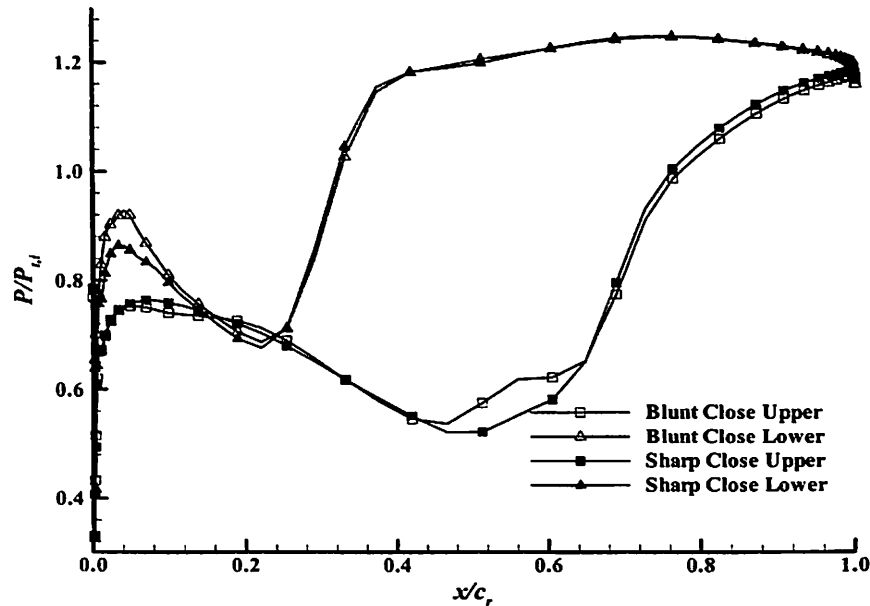**Figure 4-11 Time-Averaged Spanwise Rotor Static Pressure: Blunt-Far.**
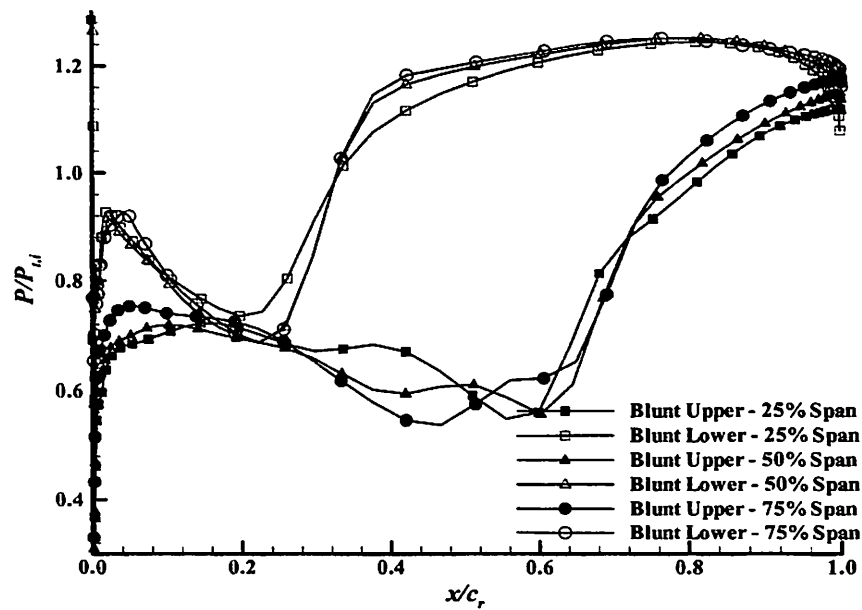
Figure 4-12 Time-Averaged Spanwise Rotor Static Pressure: Blunt-Close.

40

Figure 4-13 shows time-averaged rotor static pressure at three different spanwise locations for the sharp-IGV, far-spacing condition. The static pressure differential across the blade is observed to increase significantly at the leading edge for the 25% spanwise location. This change in behavior relative to the blunt-IGV case can be attributed to flow separation observed on the sharp IGV at 25% span, as discussed below. Similar results are shown for the close-spacing condition in Figure 4-14; although, less leading-edge differential-pressure increase is observed at the 25% spanwise location then at the far-spacing condition. As compared to the blunt-IGV case, rotor static pressure distributions for the sharp IGV are quite similar, except near the leading edge and at 25% span. Near the leading edge, the blunt-IGV case shows an increased rotor pressure differential, while the rotor passage-shack position moves upstream for the sharp-IGV case at 25% span, due to flow separation on the upstream IGV.
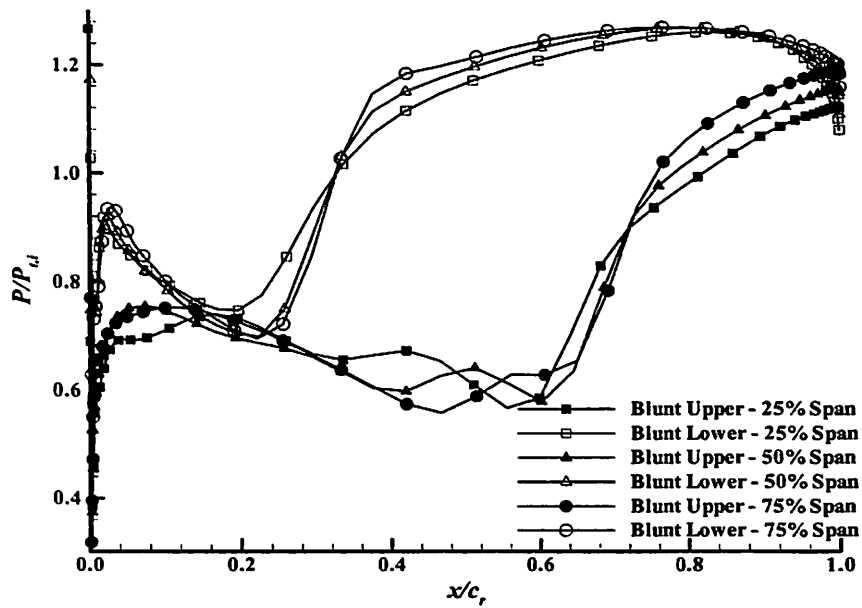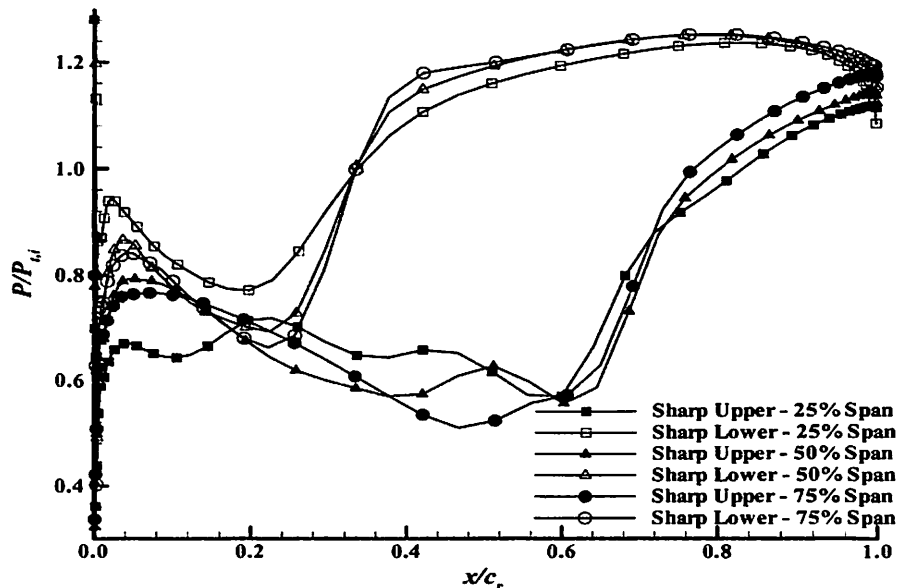

Figure 4-13 Time-Averaged Spanwise Rotor Static Pressure: Sharp-Far.

41
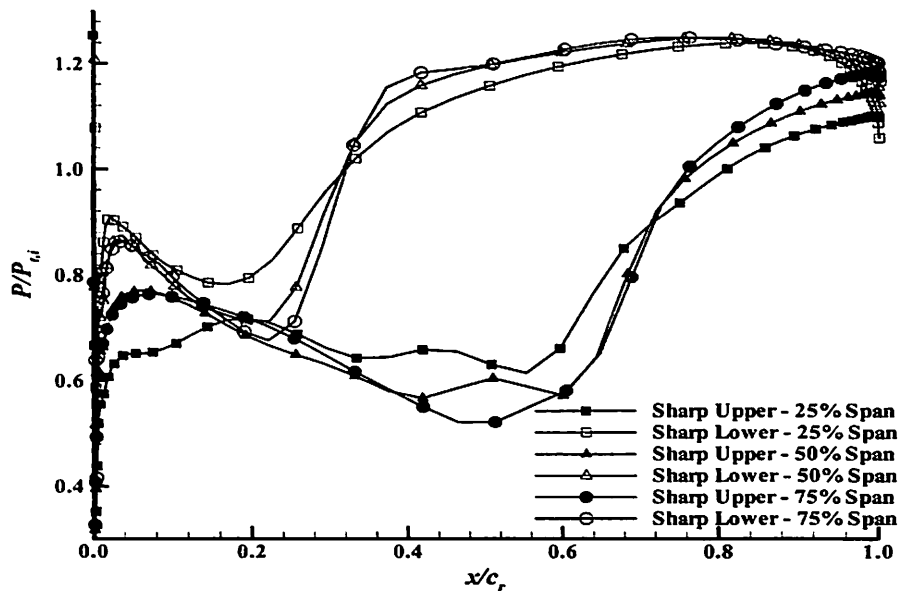
Figure 4-14 Time-Averaged Spanwise Rotor Static Pressure: Sharp-Close.

4.4   IGV TIME-AVERAGED WAKE CHARACTERISTICS

Time-averaged IGV wake character is important when considering forward forcing of the rotor, as IGV wakes directly impact the downstream rotor. IGV wake impact on the rotor influences the rotor potential field. Thus, different downstream-propagating IGV wakes, as might be caused by IGV geometry changes, may contribute to varying upstream-propagating rotor-induced IGV forcing functions. Since IGV forcing is the focus of this thesis, it is important to characterize IGV wake properties.

When examining an IGV wake, total pressure is reported at specific axial and spanwise locations over a single vane pitch (i.e., vane-to-vane passage distance). The axial location examined here equals the sliding-mesh interface location between IGV and rotor computational domains, around 4.0% rotor chords upstream of the rotor leading edge. IGV pitch location is reported such that $\theta/\theta_{BP} = 0.0$ equals the IGV trailing-edge

location. Wake depth is defined as the maximum total pressure deficit, while wake width represents the maximum pitchwise effect of the total pressure deficit.
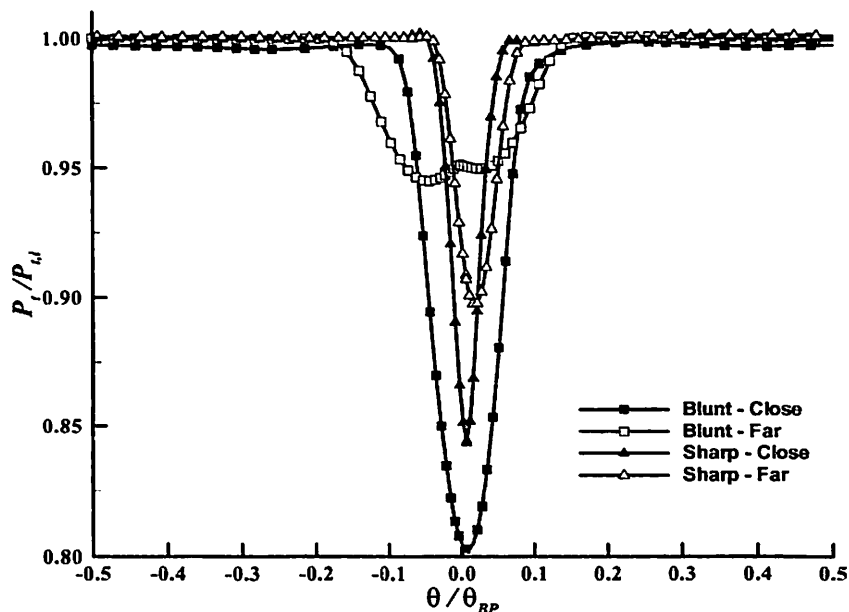
Figure 4-15 Time-Averaged IGV Wake Profiles: 75% Span.

Pitchwise total pressure is plotted in Figure 4-15 at 75% span over a single vane pitch. Wider wake width is observed for both blunt-far and blunt-close cases, as compared to the sharp-IGV geometry. Moreover, wake width widens and wake depth lessens for both blunt-far and sharp-far cases when compared to the corresponding close-spacing cases, as expected due to additional wake mixing length provided at the far-spacing condition. The larger wake depth for the blunt-close case as compared to the sharp-close case, and the smaller wake depth for the blunt-far case as compared to sharp-far case, indicates accelerated wake mixing, or decay, rates for the blunt-IGV geometry. Notably, the blunt-far case yields a "double wake" characteristic, showing two total pressure minima.
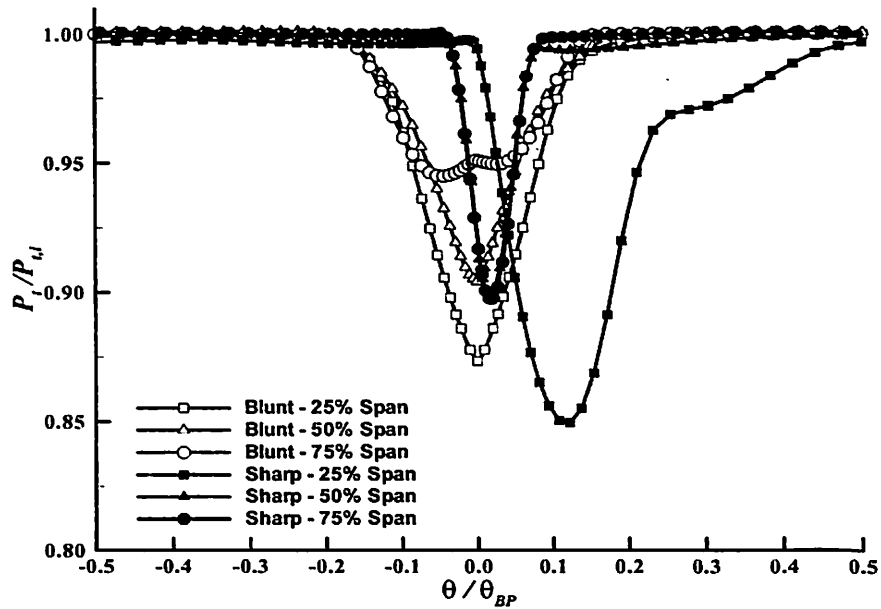
Figure 4-16 Time-Averaged IGV Wake Profiles: Far-Spacing.
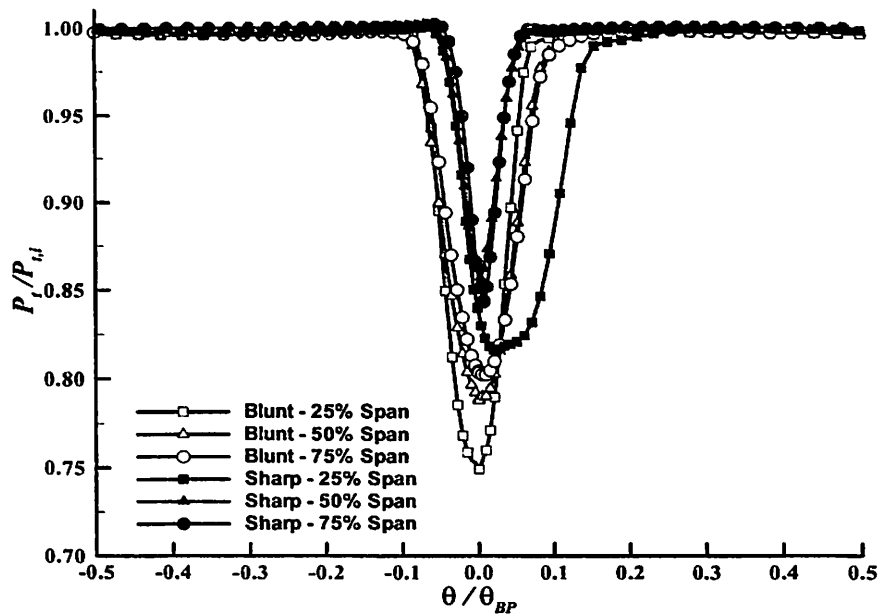
Figure 4-17 Time-Averaged IGV Wake Profiles: Close-Spacing.

Spanwise variations in IGV-wake character are illustrated in Figure 4-16 and Figure 4-17 for the far-spacing and close-spacing conditions, respectively. For both axial spacings, the blunt-IGV wake depth decreases with increased span and wake pitchwise location remains fixed behind the vane (i.e., symmetric about the θ/θ_{BP} = 0.0 location). The blunt-IGV wake-depth behavior with span (see Figure 4-16) may correspond to the

44

slight forward sweep of the IGV trailing edge, providing increased wake-mixing distance near the casing. In contrast, the sharp-IGV geometry shows little variation in wake depth at 50% and 75% span for either spacing condition. At 25% span, however, the sharp IGV shows evidence of significant flow separation along the vane, especially at the far-spacing condition. Flow separation of this nature introduces large secondary-flow perturbations into the downstream rotor, as seen in the total-pressure contour plot illustrating the sharp-IGV separated flow at 25% span in Figure 4-18. Increased unsteady blade-row interactions at close axial spacing may serve to excite the sharp-IGV boundary layer, delaying chordwise separation at 25% span, causing the IGV wake at close spacing to exhibit significantly less width than that at the far-spacing condition. This phenomenon has been previously observed in rotor-stator aerodynamic interaction studies involving forward forcing, as detailed by (Walker et al., 1999 and Solomon et al. 1999) for comparison purposes. Non-separated flow on the blunt-far IGV at 75% span is illustrated in Figure 4-13 for comparison purposes; note the double wake characteristic previous discussed in reference to Figure 4-16.
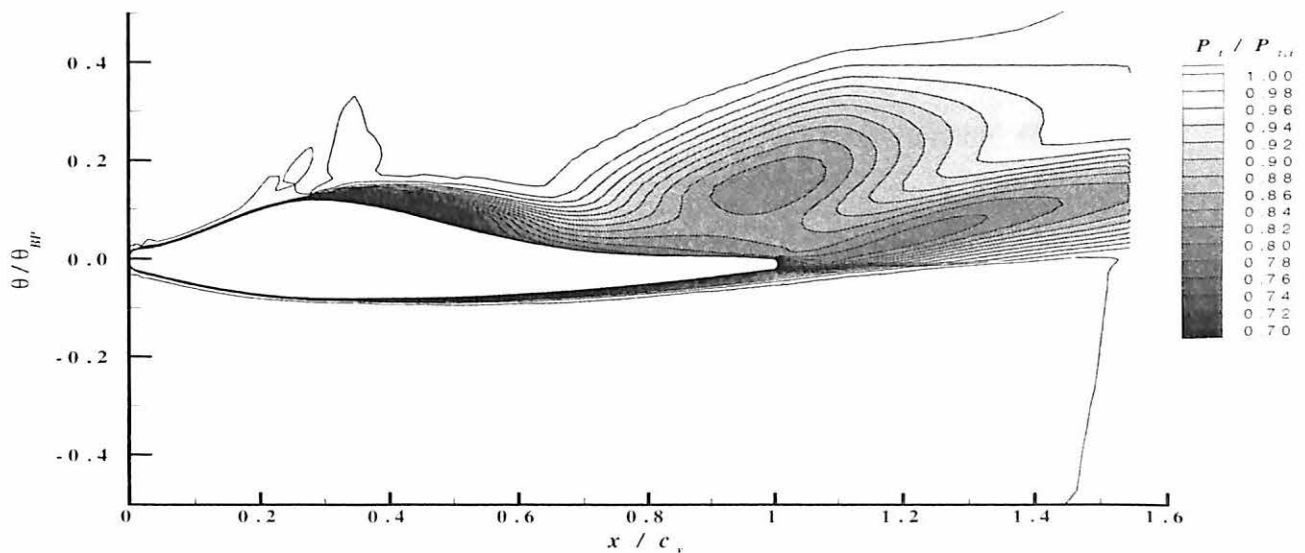
Figure 4-18 Time-Averaged IGV Static Pressure Contours: Sharp-Far, 25% Span.

45
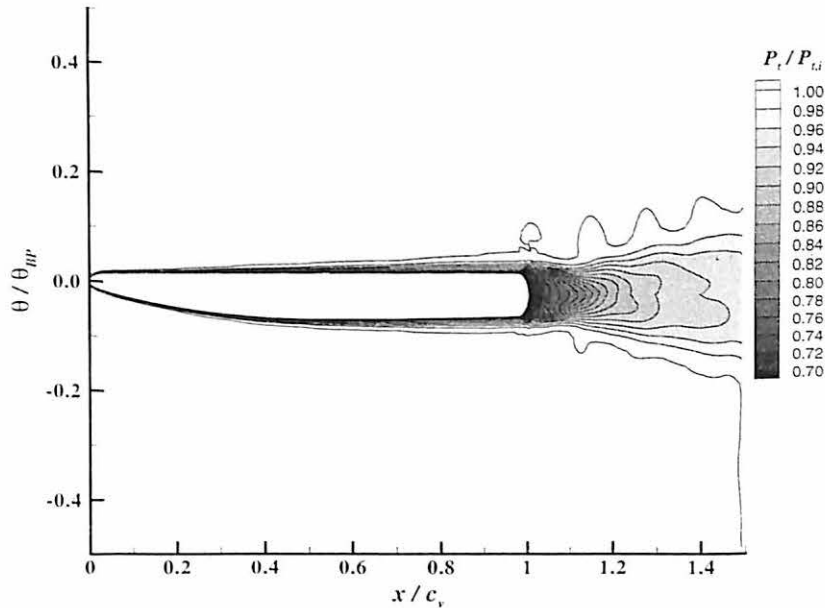
Figure 4-19 Time-Averaged IGV Static Pressure Contours: Blunt-Far, 75% Span.

4.5   ROTOR TIME-AVERAGED INCIDENCE ANGLE

Time-averaged axial velocity at the sliding-mesh interface was computed across one vane pitch at three different spanwise locations. Inlet relative velocity magnitude and angle to the rotor was determined from rotor rotational speed and the averaged axial velocity. Rotor-blade flow incidence angle was calculated by subtracting rotor stagger angle from the computed inlet relative velocity angle.

Rotor-blade flow incidence angle for the different trailing-edge geometries and axial-spacing conditions are reported in Table 4-1. The incidence angle is observed to decrease with increasing spanwise location for all trailing-edge geometries. Correspondingly, wake deficit for the blunt IGV at close spacing (Figure 4-16) was previously noted to decrease with increasing span while wake width remained constant, suggesting reduced wake depth results in lower rotor incidence angles. Table 4-1 also shows that at each spanwise location the blunt IGV at the far-spacing condition produces the largest rotor incidence angle, possibly indicating increased rotor aerodynamic

46

loading. The blunt IGV at the close-spacing condition yields the second highest rotor incidence angle, with the exception of the far-spacing sharp-IGV at 25% span, which is subjected to separated flow perturbations.

The sharp-IGV geometry yields similar incidence angles at both far-spacing and close-spacing conditions at 50% and 75% span. Correspondingly, sharp-IGV wake characteristics are observed to be nearly identical at 50% and 75% span, as shown in Figure 4-16 and Figure 4-17. This suggests similar wake characteristics result in nearly equal rotor incidence angles. At 25% span, however, where IGV flow separation is present, rotor incidence angles differ between the sharp-IGV far-spacing and close spacing conditions. Again, this difference suggests IGV wake characteristics greatly influence rotor incidence angles.

Table 4-1 Relative-Frame Rotor Incidence Angle and Inlet Velocity Magnitude.

Case	Incidence Angle (radians)	Inlet Relative-Velocity Magnitude (m/s)
25% Spanwise Location		
Blunt-IGV, Far-spacing	0.263	340.56
Blunt-IGV, Close-spacing	0.245	345.00
Sharp-IGV, Far-spacing	0.247	344.39
Sharp-IGV, Close-spacing	0.238	346.68
50% Spanwise Location		
Blunt-IGV, Far-spacing	0.227	361.06
Blunt-IGV, Close-spacing	0.214	364.31
Sharp-IGV, Far-spacing	0.209	365.54
Sharp-IGV, Close-spacing	0.208	365.87
75% Spanwise Location		
Blunt-IGV, Far-spacing	0.194	380.51
Blunt-IGV, Close-spacing	0.183	383.27
Sharp-IGV, Far-spacing	0.177	384.89
Sharp-IGV, Close-spacing	0.177	384.78

4.6   ROTOR-INDUCED PRESSURE DISTURBANCE

Figure 4-20 illustrates instantaneous static pressure contours for the blunt-IGV far-spacing condition at 75% span. Similar contours are shown at 50% and 25% span in Figure 4-21 and Figure 4-22, respectively. Focusing on the rotor-induced pressure disturbance (i.e., bow shock) illustrated by the sharp pressure gradient created by, and emanating upstream from, the rotor leading edge, a comparison of IGV-forcing function variation with spanwise location is made. The rotor-induced pressure disturbance is observed to increase in strength with increasing span, as would be expected due to the increased rotor relative velocity (see Table 4-1). In addition, disturbance angle relative to the axial direction (x-axis) is observed to increase with increasing spanwise location. Comparing these rotor-induced pressure disturbance characteristics with the rotor incidence angle and inlet relative-velocity magnitude results, it can be concluded that increased incidence angles result in decreased relative disturbance angles, and decreased inlet relative-velocity magnitudes result in decreased disturbance strengths.

Instantaneous pressure contours are shown for the blunt-IGV, close-spacing condition at 75%, 50%, and 25% span in Figure 4-23, Figure 4-24, and Figure 4-25, respectively. Again, rotor-induced disturbance strength and relative disturbance angle-increase with increasing span. This observation correlates with decreased rotor incidence angles with increasing span, as well as less rotor leading-edge differential pressure with increasing span (as shown for both far-spacing and close spacing conditions in Figure 4-11 and Figure 4-12, respectively).

Figure 4-20 IGV Static-Pressure Contours:
Blunt-Far, 75% Span, $t = 0$.
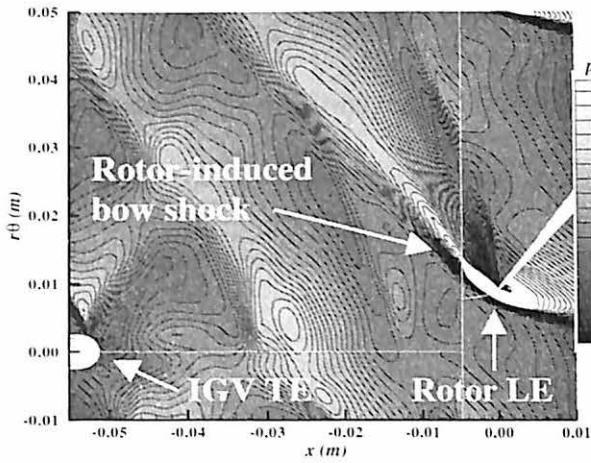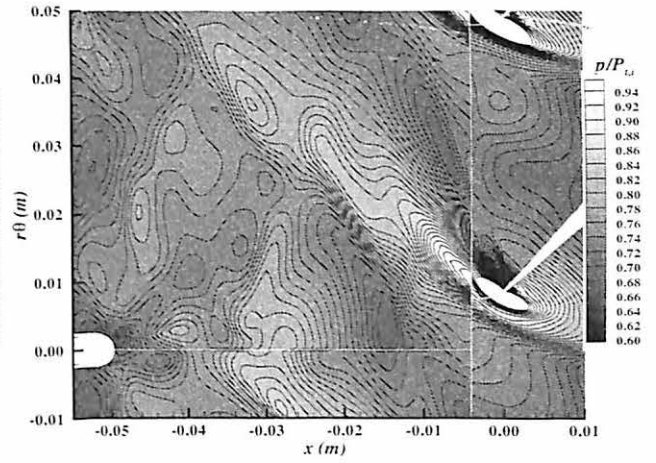

Figure 4-21   IGV Static-Pressure Contours:
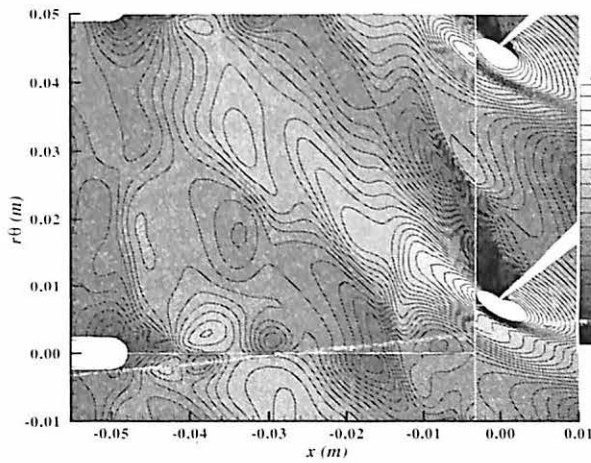Blunt-Far, 50% Span, $t = 0$.

Figure 4-22   IGV Static-Pressure Contours:
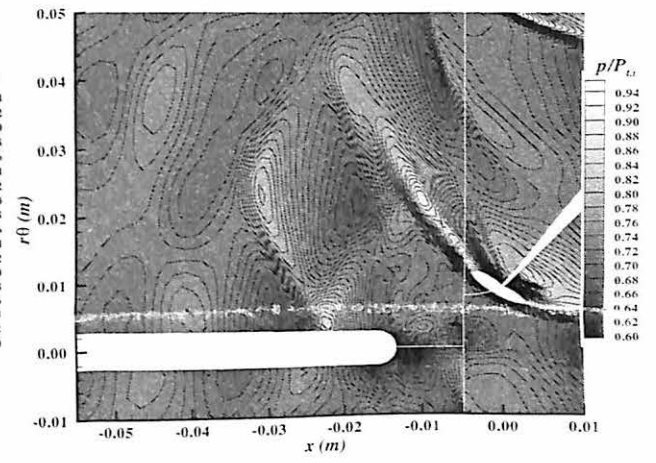Blunt-Far, 25% Span, $t = 0$.

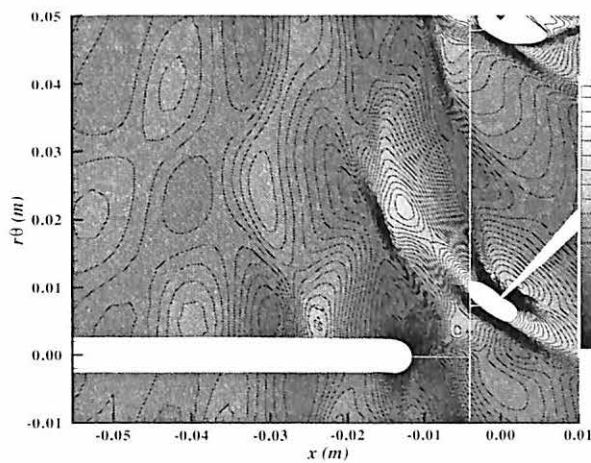Figure 4-23   IGV Static-Pressure Contours:
Blunt-Close, 75% Span, $t = 0$.

Figure 4-24   IGV Static-Pressure Contours:
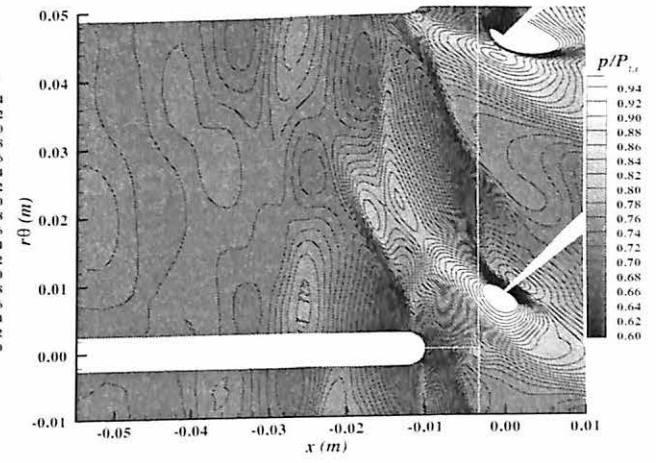Blunt-Close, 50% Span, $t = 0$.

Figure 4-25   IGV Static-Pressure Contours:
Blunt-Close, 25% Span, $t = 0$.

49

Comparing rotor-induced disturbances between the blunt-IGV far-spacing and close-spacing conditions, disturbance strength is observed to be less at the far-spacing condition. Magnified blunt-close disturbance strength at 75% span coincides with a smaller leading-edge differential pressure (shown in Figure 4-10) as compared to far spacing (Figure 4-8). This observation is also supported by rotor-inlet velocity magnitude, where smaller differential-pressure magnitude, and thus less loading, exists for the blunt-IGV at the close-spacing condition as compared to the far-spacing condition.

Sharp-IGV pressure contours for the far-spacing condition at 75%, 50%, and 25% span are shown in Figure 4-26, Figure 4-27, and Figure 4-28, respectively. Again, the rotor-induced pressure disturbances increase in strength and relative angle with increasing span. Similar pressure contours are illustrated in Figure 4-29 through Figure 4-31 for the sharp-IGV at the close-spacing condition. Axial-spacing effects on rotor-induced pressure disturbances are observed to have little difference at 50% and 75% span. However, significant difference is observed between the sharp-far and sharp-close conditions at 25% span. Although almost no difference is observed when directly comparing the rotor-induced pressure disturbance strength and relative angle between the sharp-IGV and blunt-IGV, the sharp-IGV case generally exhibits a slightly increased rotor-induced disturbance magnitude and relative disturbance angle, except at 50% span where the sharp-IGV exhibits significantly greater rotor-induced disturbance magnitude. Spanwise amplification of the rotor-induced disturbance is illustrated in Figure 4-32, showing the 50% span data to have the largest maximum and peak-to-peak pressure amplitudes at $x/c_v = 0.2$ upstream of the sliding-mesh interface and $\theta/\theta_{BP} = 0.0$.

Figure 4-26 IGV Static-Pressure Contours: Sharp-Far, 75% Span, t = 0.

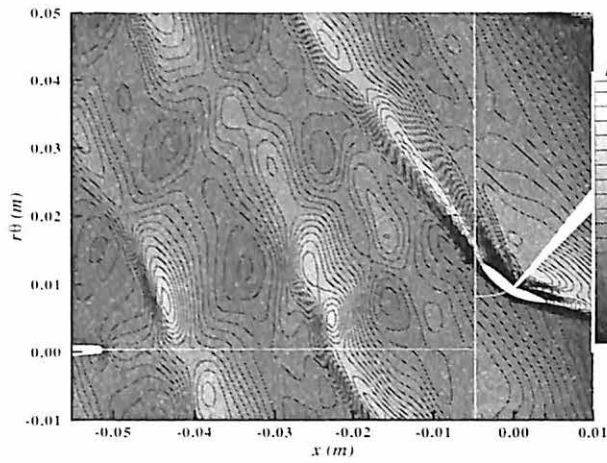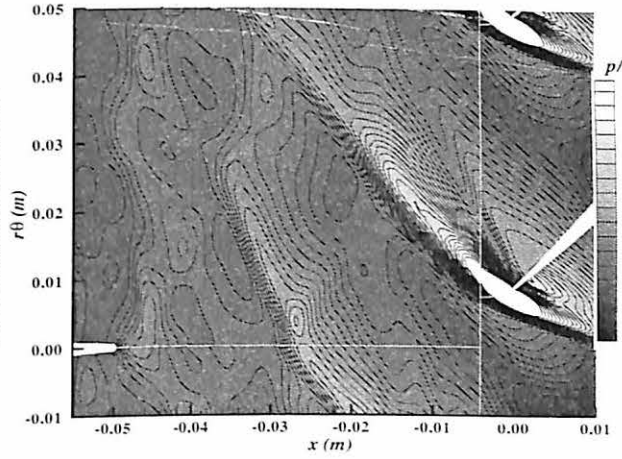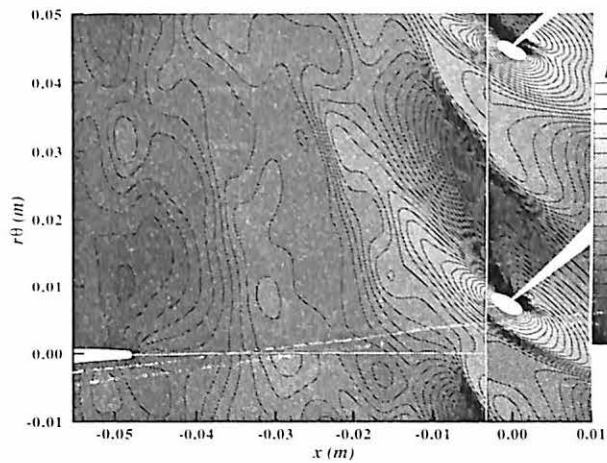**Figure 4-27 IGV Static-Pressure Contours: Sharp-Far, 50% Span, t = 0.**

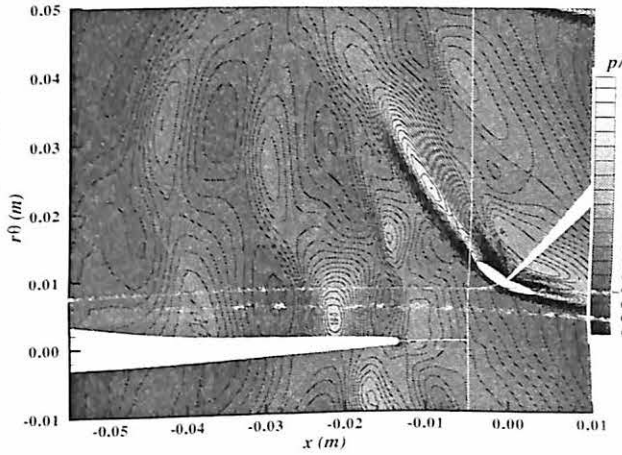**Figure 4-28 IGV Static-Pressure Contours: Sharp-Far, 25% Span, t = 0.**

Figure 4-29 IGV Static-Pressure Contours: Sharp-Close, 75% Span, t = 0.
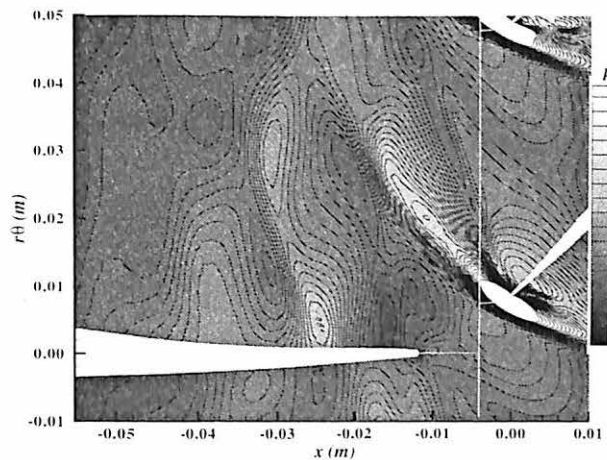
Figure 4-30 IGV Static-Pressure Contours: Sharp-Close, 50% Span, t = 0.
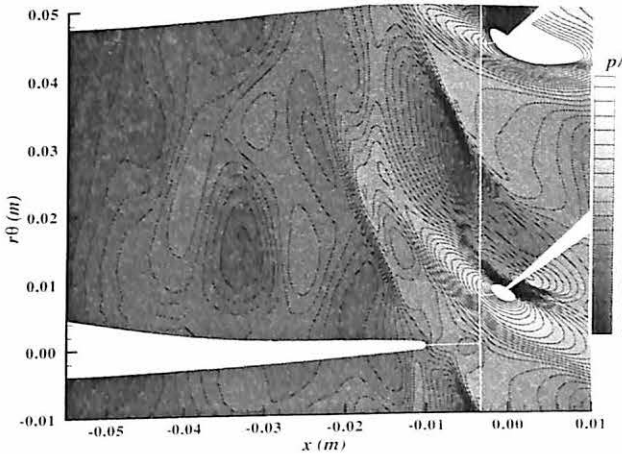
Figure 4-31 IGV Static-Pressure Contours: Sharp-Close, 25% Span, t = 0.

51
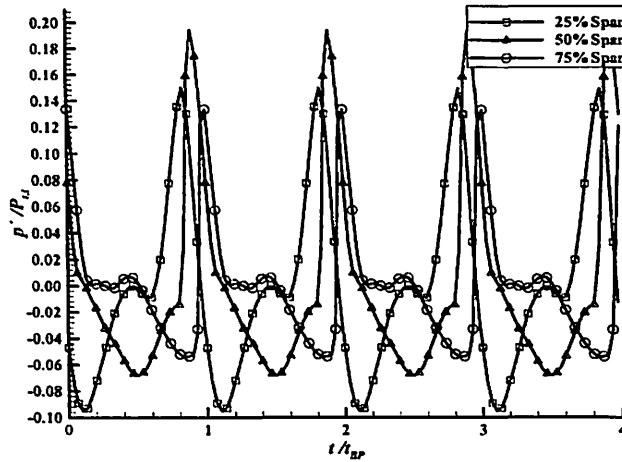
Figure 4-32 Rotor-Induced Forcing Function: $x/c_v = 0.20$
Upstream of Sliding Interface, $\theta/\theta_{BP} = 0.0$, **Sharp-Close.**

4.7 TIME-AVERAGED RESULT SUMMARY

MSU-TURBO produced well-behaved time-averaged static pressure distributions indicating the sharp IGV to be aerodynamically loaded and the blunt IGV to be unloaded, as expected. When comparing the blunt-IGV case at 75% span between the close-spacing and far-spacing conditions, a decrease in static pressure at the IGV trailing edge was observed with decreased axial spacing. This decrease in static pressure was not observed for the sharp-IGV case, indicating a geometry dependence on rotor bow-shock interaction with the IGV trailing edge. Interestingly, the observed decrease in trailing-edge static pressure on the blunt-IGV was a function of span, suggesting stronger nonlinear fluid-structure interactions caused by rotor bow-shock impingement occurring toward the casing.

Rotor time-averaged static pressure distributions indicated a passage shock to exist. Overall, changes in IGV trailing-edge geometry or IGV-rotor axial spacing had little effect on the passage shock location.

Wakes developed from the different IGV geometries and axial-spacing conditions were compared. The blunt-IGV resulted in larger wakes as compared to the sharp-IGV.

with the exception of 25% span were flow separation was present for the sharp-IGV. Differences in IGV-wake characteristics were determined to influence rotor incidence angle. In turn, a change in incidence angle resulted in different rotor leading-edge loading conditions. Time-averaged static pressure distributions along the rotor chord indicate a greater leading-edge differential pressure for the blunt-IGV cases, corresponding to larger incidence angles at a particular span. In addition, rotor leading-edge differential pressure was observed to be greater for the far-spacing condition compared to the close-spacing condition, again corresponding to large rotor incidence angles.

Differences in rotor leading-edge loading correspond to different rotor-emitted potential disturbances (i.e., bow shocks). Thus, rotor-induced potential disturbances are a function of both IGV trailing-edge geometry and IGV-rotor axial spacing. Disturbance strength is observed to be stronger near the casing for both sharp-IGV and blunt-IGV cases, resulting from greater rotor-inlet velocity magnitudes toward the casing. Relative disturbance angle was also observed to increase with increasing span, resulting from decreasing rotor incidence angle with span. Axial-spacing effects on rotor-induced pressure disturbances were observed at all spanwise location for the blunt-IGV case. In contrast, the sharp-IGV case indicated little difference between the rotor-emitted pressure disturbances at far-spacing and close-spacing conditions, except at 25% span where flow separation was observed. Although little difference was observed between the blunt IGV and sharp IGV at 25% and 75% span, the sharp IGV exhibited significantly greater rotor-induced disturbance strength at 50% span.

5 IGV UNSTEADY FORCING

This chapter describes unsteady forcing on the upstream IGV, where unsteady forcing is reported in terms of chordwise IGV unsteady surface-pressure distribution, spectral content, and phase. The effects of IGV-rotor axial spacing and trailing-edge geometry are considered at 75% span. Presented unsteady flow results were developed from instantaneous static pressure data with the time-averaged static pressure removed.

5.1   IGV SURFACE-PRESSURE TIME DEPENDENCY

Figure 5-1 through Figure 5-6 show contours of static pressure for the blunt-IGV at the far axial-spacing condition. The plots represent instantaneous points in time, separated by exactly one-sixth of a blade-passing period. It is observed that rotor-induced pressure disturbances rotate with the rotor-blade (not shown) as it rotates in time. The pressure waves are also periodic and repeat with every blade passing. As the static pressure disturbances rotate with the rotor, they directly impact the upstream IGV trailing edge. At the IGV trailing edge, the pressure disturbances split and travel upstream along both IGV lower and upper surfaces. This disturbance splitting process is most evident from $t = 2T/3$ to $t = 5T/6$. At impact on the IGV upper surface, the pressure waves reflect (see Figure 5-1) back into the oncoming disturbance field. The impacted wave and its reflection travel together upstream along the vane, decaying in strength during the process. On the IGV lower surface, pressure wave impact and reflection is much less prominent, the wave chordwise propagation is delayed (i.e. further downstream) relative to the upper surface.

54

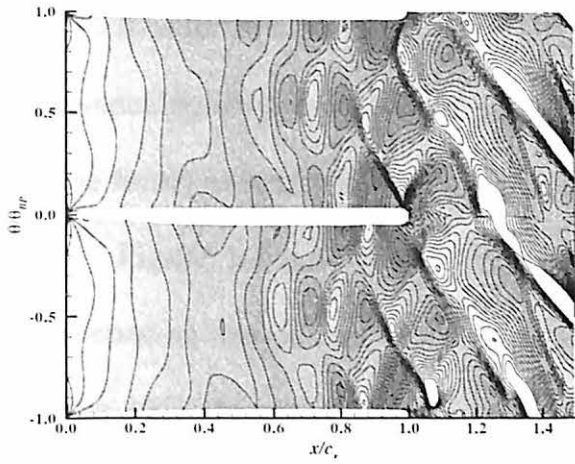Figure 5-1   IGV Static-Pressure Contours:
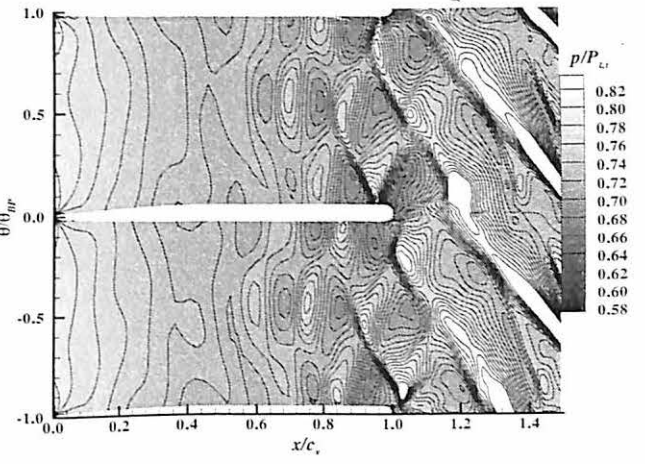Blunt-Far, $t = 0$.

Figure 5-2   IGV Static-Pressure Contours:
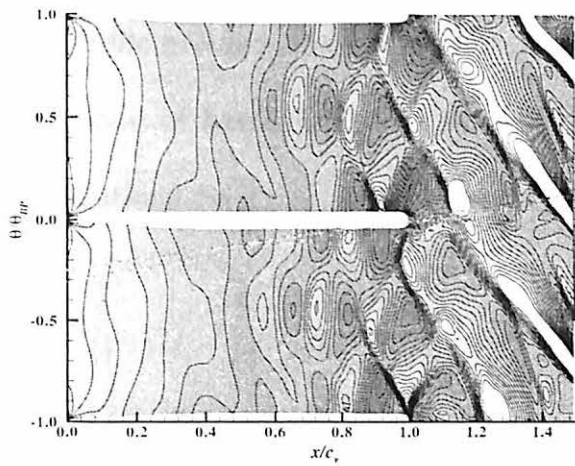Blunt-Far, $t = T/6$.

Figure 5-3   IGV Static-Pressure Contours:
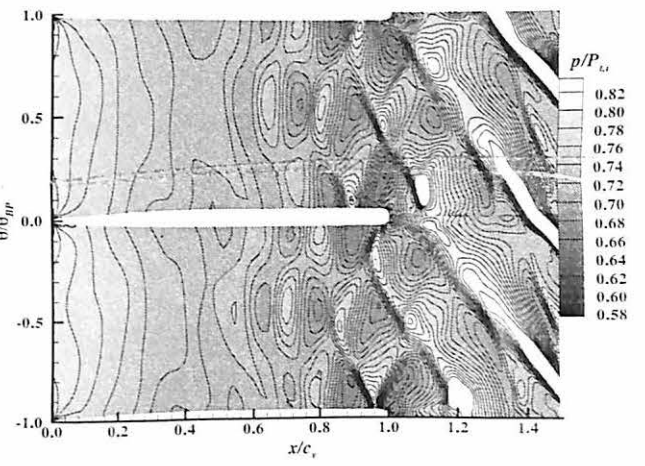Blunt-Far, $t = T/3$.

Figure 5-4   IGV Static-Pressure Contours:
Blunt-Far, $t = T/2$.
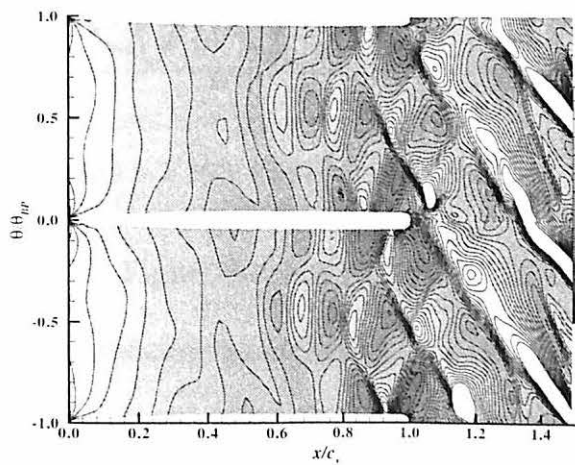
Figure 5-5   IGV Static-Pressure Contours:
Blunt-Far, $t = 2T/3$.
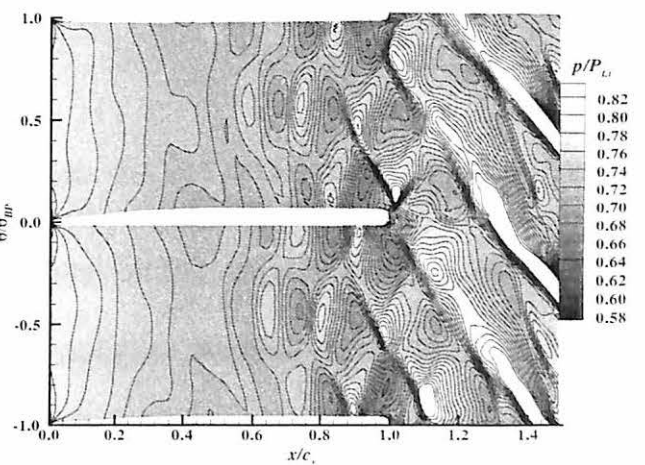
Figure 5-6   IGV Static-Pressure Contours:
Blunt-Far, $t = 5T/6$.

55

Similar instantaneous contour plots of static pressure for the blunt IGV at the close-spacing condition, and the sharp IGV at both close and far axial-spacing conditions, can be found in Appendix C.

Figure 5-7 and Figure 5-8 show blunt-IGV surface-pressure time series for both axial-spacing conditions at four upper-surface chord locations. As expected, these figures indicate periodic static-pressure variations corresponding to the rotor blade-passing frequency. A monotonic phase shift is also observed between vane-chord locations, indicating constant-speed disturbance propagation upstream along the chord. While the pressure fluctuations are periodic, they are not purely sinusoidal, indicating the existence of harmonic content. For both axial-spacing cases, larger unsteady pressure fluctuations exist near the IGV trailing edge, decaying rapidly upstream.
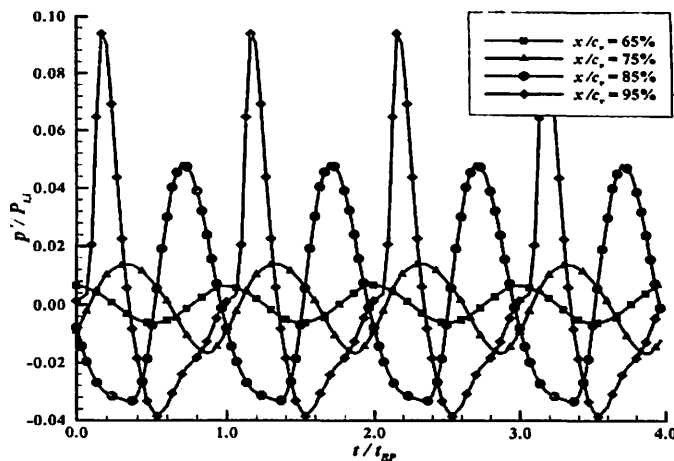
Figure 5-7 IGV Upper-Surface Pressure Time Series: Blunt-Far.
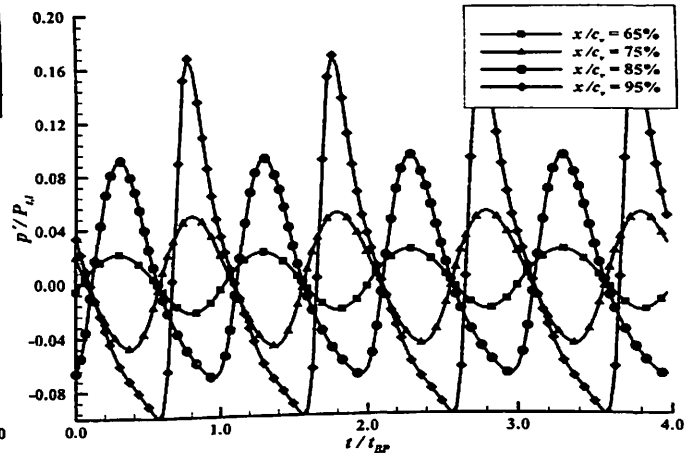
Figure 5-8 IGV Upper-Surface Pressure Time Series: Blunt Close.

Figure 5-9 and Figure 5-10 show sharp-IGV surface-pressure time series for both axial-spacing conditions along the vane upper surface. Similar to the blunt IGV, the sharp geometry shows periodic time-series behavior corresponding to the rotor blade-passing frequency, unsteady trailing-edge pressure amplification, and a monotonic phase

shift between different chordwise locations. However, the overall time-series amplitudes are greater for the blunt trailing-edge geometry as compared to the sharp geometry.
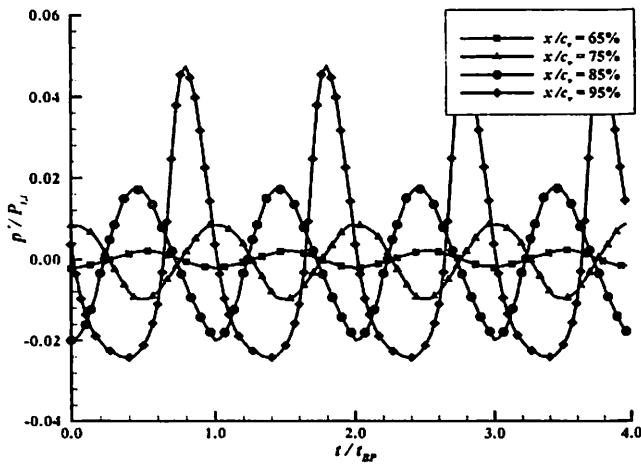
Figure 5-9 IGV Upper-Surface Pressure Time Series: Sharp-Far.
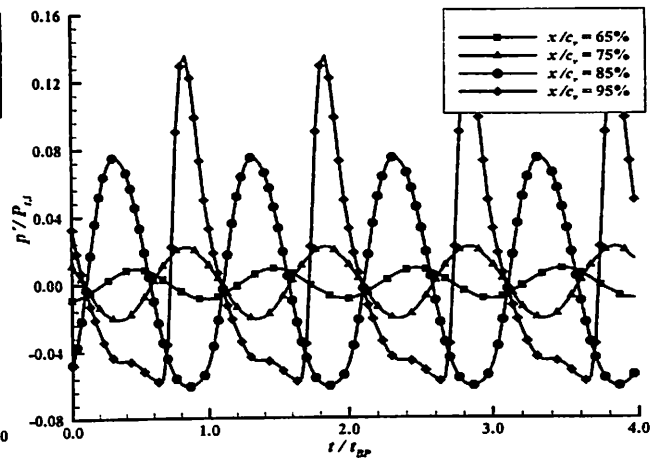
Figure 5-10 IGV Upper-Surface Pressure Time Series: Sharp Close.

When comparing far and close axial-spacing conditions for both IGV geometries, a decrease in spacing results in higher-amplitude unsteady pressure fluctuations. For the sharp trailing-edge geometry, approximately three times greater amplitude is observed at the close-spacing condition, while the blunt trailing-edge geometry exhibits around two times greater pressure amplitudes at the close condition.

5.2 IGV SURFACE-PRESSURE SPECTRAL CONTENT

Figure 5-11 and Figure 5-12 depict spectral content for the blunt-far and blunt-close time series corresponding to Figure 5-7 and Figure 5-8, respectively. Relevant IGV surface-pressure frequencies reaching five times the blade-passing frequency are observed. The blunt trailing-edge geometry exhibits increased higher-order pressure harmonics near the trailing-edge region at both far-spacing and close-spacing conditions, where the close-spacing condition shows greater harmonic amplitude. In both cases, higher-order harmonic content decays rapidly upstream along the vane, with the 65% and 75% IGV chord data displaying almost no pressure amplitude beyond the fundamental

blade-passing frequency (i.e., $f/f_{BP} = 1$). This behavior is expected, as the acute pressure gradient produced by the rotor-induced bow shock inherently produces large harmonic content shock strength which decays rapidly upstream (at exponential rates) through the vane row, diffusing the IGV unsteady surface-pressure into a sinusoidal waveform devoid of harmonic content.

Figure 5-11 IGV Upper-Surface Pressure
Spectral Content: Blunt-Far.

Figure 5-12 IGV Upper-Surface Pressure
Spectral Content: Blunt-Close.
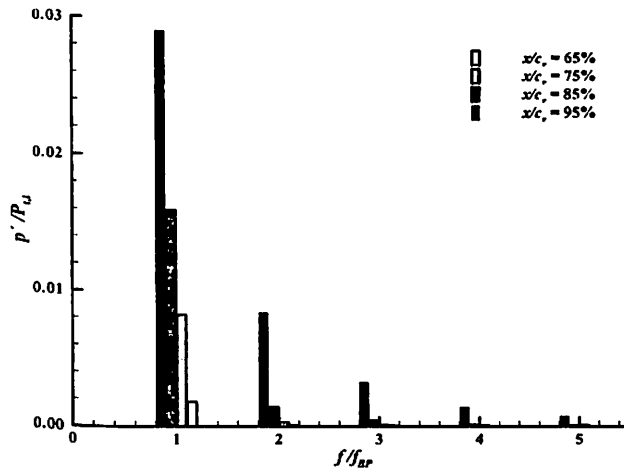
Figure 5-13 IGV Upper-Surface Pressure
Spectral Content: Sharp-Far.
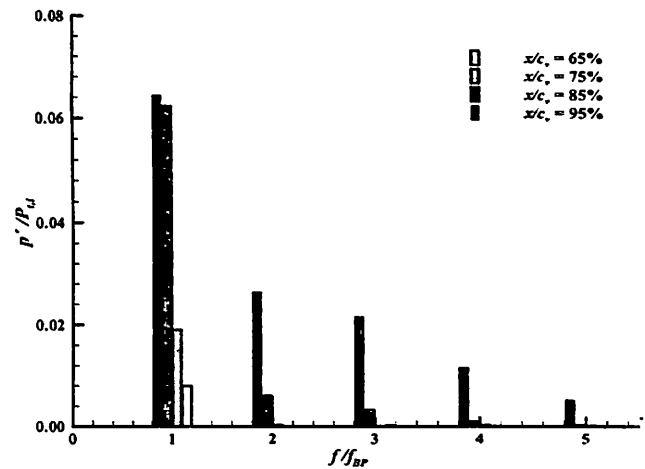
Figure 5-14 IGV Upper-Surface Pressure
Spectral Content: Sharp-Close.

Spectral content for the far-spacing and close-spacing conditions with the sharp trailing-edge IGV are shown in Figure 5-13 and Figure 5-14, corresponding to the time-series data in Figure 5-9 and Figure 5-10, respectively. When compared to the close-
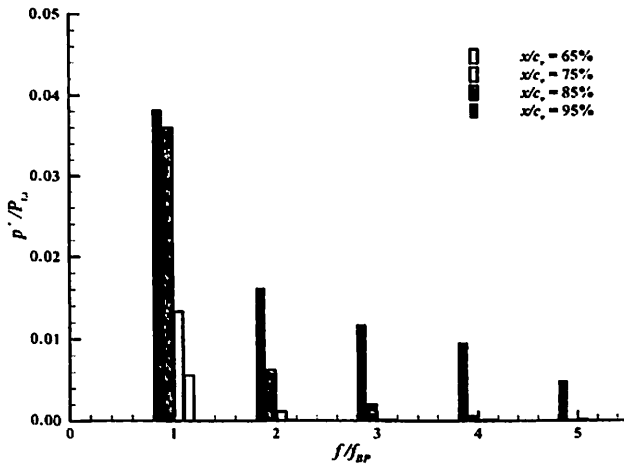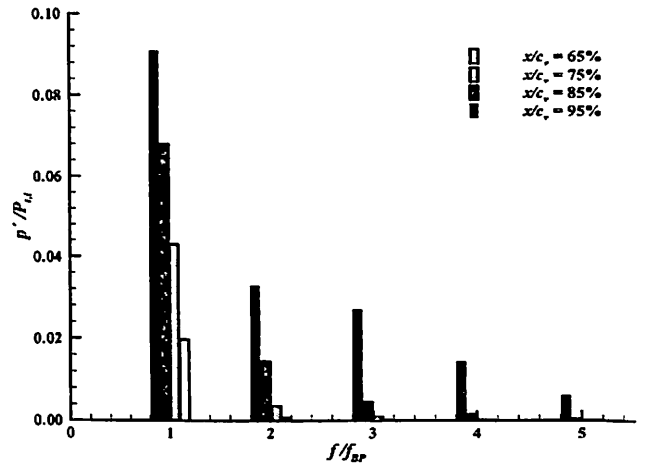
spacing condition, far spacing is observed to have significantly less harmonic content relative to the fundamental frequency. This indicates the rotor-induced disturbance has become almost purely sinusoidal before it interacts with the sharp-IGV trailing edge.

Comparing results for the sharp IGV to those of the blunt IGV show several differences. First, overall pressure amplitude decreases for the sharp-IGV case, at both axial-spacing conditions. Second, at far-spacing conditions, the blunt IGV shows significant spectral content at the trailing edge as compared with sharp-IGV geometry, indicating a dependence on trailing-edge geometry. This increase in harmonic content is supported by time-series data where the blunt-IGV waveform has a "see-saw" shape for $x/c_v = 0.95$ shown in Figure 5-7, but the same waveform has a sinusoidal shape the sharp IGV in Figure 5-9. Finally, the decay of surface-pressure harmonic content upstream along the vane is similar for both geometries.

5.3 IGV SURFACE-PRESSURE FIRST-HARMONIC CHORDWISE AMPLITUDE

Figure 5-15 and Figure 5-16 express the IGV first-harmonic (i.e., the fundamental blade-passing frequency) unsteady pressure dependence on chord for the blunt-far and blunt-close IGV spacing conditions, respectively. Each figure displays IGV upper-surface, lower-surface, and differential unsteady pressures in the vane aft half-chord region. Differential unsteady pressure represents upper-surface minus lower-surface pressure, as presented in Eq. (5-1).

$$\Delta p' = p'_u - p'_l \qquad (5-1)$$

Similar first-harmonic pressure data is depicted for the sharp IGV at both axial spacings in Figure 5-17 and Figure 5-18.

59
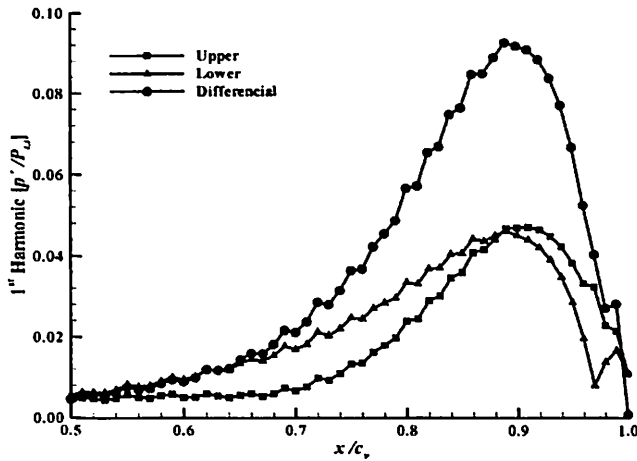
Figure 5-15 1ˢᵗ Harmonic Pressure: Blunt-Far.
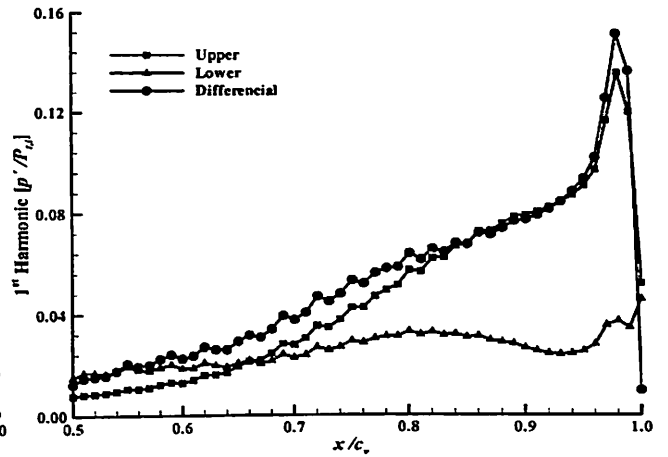
Figure 5-16 1ˢᵗ Harmonic Pressure: Blunt-Close.
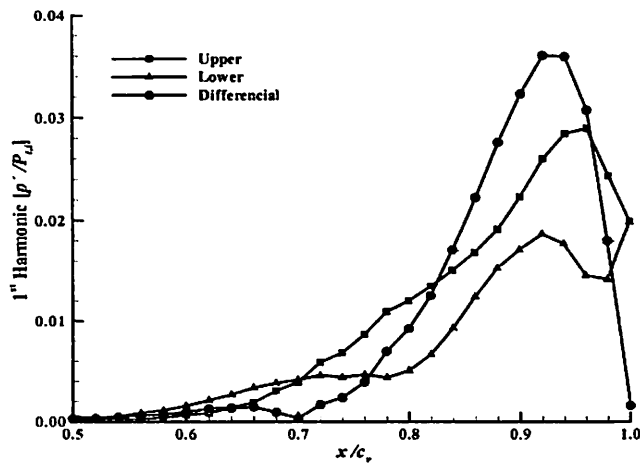
Figure 5-17 1ˢᵗ Harmonic Pressure: Sharp-Far.
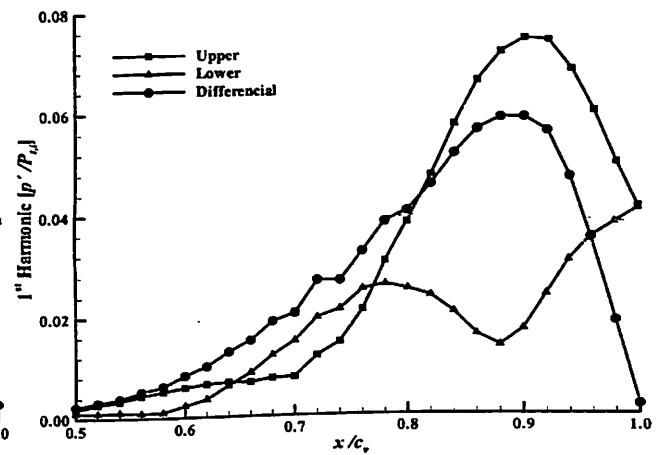
Figure 5-18 1ˢᵗ Harmonic Pressure: Sharp-Close.

By comparing first-harmonic data, several observations can be made. First, at both axial-spacing conditions, the blunt IGV exhibits higher-amplitude unsteady pressures, and therefore more unsteady loading, along the entire vane. This contrasts previous ascertains made in Chapter 4, stating that the blunt-IGV geometry produces weaker rotor-induced bow waves (i.e., IGV forcing functions) as compared to the sharp-IGV. Thus, IGV geometry plays a strong role in vane unsteady forcing amplitude. Second, differential pressure ubiquitously amplifies toward the IGV trailing edge, although the maximum pressure location does not occur at $x/c_v = 1.0$ and varies with IGV geometry and axial spacing. For the blunt IGV, the maximum differential-pressure

60

location moves between approximately 90% - 99% IGV chord with decreased axial spacing, while the sharp-IGV maximum differential-pressure location translates between approximately 93% - 89% IGV chord with a similar spacing reduction. Third, pressure amplification occurs on the IGV lower surface at $x/c_v = 0.78$ and $x/c_v = 0.92$ for close-spacing and far-spacing conditions, respectively, which is not mirrored on the upper surface. This phenomenon was previously identified by Falk and Darbe (2003), relating it to IGV-row solidity and showing increasing vane-row solidity to amplify lower-surface unsteady pressure near mid-chord (Falk et al., 2003). As such, lower-surface pressure amplification near $x/c_v = 0.78 - 0.92$ to aerodynamic disturbance interactions through the IGV passage, as caused by disturbance reflections off adjacent vane surfaces, as addressed later. Finally, IGV differential pressure amplifies between far-spacing and close-spacing conditions, corresponding to increased forcing-function amplitudes at IGV positions closer to the rotor. The maximum amplitude of the IGV differential pressure reaches approximately 10% (~10 kPa) and 16% (~16 kPa) of the time-averaged inlet total pressure, for the blunt-far and blunt-close vanes, respectively. Similarly, the sharp-far and sharp-close cases experience maximum IGV surface differential-pressure amplitudes of 4% (~4 kPa) and 8% (~8kPa), respectively.

Despite exhibiting differential-pressure amplification toward the IGV trailing edge, all simulations also show vane upper-surface and lower-surface pressure amplitudes to equalize directly at the trailing edge, giving zero differential pressure directly at $x/c_v = 1.0$. This finding strengthens previous suppositions made by Falk and Darbe (2003), suggesting no trailing-edge differential-pressure singularity exists for rearward forced vane rows. Note, however, that significant pressure amplification, or

"singularity-like" behavior occurs for the blunt-IGV near $x/c_v = 0.96$ in Figure 5-16. This behavior is akin to the "singularity" commonly observed in steady-state pressure distributions near the leading edge of thin airfoils. Previous arguments made from experimental data regarding the possible existence of a trailing-edge pressure singularity for IGV rearward forcing, such as those of Fabian et al. (1999, 2001), are therefore supported by the blunt-close data. Interestingly, the sharp-IGV demonstrates no tendency toward a differential-pressure spike at the trailing edge; a notable finding given that Fabian et al. worked exclusively with sharp-trailing-edge vanes, and predicted that only sharp-trailing-edge vanes could support a trailing-edge singularity.

5.4 "SINGULARITY LIKE" TRAILING EDGE PRESSURE BEHAVIOR

Figure 5-19 through Figure 5-24 show instantaneous static-pressure contours near the blunt-IGV trailing-edge region at the close-spacing condition. Each plot represents a different instant in time, separated by one-sixth of a blade-passing period. While at times $t = 0$ to $t = T/3$ the rotor-induced disturbances propagate toward the IGV trailing edge, at $t = T/2$ the disturbance directly impacts the trailing edge. At impact, the rotor bow shock induces a large positive pressure on the IGV trailing-edge upper surface. At the same instant in time, an area of lower pressure interacts at the IGV trailing-edge lower surface. This lower pressure area is caused by an expansion wave emanating from behind the rotor-induced bow shock attached to the previous blade (seen best in Figure 5-22). The pressure expansion wave propagates upstream at a slower speed than the bow shock allowing the two disturbances to interact with each other at the IGV trailing edge at the same instant in time. The combination of a high-pressure disturbance on the IGV upper surface and low-pressure expansion wave on the IGV lower surface results in high

unsteady pressure loading of the IGV trailing-edge region (i.e., the "singularity-like" differential pressure observed in Figure 5-16). This phenomenon is only observed at the trailing edge because this is the only chord location where the high pressure and low pressure meet on opposite sides of the IGV. This coincidental phenomenon is not observed for the other examined IGV-forcing cases at 75% span.
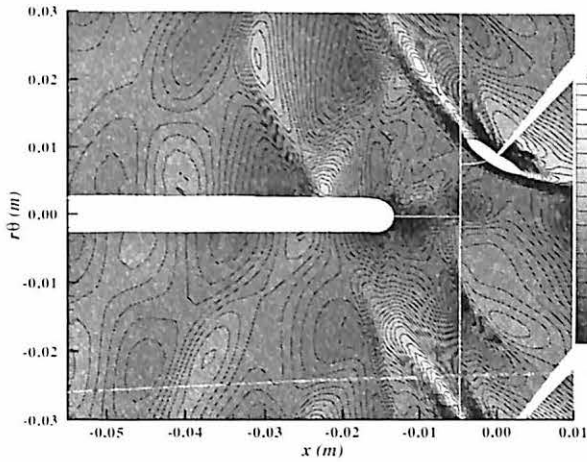
Figure 5-19   IGV Static-Pressure Contours: Blunt-Close, 75% Span, $t = 0$.
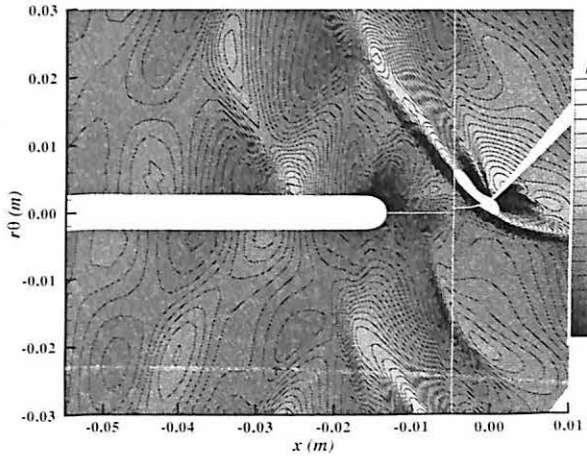
Figure 5-20   IGV Static-Pressure Contours: Blunt-Close, 75% Span, $t = T/6$.
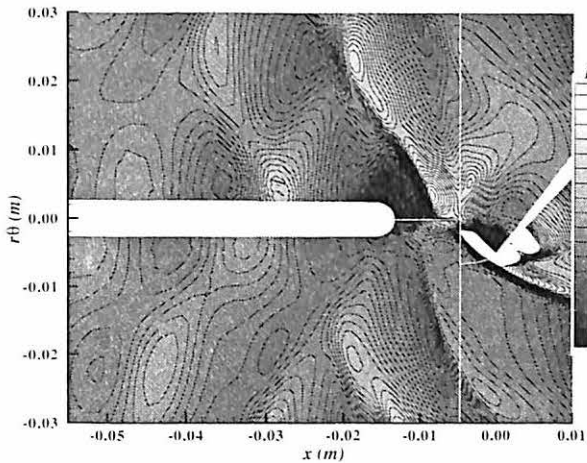
Figure 5-21   IGV Static-Pressure Contours: Blunt-Close, 75% Span, $t = T/3$.
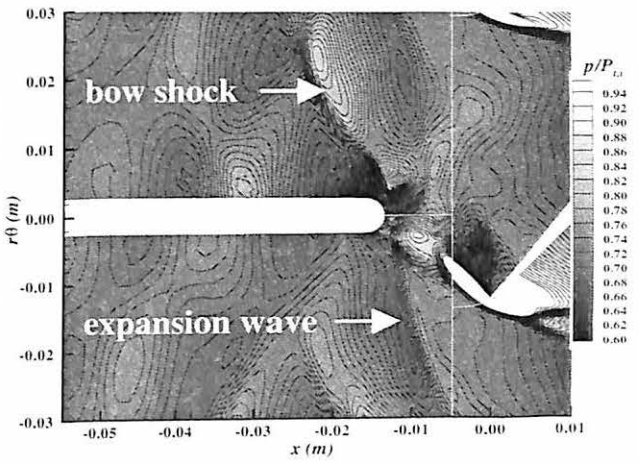
Figure 5-22   IGV Static-Pressure Contours: Blunt-Close, 75% Span, $t = T/2$.

63
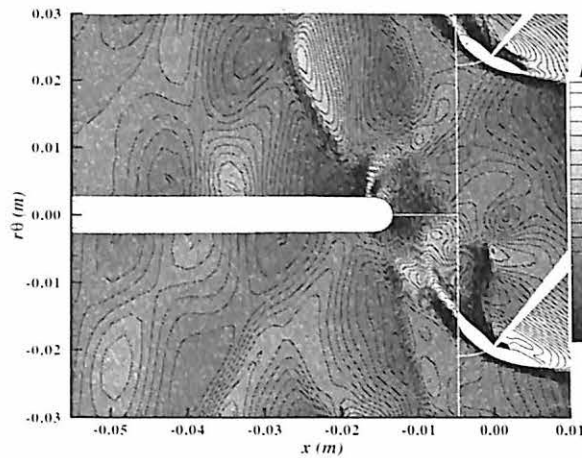
Figure 5-23 IGV Static-Pressure Contours: Blunt-Close, 75% Span, t = 2T/3.
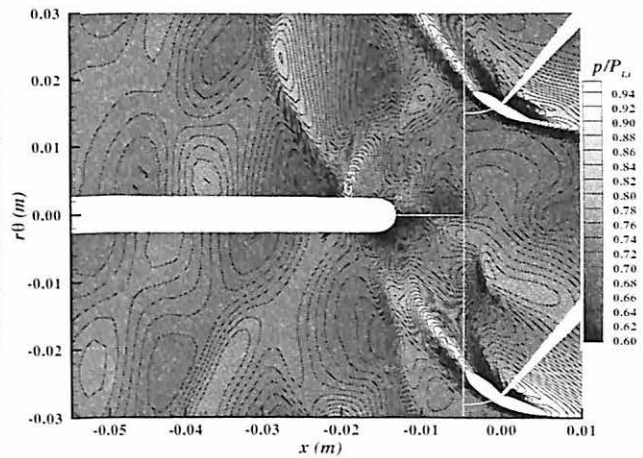
Figure 5-24 IGV Static-Pressure Contours: Blunt-Close, 75% Span, t = 5T/6.

5.5   IGV SURFACE-PRESSURE FIRST-HARMONIC CHORDWISE PHASE

Figure 5-25 and Figure 5-26 show relative phase for the first-harmonic surface-pressure data at the blunt-far and blunt-close IGV conditions, respectively. Each figure displays IGV upper-surface, lower-surface, and differential-pressures phase along the vane chord. Similar data is provided for the sharp-trailing-edge geometry at far-spacing and close-spacing conditions in Figure 5-27 and Figure 5-28, respectively.
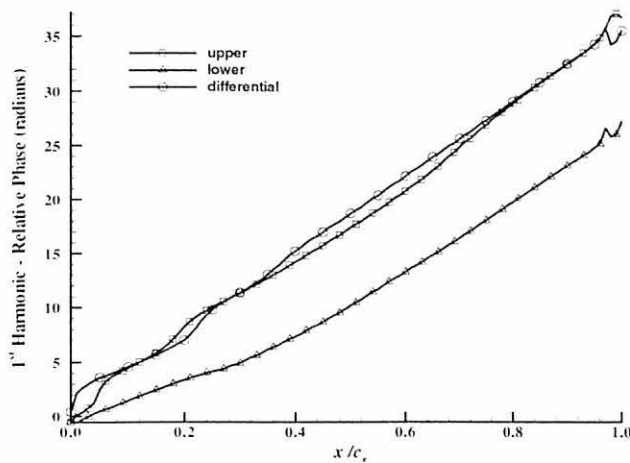
Figure 5-25 1st Harmonic Phase: Blunt-Far.
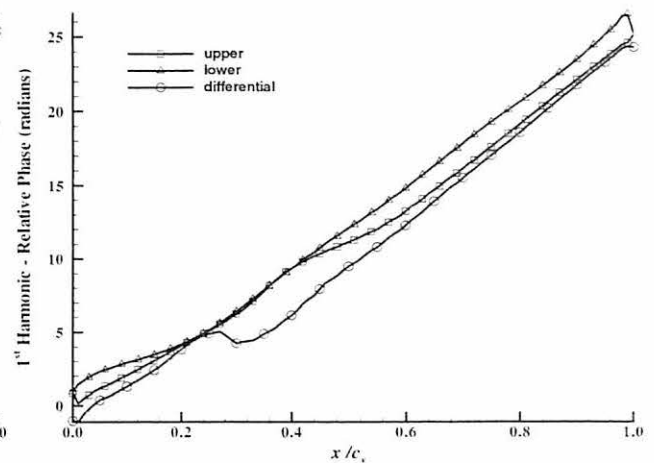
Figure 5-26 1st Harmonic Phase: Blunt-Close.

64
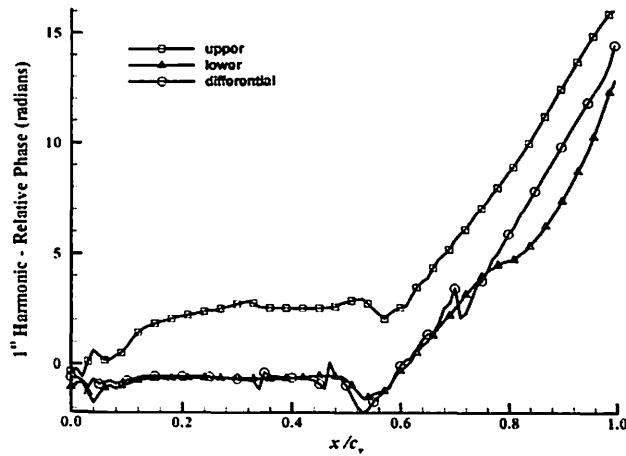
Figure 5-27 1st Harmonic Phase: Sharp-Far.   **Figure 5-28** 1st Harmonic Phase: Sharp-Close.
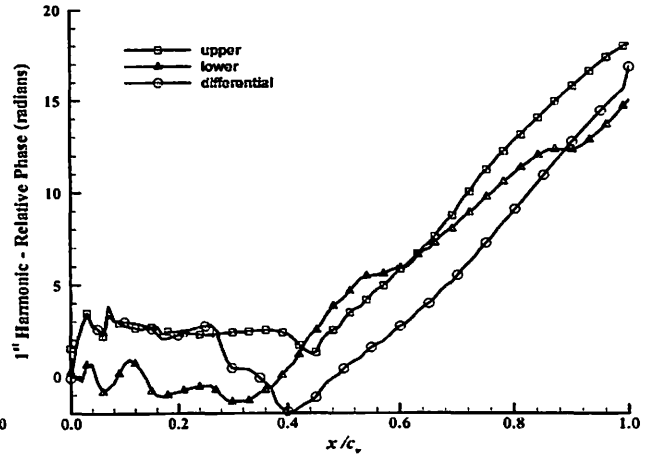
Relative phase information for a rearward-forced vane indicates propagation speeds for the unsteady disturbance along the vane chord (Falk et al., 2001). Therefore, comparing first-harmonic phase data in Figure 4-25 through Figure 4-28 shows consistent upstream disturbance propagation along the entire vane chord for the blunt-IGV cases (as indicated by the constant positive slope of the phase lines). However, unsteady disturbance propagation does not occur along the entire chord for the sharp-IGV case, as the phase slope changes to approximately zero near mod-chord. In fact, disturbance propagation along the sharp IGV stops near 53% and 40% chord for the far-spacing and close-spacing conditions, respectively: the arrested disturbance propagation near the sharp-IGV mid-chord region is attributed to disturbance amplitude decay with chordwise distance, caused by a time-averaged static pressure rise aft of the vane-row minimum throughflow area (see Figure 4-1). The time-averaged static pressure rise along the sharp IGV coincides with rapid rotor-induced disturbance decay, causing disturbance propagation to cease. Disturbance propagation occurs along a greater portion of the vane in the close-spacing configuration because the forcing disturbances are magnified at this condition.

5.6   IGV SURFACE-PRESSURE HIGHER-HARMONIC CHORDWISE

DIFFERENTIAL AMPLITUDE
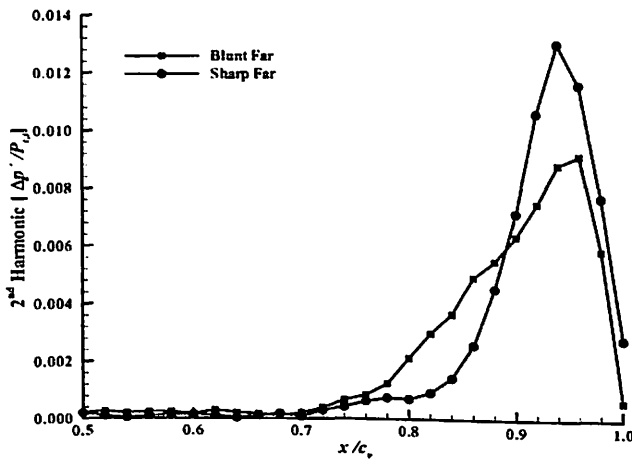
Figure 5-29 2nd Differential Pressure: Far.   Figure 5-30 2nd Differential Pressure: Close.
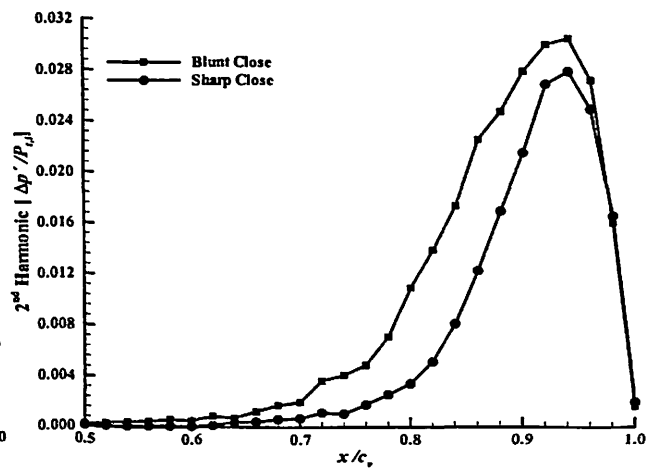
Figure 5-29 and Figure 5-30 provide chordwise unsteady differential-pressure data for the second-harmonic frequency components (i.e., two times the blade-passing frequency) for the far-spacing and close-spacing conditions, respectively. In both cases, pressure amplifies near the IGV trailing-edge region, but decays rapidly with distance upstream, similar to the first-harmonic data. Interestingly, the sharp-IGV case at far-spacing condition (Figure 5-29) exhibits greater maximum second-harmonic amplitude than the blunt-IGV case, contradicting the first-harmonic results. Note, however, that the relative amplitude difference between maxima in Figure 5-29 is small relative to the first-harmonic amplitudes.

Figure 5-31 and Figure 5-32 show unsteady differential pressure at the third harmonic frequency for both the far-spacing and close-spacing cases, respectively. Comparing the second-harmonic and third-harmonic data to the first-harmonic pressures of Figure 5-15 through Figure 5-18, it is clear that the higher-order harmonic pressures tend to decay more rapidly with upstream distance, with the rate of decay increasing with

frequency. Differential pressure reduces to zero directly at the trailing edge for both displayed higher-order harmonic frequencies, although large pressure amplification beyond 90% chord again suggests "singularity-like" pressure behavior in the harmonics. Higher-order harmonics do not display a significant dependence on IGV trailing-edge geometry at close spacing, but more dependence at far spacing.
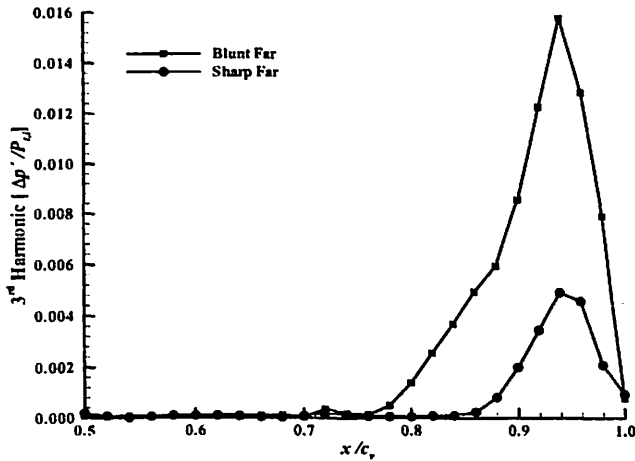
Figure 5-31 3rd Differential Pressure: Far.   Figure 5-32 3rd Differential Pressure: Close.
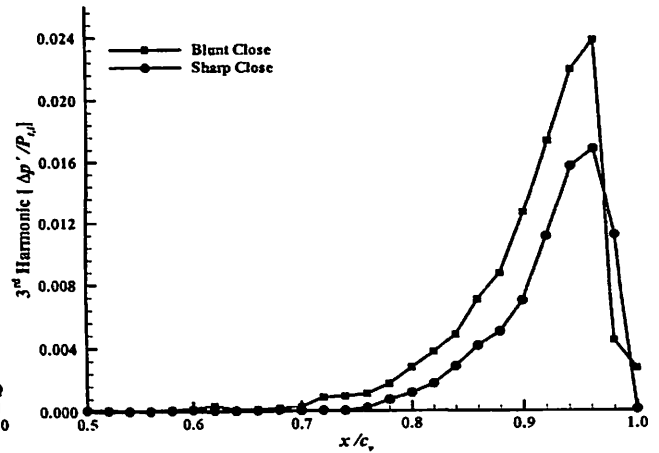
5.7   IGV SURFACE-PRESSURE HIGHER-HARMONIC CHORDWISE DIFFERENTIAL PHASE

Relative-phase data for the differential pressure at second-harmonic and third-harmonic frequencies are shown in Figure 5-33 and Figure 5-34, for the blunt and sharp IGV trailing-edge geometries, respectively. From these figures, it is observed that axial spacing has little effect on phase slope, as the slopes for the far-spacing and close-spacing geometries are relatively constant near the IGV trailing edge. For both the blunt-IGV and sharp-IGV cases, the slope of the third harmonic phase (and second-harmonic, for the sharp IGV) is linear toward the trailing edge, but decays rapidly to zero near $x/c_v = 0.70$. Again, this drastic change in phase slope is attributed to a loss in disturbance strength with upstream propagation distance, as correlated with the data of Figure 5-31 and Figure

67

5-32. Note that the percentage of IGV chord over which the disturbances propagate is reduced with increasing harmonic frequency, corresponding to increased disturbance decay at higher frequencies.
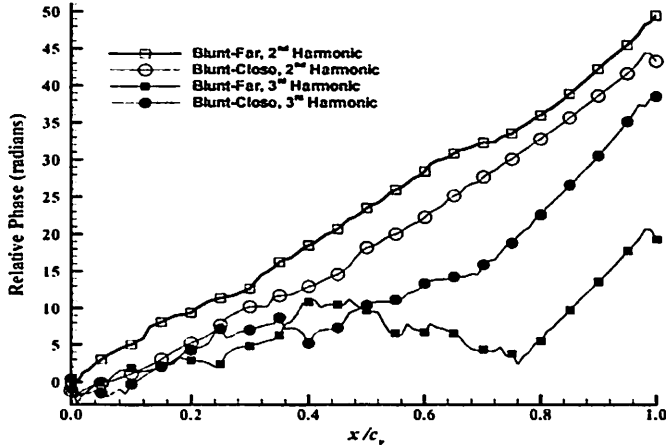
Figure 5-33 Higher-Harmonic Differential Pressure: Blunt.
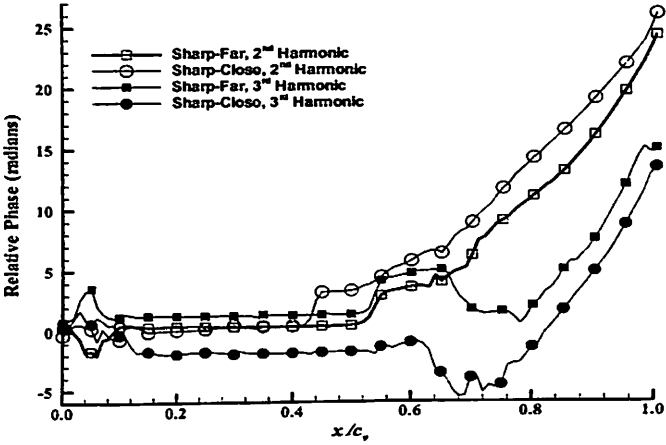
Figure 5-34 Higher-Harmonic Differential Pressure: Sharp.

5.8   IGV FORCING SUMMARY

Unsteady pressure time series on the IGV upper-surface indicate a monotonic pressure phase shift between vane-chord locations, consistent with constant-speed upstream disturbance propagation. These upstream-propagating disturbances exhibit high unsteady pressure amplitudes near the IGV trailing edge, decaying with distance upstream along the IGV surface.

Overall, first-harmonic differential pressures have significant amplitudes at the IGV trailing-edge region, up to 16% of the area-averaged total inlet pressure. First-harmonic pressure data show amplification on the IGV lower surface upstream of the trailing edge, that amplification not being mirrored on the upper surface. Similar results were found by Falk and Darbe (2003) who related it to IGV-row solidity. Chordwise first-harmonic differential pressure also exhibits amplification toward the IGV trailing edge for all examined cases. Despite this pressure amplification, simulation results show

zero differential pressure directly at the trailing edge, disputing the existence of a trailing-edge singularity. However, "singularity-like" pressure behavior near the trailing edge occurs for the blunt-IGV at close-spacing conditions. This "singularity-like" characteristic is attributed to rotor-induced bow shock and low-pressure expansion wave interaction; these disturbances meeting directly at the IGV trailing edge from opposite sides of the IGV surface. Surface-pressure phase results indicate disturbance propagation along the entire vane chord for the blunt-IGV, but arrested propagation along the vane for the sharp-IGV case, corresponding to rapid disturbance decay with upstream distance.

IGV trailing-edge differential pressure exhibited significant harmonic content up to five times the blade-passing frequency. Higher-order harmonic pressures exhibit similar amplification at the IGV trailing edge, to the first-harmonic data. However, higher-order differential-pressure amplitudes decay rapidly along the vane chord at increasing frequencies. Trailing-edge "singularity-like" pressure behavior was exhibited by the second-harmonic and third-harmonic differential-pressure data; however, the differential pressure always reduces to zero at the IGV trailing edge.

6 IGV SPANWISE FORCING RESULTS

This chapter investigates unsteady forcing on the upstream IGV at different spanwise locations. Unsteady forcing is reported in terms of IGV unsteady surface-pressure distribution, spectral content, and phase. The effects of IGV-rotor axial spacing and trailing-edge geometry are considered at different spanwise locations. Unsteady results are obtained in the same manner as described in Chapter 5.

6.1 IGV SURFACE-PRESSURE TIME DEPENDENCY

Figure 6-1 through Figure 6-6 illustrate instantaneous unsteady differential pressure on the blunt-IGV at close-spacing conditions, where the time difference between each figure is one-sixth of a blade-passing period. In the presented figures, spanwise location varies from 0.0 to 1.0, corresponding to the SMI hub-radius and casing-radius, respectively.

In Figure 6-2 the rotor-induced potential disturbance is first seen to affect IGV differential pressure at the hub (as indicated by the small white region). Due to the low rotational velocity of the rotor at this radius, however, the rotor-induced forcing disturbance is relatively weak, causing minimal IGV unsteady pressure amplitude. As time increases one-sixth of a blade-passing period, the unsteady differential pressure grows in strength and affects a larger portion of the IGV trailing edge, as shown in Figure 6-3. Rotor-induced forcing amplifies in the radial direction, as rotor-induced bow shock strength increases with span, causing greater unsteady pressure amplitudes near the IGV mid-span region. After another one-sixth of a blade-passing period, the location of

70

highest unsteady differential pressure moves rapidly along the IGV trailing edge toward the casing, while unsteady pressure disturbances at lower span positions begin to propagate upstream along the IGV chord. The maximum unsteady differential pressure continues to traverse in the spanwise direction as time unfolds, eventually impacting the casing (see Figure 6-5). After impacting the casing, the unsteady pressure disturbance first travels upstream along the casing, but then bounces away from the casing into the flow, as illustrated in Figure 6-1 through Figure 6-4. Overall, the unsteady pressure disturbances affect the entire IGV trailing-edge region; however, the disturbances primarily influence upstream IGV chord locations only at higher spans. Instantaneous unsteady differential plots for the far-spacing conditions can be found in Appendix D.

Figure 6-7 through Figure 6-12 show unsteady differential pressure on the IGV for the sharp trailing-edge geometry at close-spacing conditions. Similar to the blunt-IGV case, the rotor-induced forcing affects the IGV trailing-edge region at the hub first, as seen in Figure 6-7 and Figure 6-8. As the point of maximum differential pressure moves outward toward the casing, unsteady pressure increases in strength around mid-span, before losing strength toward the casing. This mid-span amplification is attributed to increased rotor-induced forcing disturbance near 50% span, as previously noted in Figure 4-32; however the loss of pressure amplitude very near the casing is unexpected. Once reaching the casing, the point of maximum differential pressure again bounces radially inward (see Figure 6-7 through Figure 6-10). Unlike the blunt-IGV minimal unsteady pressure is observed upstream of 50% IGV chord, corresponding to rapid disturbance decay with upstream distance along the sharp IGV, as previously noted in Chapter 5.

Figure 6-1 IGV Unsteady Differential-Pressure Contours: Blunt-Close, $t = 0$.

Figure 6-2 IGV Unsteady Differential-Pressure Contours: Blunt-Close, $t = T/6$.

Figure 6-3 IGV Unsteady Differential-Pressure Contours: Blunt-Close, $t = T/3$.
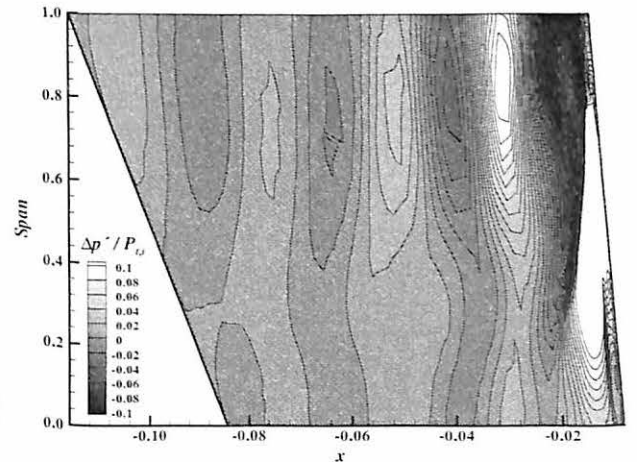
Figure 6-4 IGV Unsteady Differential-Pressure Contours: Blunt-Close, $t = T/2$.
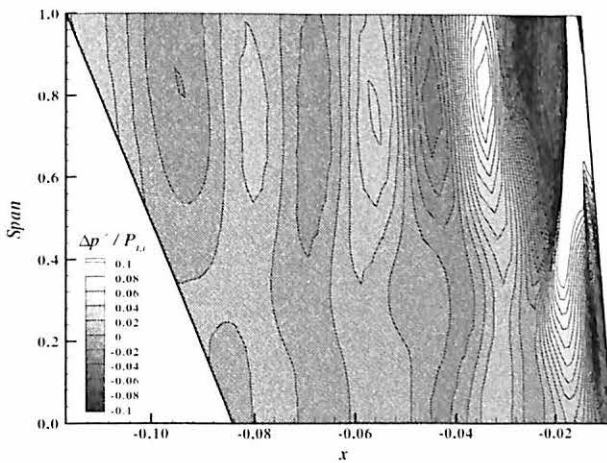
Figure 6-5 IGV Unsteady Differential-Pressure Contours: Blunt-Close, $t = 2T/3$.

Figure 6-6 IGV Unsteady Differential-Pressure Contours: Blunt-Close, $t = 5T/6$.

72

Figure 6-7 IGV Unsteady Differential-Pressure Contours: Sharp-Close, $t = 0$.
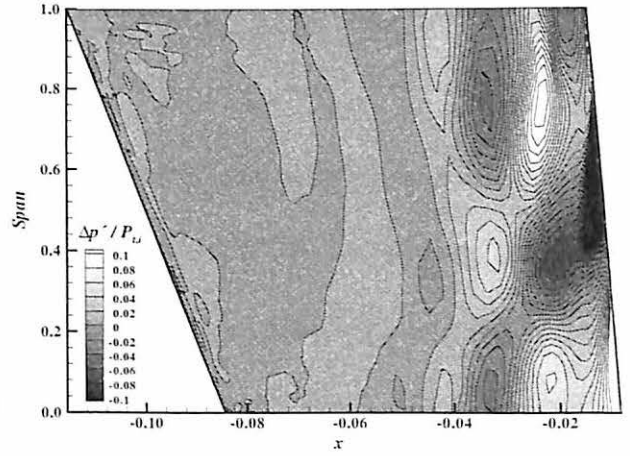
Figure 6-8 IGV Unsteady Differential-Pressure Contours: Sharp-Close, $t = T/6$.
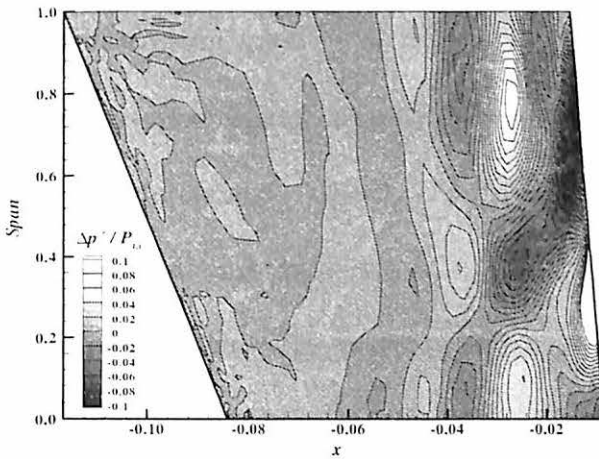
Figure 6-9 IGV Unsteady Differential-Pressure Contours: Sharp-Close, $t = T/3$.
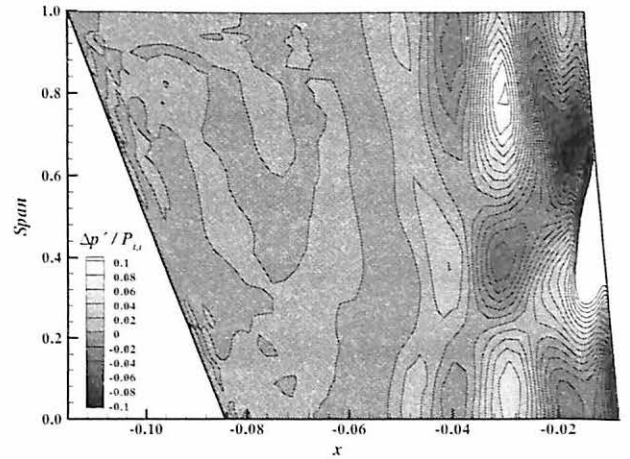
Figure 6-10 IGV Unsteady Differential-Pressure Contours: Sharp-Close, $t = T/2$.
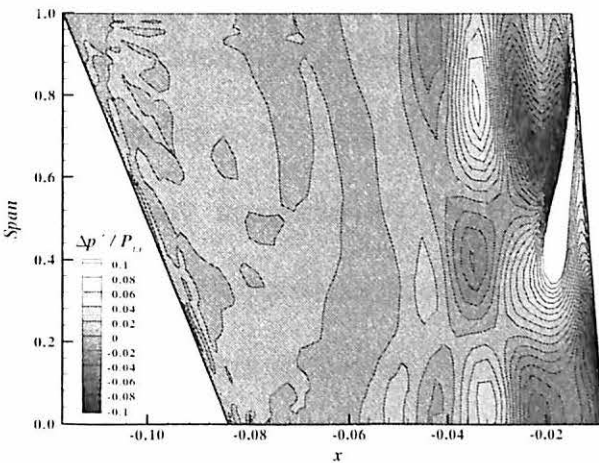
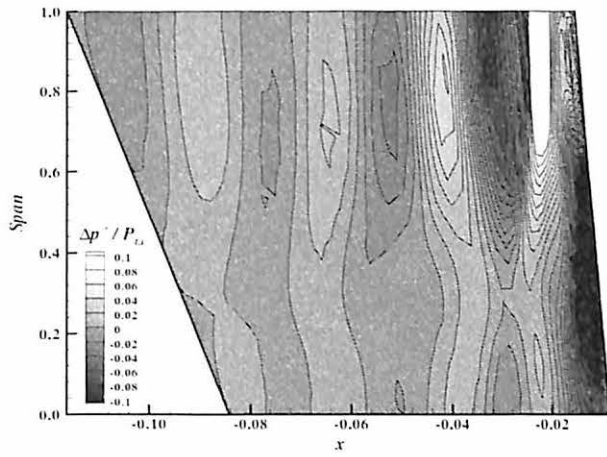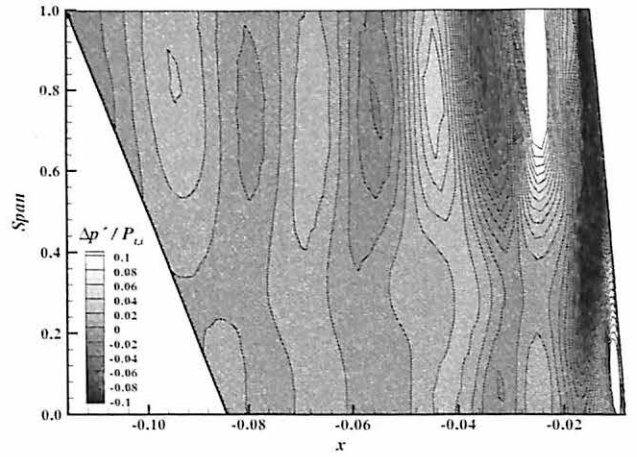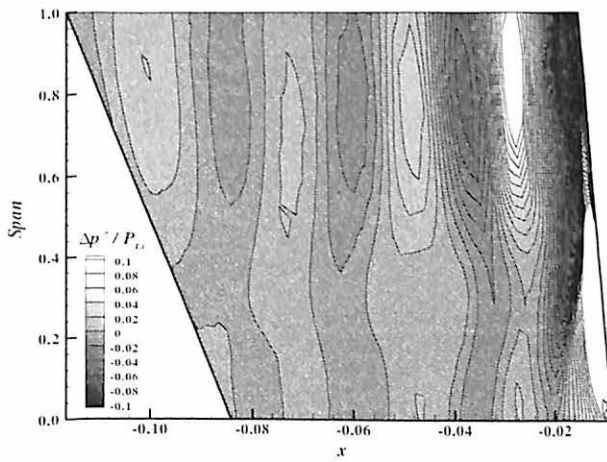**Figure 6-11 IGV Unsteady Differential-Pressure Contours: Sharp-Close, $t = 2T/3$.**
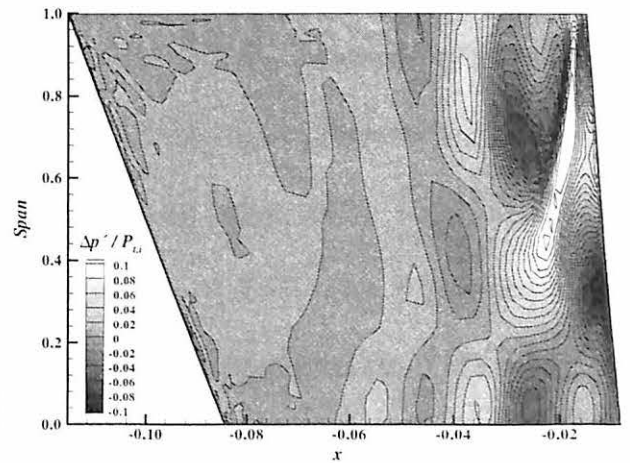
Figure 6-12 IGV Unsteady Differential-Pressure Contours: Sharp-Close, $t = 5T/6$.
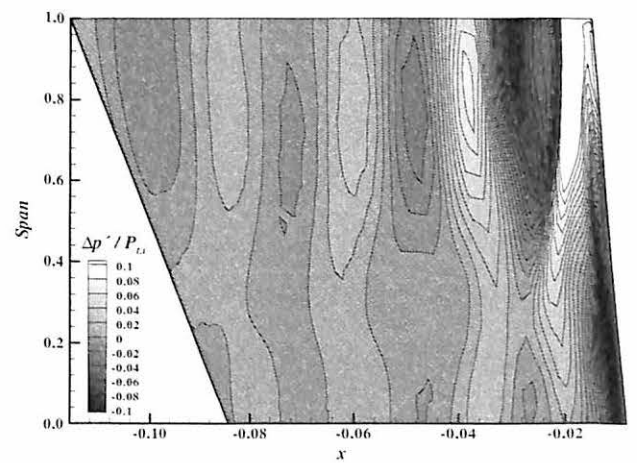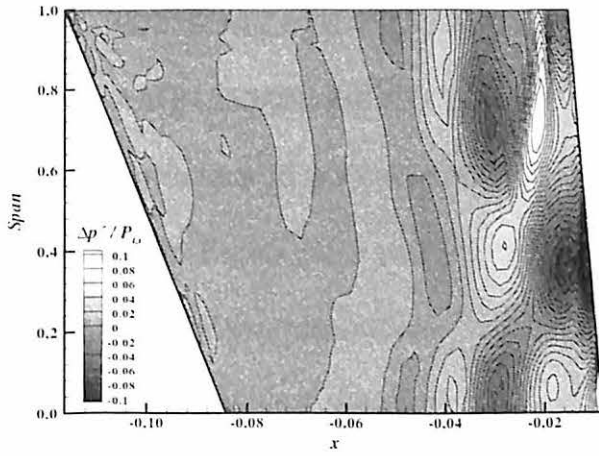
73

6.2 IGV SURFACE-PRESSURE FIRST-HARMONIC DIFFERENTIAL AMPLITUDE DEPENDENCY

Variations in IGV differential-pressure first-harmonic amplitude with span are illustrated in Figure 6-13 and Figure 6-14, for the blunt IGV at far-spacing and close-spacing conditions, respectively. The first-harmonic amplitudes are significantly stronger for the close-spacing condition, and show a dramatic pressure rise toward the trailing edge at higher span locations, as previously noted in Figure 5-15 through Figure 5-18. At both spacing conditions, first-harmonic unsteady differential pressures generally increase with increasing span. This is expected due to the stronger rotor-induced bow waves in the outer-span region, caused by increasing blade rotational velocity with radius.

Interestingly, significant trailing-edge differential-pressure amplification occurs in the blunt-far case near $x/c_v = 0.97$ at all span locations, with the 25% and 50% span locations showing the most amplification. Such trailing-edge pressure amplification is attributed to the rounded shape of the blunt-IGV trailing edge for two reasons. First, the first-harmonic differential-pressure spikes at the IGV trailing edge do not occur in the sharp-IGV data (see Figure 6-17 and Figure 6-18 below), but occur in all blunt-IGV data. Second, trailing-edge pressure amplification only occurs beyond $x/c_v = 0.97$, corresponding to the location at which blunt-IGV trailing-edge curvature begins. In all, the unsteady separated flow at the blunt-IGV trailing edge cases significant time-dependent differential pressure to develop beyond $x/c_v = 0.97$. As illustrated in the entropy contours of Figure 6-15, for the close-spacing condition at 75% span, the hemispherical trailing-edge shape induces flow separation from the IGV. In turn, the separation flow region causes pressure rise, or base drag, at the vane trailing edge.

Moreover, this separation-induced pressure rise is time dependent in nature, as illustrated in the instantaneous pressure contour of Figure 6-16, and thus does not appear in the time-averaged static pressure data of Figure 4-5. Trailing-edge pressure rise time dependency is attributed to observed vortex shedding off the blunt-IGV trailing edge at the blade-passing frequency,

First-harmonic unsteady differential pressures for the blunt-IGV close-spacing case in Figure 6-14 also demonstrate increasing trailing-edge amplitudes beyond x/c_v = 0.95 for all span locations. This trailing-edge pressure amplification can again be attributed to an unsteady separation-induced pressure rise, or base drag, over the hemispherical trailing-edge shape. At the close-spacing condition, however, the trailing-edge pressure rise is also related to previously discussed (Chapter 5) interaction between the high-pressure bow-shock and low-pressure expansion wave directly at the IGV trailing edge (particularly at 25% span). Notably, the first-harmonic differential pressure is larger in amplitude for 25% span location compared to the 50% span location from x/c_v = 0.75 to x/c_v = 0.90.
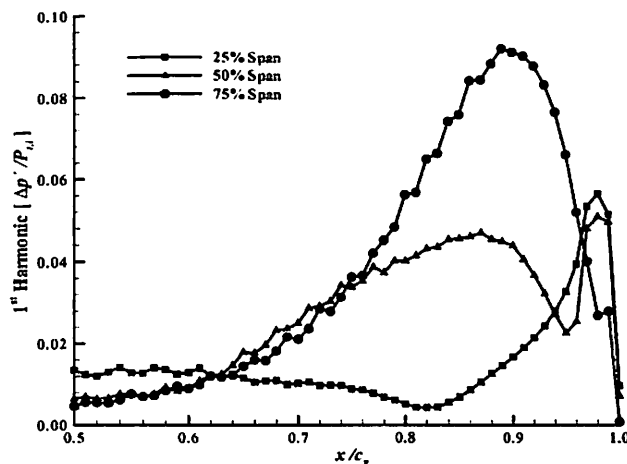
Figure 6-13 First-Harmonic Differential
Pressure: Blunt-Far.
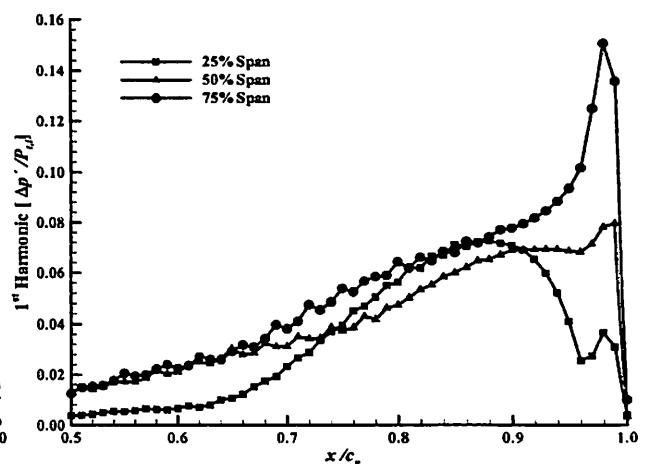
Figure 6-14 First-Harmonic Differential
Pressure: Blunt-Close.
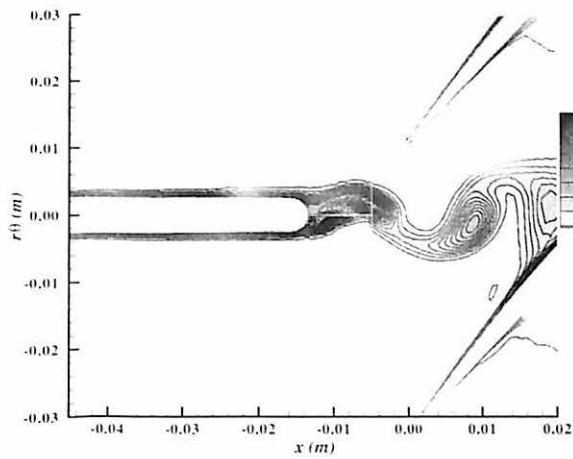
Figure 6-15 Instantaneous Entropy Contours: Blunt-Close.
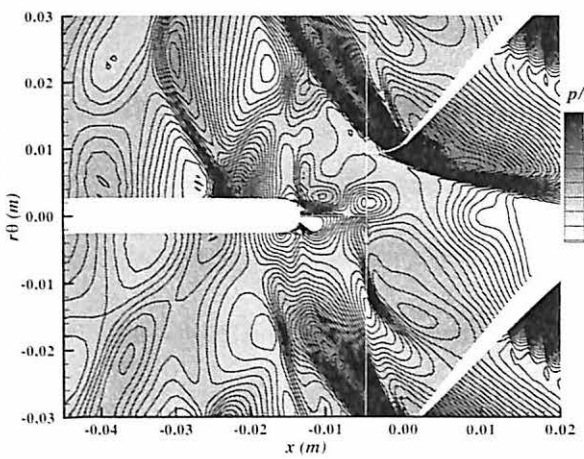
Figure 6-16 Instantaneous Static-Pressure Contours: Blunt-Close.
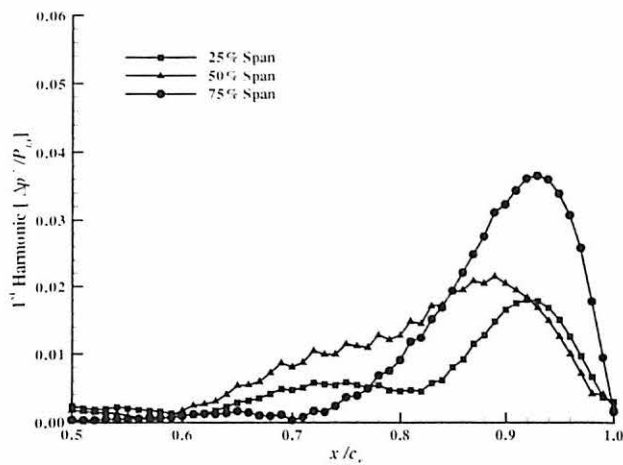
Figure 6-17 First-Harmonic Differential Pressure: Sharp-Far.
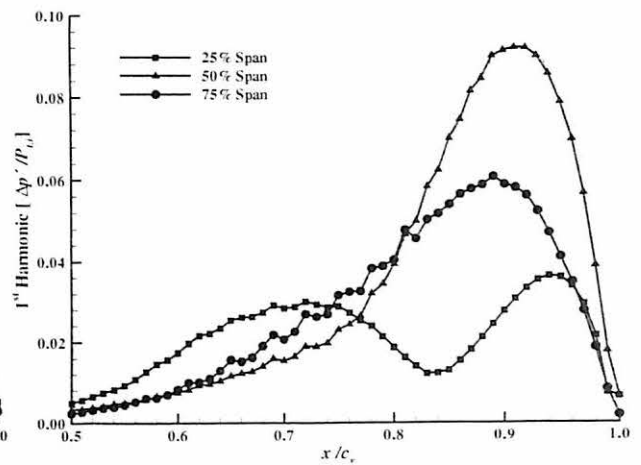
Figure 6-18 First-Harmonic Differential Pressure: Sharp-Close.

Figure 6-17 and Figure 6-18 illustrate first-harmonic differential unsteady pressure on the sharp-IGV aft-half chord at far-spacing and close-spacing conditions, respectively. Comparing the sharp-IGV data with the blunt-IGV data of Figure 6-13 and Figure 6-14, the overall pressure amplitudes are observed to be less for the sharp-IGV cases. In addition, there is no presence of an abrupt trailing-edge pressure amplification beyond $x/c_v = 0.97$ for the sharp-IGV, suggesting the blunt-IGV geometry causes the previously observed trailing-edge pressure spikes. The sharp-IGV 25% span location has

76

a local minimum at $x/c_v = 0.80$ and $x/c_v = 0.84$ for the far-spacing and close-spacing conditions, respectively. This behavior may be attributed to flow separation affects on the sharp IGV, as noted in Chapter 4 at 25% span. At close spacing, the sharp-IGV also exhibits higher first-harmonic differential pressure at 50% span, possibly due to greater rotor-induced forcing disturbances that occur at 50% span for the sharp-IGV case as shown in Figure 4-32.

6.3 SURFACE-PRESSURE FIRST HARMONIC DIFFERENTIAL PHASE

Figure 6-19 and Figure 6-20 show relative-phase data for the first-harmonic unsteady differential pressure at three spanwise locations along the blunt-IGV at both far-spacing and close-spacing conditions, respectively. Unsteady pressure is observed to travel across the entire length of the IGV chord for all cases, with the unsteady differential pressure traveling slightly faster for the close-spacing condition. Similarly, Figure 6-21 and Figure 6-22 show relative-phase data for the first-harmonic unsteady differential pressure, at the sharp-IGV far-spacing and close-spacing conditions, respectively. The far-spacing condition indicates unsteady pressures do not travel the full length of the IGV chord, stopping around $x/c_v = 0.30$ where the time-averaged static pressure exhibits a strong adverse pressure gradient (see Figure 4-7) in the upstream direction. This is not as evident for the close-spacing condition, as the relative-phase data indicate disturbance propagation along the entire IGV-chord at 50% span, but near-zero disturbance propagation upstream of $x/c_v = 0.3$ at 25% and 75% span. The lack of phase-slope decay at 50% span is further supported by the forcing-function data in Figure 4-32, showing the strongest sharp-IGV forcing function at 50% span. A stronger forcing function allows the disturbance to propagate further upstream through the sharp-IGV

adverse pressure gradient near $x/c_v = 0.3$. The sharp-IGV far-spacing relative-phase results also suggest disturbance propagation speeds to be a function of time-averaged vane-passage pressure gradient, as the 50% span location experienced both the highest time-averaged pressure gradient (Figure 4-7) and the fastest propagation speed.
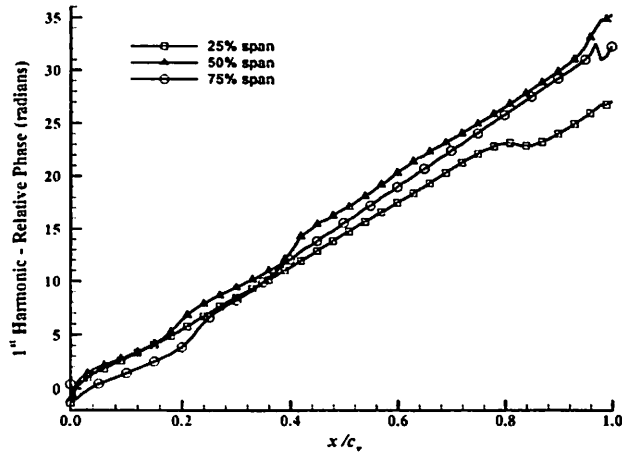
Figure 6-19   First-Harmonic Relative Phase: Blunt-Far.
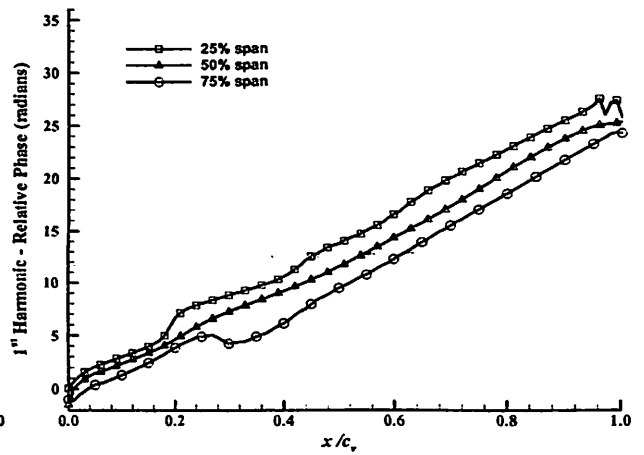
Figure 6-20   First-Harmonic Relative Phase: Blunt-Close.
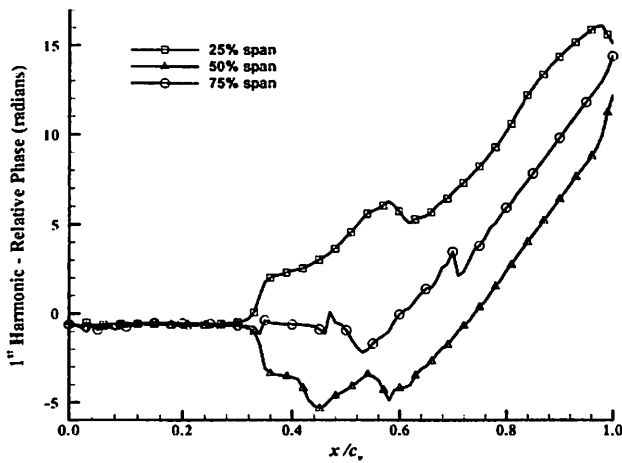
Figure 6-21   First-Harmonic Relative Phase: Sharp-Far.

Figure 6-22   First-Harmonic Relative Phase: Sharp-Close.

6.4 IGV SURFACE-PRESSURE HIGHER-HARMONIC DIFFERENTIAL AMPLITUDE

Figure 6-23 and Figure 6-24 illustrate amplitudes for the unsteady differential-pressure second-harmonic frequency component along the blunt-IGV aft-half chord for the far-spacing and close-spacing conditions, respectively. At the far-spacing condition, trailing-edge amplification is greatest at 50% span. This is not as evident at the close-spacing condition, as the second-harmonic differential pressure is only slightly larger for the 50% span location as compared to the 75% span location. Similar second-harmonic amplitudes are depicted in Figure 6-25 and Figure 6-26 for the sharp-IGV at far-spacing and close-spacing conditions, respectively. Unlike the blunt-IGV case, both axial locations indicate that the 75% span location yields the highest second-harmonic pressure amplitudes. For the sharp-IGV at both axial locations, and the blunt-IGV at far spacing, the 25% spanwise location shows relatively insignificant pressure amplitudes. Overall, the sharp-IGV amplitudes are less than those of the blunt-IGV case.
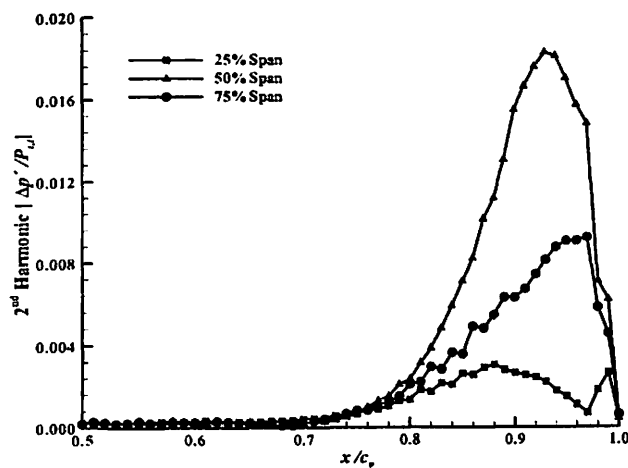
Figure 6-23   Second-Harmonic Differential Pressure: Blunt-Far.
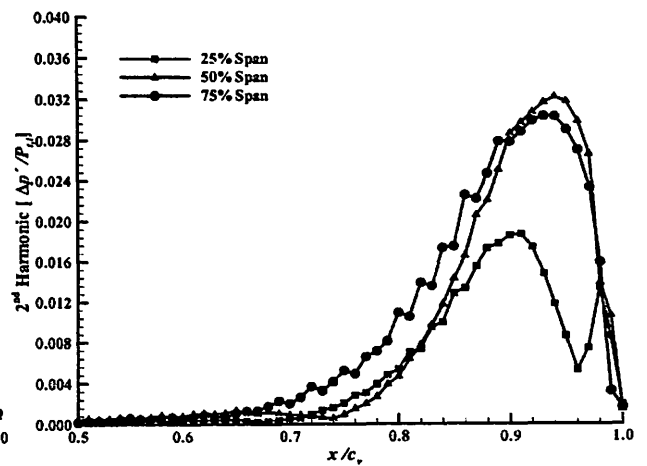
Figure 6-24   Second-Harmonic Differential Pressure: Blunt-Close.
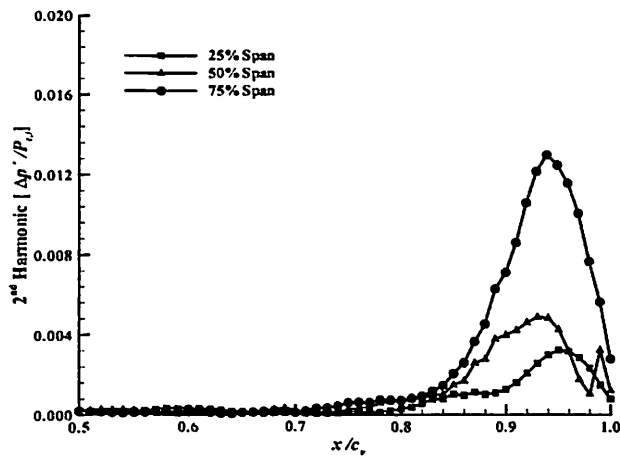
**Figure 6-25 Second-Harmonic Differential
Pressure: Sharp-Far.**
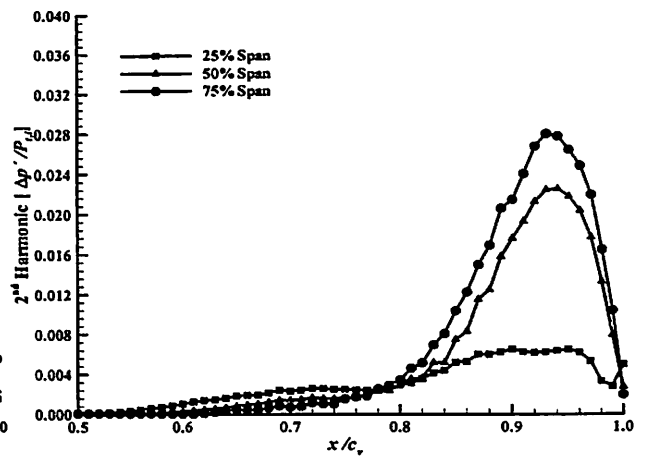
**Figure 6-26 Second-Harmonic Differential
Pressure: Sharp-Close.**

Figure 6-27 and Figure 6-28 contain unsteady differential-pressure third-harmonic

data along the blunt-IGV aft-half chord for the far-spacing and close-spacing conditions,

respectively. Similar third-harmonic amplitude data are depicted in Figure 6-29 and

Figure 6-30 for the sharp-IGV at far-spacing and close-spacing conditions, respectively.

All cases indicate an increase in trailing-edge amplitude with increasing span, with the

exception of the sharp-IGV at the close-spacing condition, where the 50% spanwise

location yields the highest unsteady differential-pressure amplification, possibly due to a

higher rotor-induced forcing at this location (as indicated in Figure 4-32). Again, blunt-

IGV pressure magnitudes are observed to be larger than the corresponding sharp-IGV

cases. Third-harmonic unsteady pressure amplification at all span location also focuses

closer to the vane trailing-edge region than the corresponding lower-order harmonics,

with almost no unsteady pressure visible upstream of $x/c_v = 0.70$. Comparing third-

harmonic amplitudes with those of the first-harmonic and second-harmonic data, pressure

amplitude clearly decreases with increasing harmonic frequency.
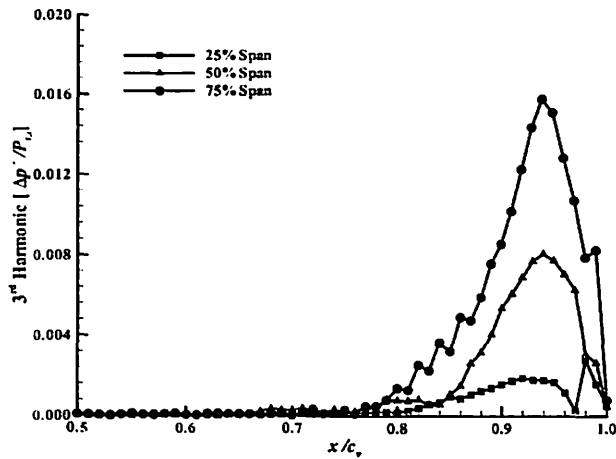
Figure 6-27 Third-Harmonic Differential Pressure: Blunt-Far.
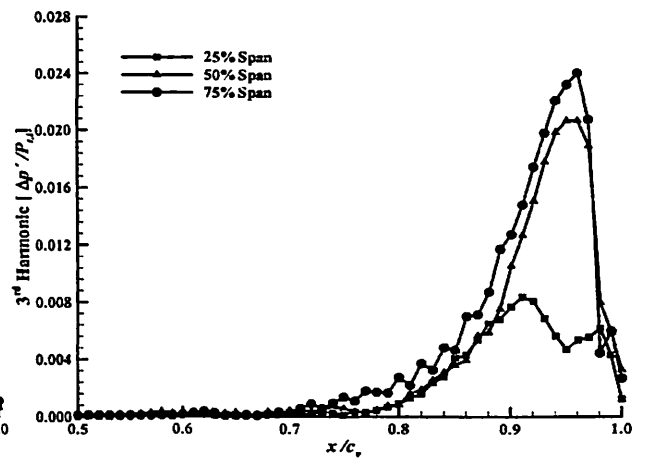
Figure 6-28 Third-Harmonic Differential Pressure: Blunt-Close.
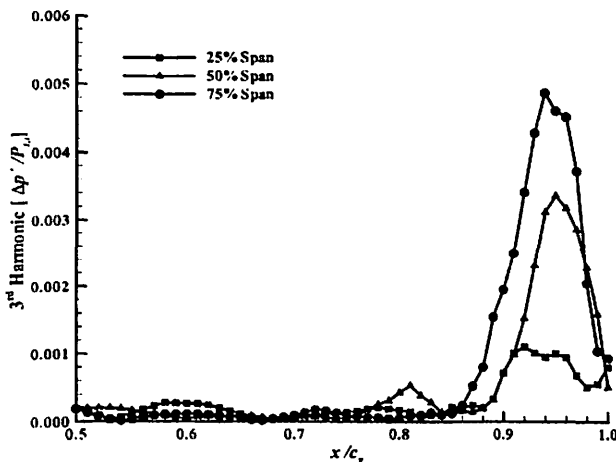
Figure 6-29 Third-Harmonic Differential Pressure: Sharp-Far.
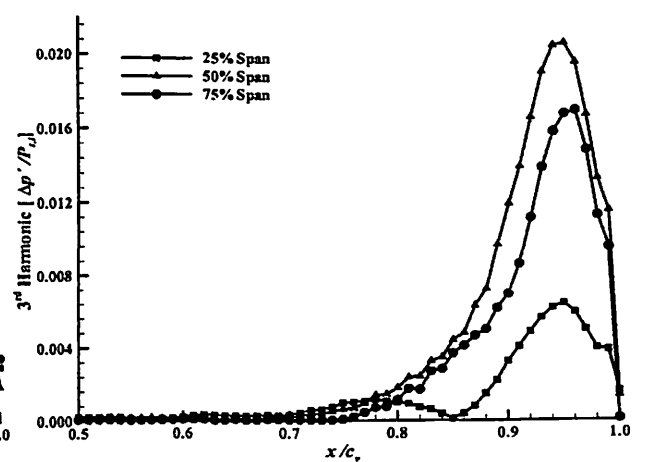
Figure 6-30 Third-Harmonic Differential Pressure: Sharp-Close.

6.5   SURFACE-PRESSURE HIGHER-HARMONIC DIFFERENTIAL PHASE

Relative-phase data for unsteady differential pressures at different IGV span locations are shown in Figure 6-31 and Figure 6-32 at the blunt-IGV far-spacing and close-spacing conditions, respectively. Rotor-induced pressure disturbances are observed to travel slower for the far-spacing condition as compared to the close-spacing condition; indicated by the slightly larger slope of the relative phase (Falk, 2000). For both axial-spacing conditions, the second-harmonic phase propagates along the entire length of the

blunt-IGV chord. When compared with the first-harmonic phase of Figure 6-19 and Figure 6-20, the second-harmonic unsteady pressures propagate at higher speeds, as would be expected due to their higher wave number (Falk, 2000).
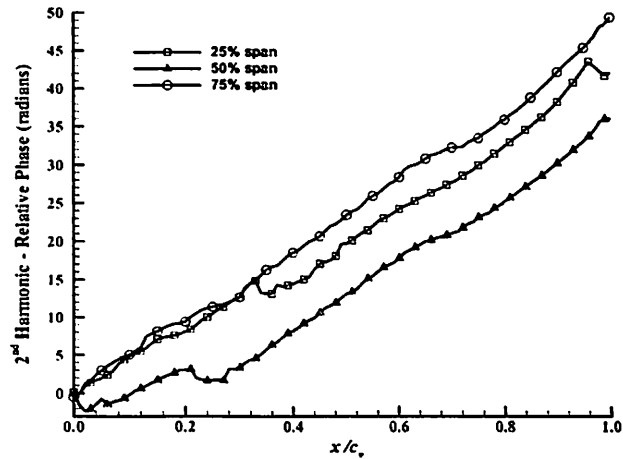
Figure 6-31   Second-Harmonic Relative Phase: Blunt-Far.
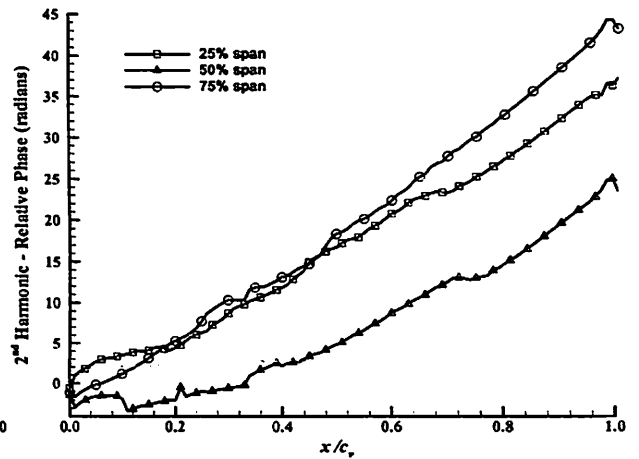
Figure 6-32   Second-Harmonic Relative Phase: Blunt-Close.

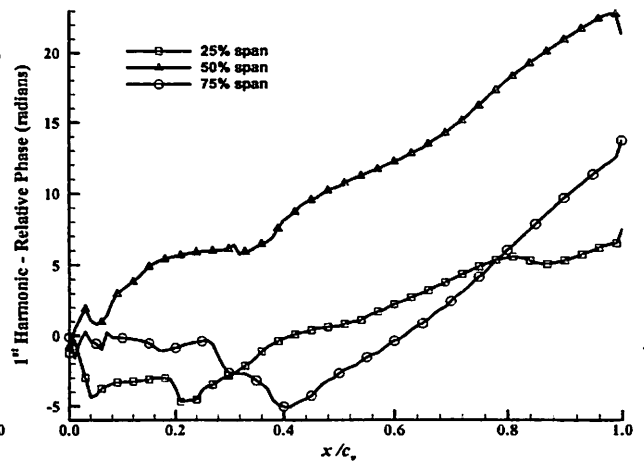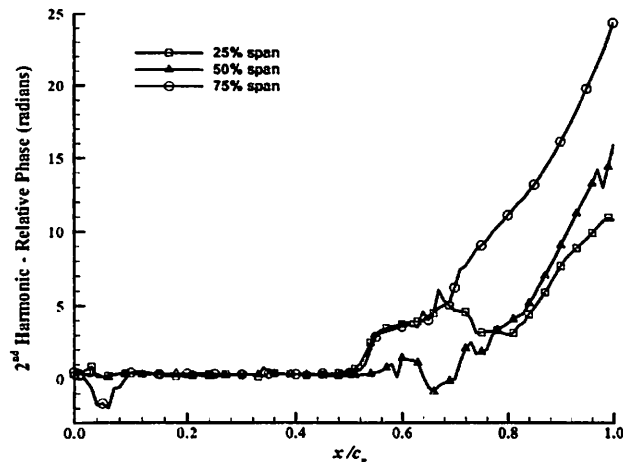**Figure 6-33   Second-Harmonic Relative Phase: Sharp-Far.**
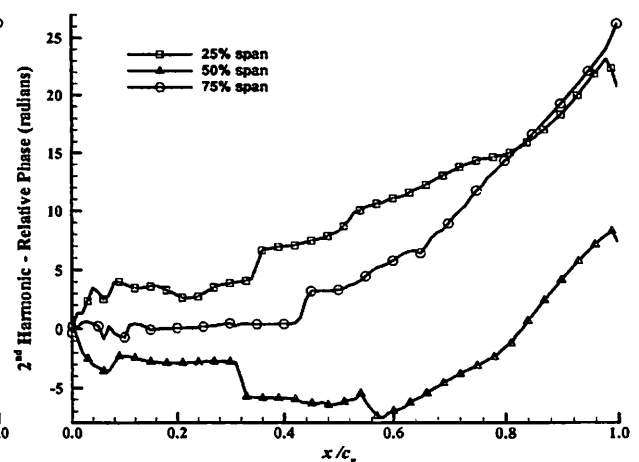
Figure 6-34   Second-Harmonic Relative Phase: Sharp-Close.

Figure 6-33 and Figure 6-34 show second-harmonic relative-phase data for the sharp-IGV at far-spacing and close-spacing conditions, respectively. At the far-spacing condition, unsteady differential pressure is observed to stop propagating near $x/c_v = 0.5$ as related to disturbance decay with upstream distance. Conversely, at the close axial-spacing condition disturbances are observed to travel nearly the entire length of the

sharp-IGV chord at 25% span, and much further upstream at other span locations than the far-spacing condition. Again, this is attributed to stronger IGV forcing disturbances at the close-spacing condition as compared to far spacing.
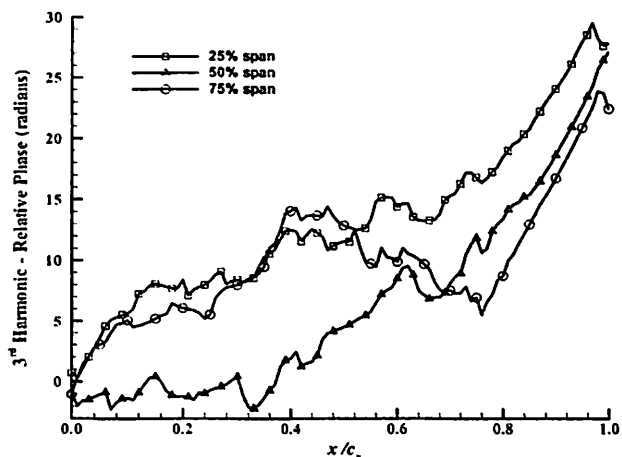
Figure 6-35   Third-Harmonic Relative Phase: Blunt-Far.
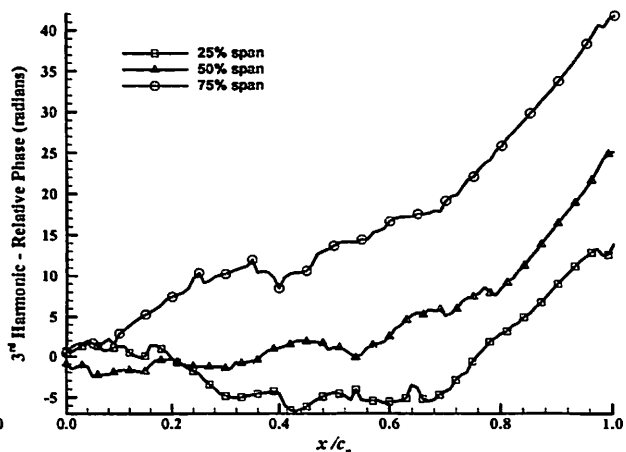
Figure 6-36   Third-Harmonic Relative Phase: Blunt-Close.
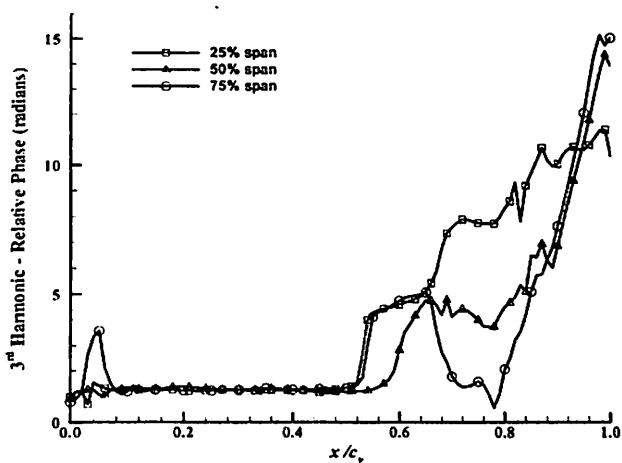
Figure 6-37   Third-Harmonic Relative Phase: Sharp-Far.
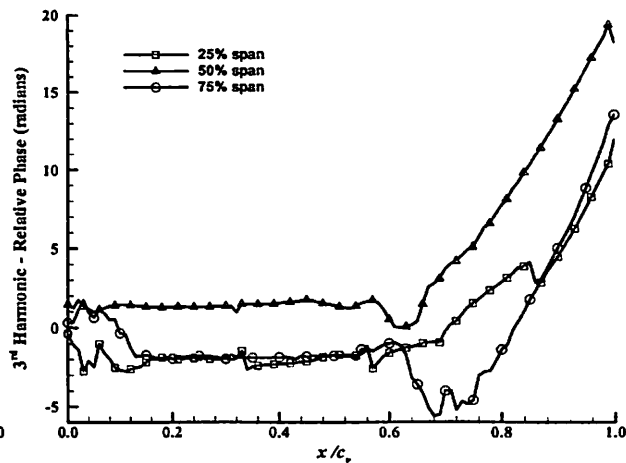
Figure 6-38   Third-Harmonic Relative Phase: Sharp-Close.

Third-harmonic relative-phase data for the unsteady differential pressure are shown in Figure 6-35 and Figure 6-36 at the blunt-IGV far-spacing and close-spacing conditions, respectively. For the far-spacing condition, phase is observed to change across the entire blunt-IGV chord. However, this is not the case for the close-spacing condition where the 25% and 75% spanwise locations indicate the phase to slow down

tremendously. Corresponding phase data for the sharp-IGV third-harmonic frequency are shown in Figure 6-37 and Figure 6-38 at the far-spacing and close-spacing conditions, respectively. Again, phase is observed to stop changing along the sharp-IGV chord, corresponding to disturbance decay related to the vane-passage pressure gradients.

6.6   SPANWISE FORCING SUMMARY

This chapter explores the spanwise variation of IGV rearward forcing. First-harmonic differential pressure is observed to increase with span for all cases, except for the sharp-IGV at close-spacing conditions where mid-span amplification is greatest. Mid-span pressure amplification is attributed to stronger rotor-induced forcing disturbances near 50% span. Overall, first-harmonic pressure characteristics indicate larger trailing-edge unsteady loading for the blunt-IGV geometry, and close-spacing conditions, when compared to the sharp-IGV geometry and far-spacing conditions, respectively. Interestingly, the first-harmonic blunt-IGV data show sharp pressure amplification in the trailing-edge region beyond $x/c_v = 0.97$; this pressure spike is not observed in the sharp-IGV case. Such trailing-edge pressure amplification is attributed, in part, to unsteady flow separation caused by the rounded trailing-edge geometry of the blunt-IGV, as pressure amplification was only observed in this region.

First-harmonic phase results indicate rotor-induced disturbance propagation ceases for the sharp-IGV far-spacing condition upstream of $x/c_v = 0.3$, corresponding to an area of increasing time-averaged pressure on the sharp IGV. The sharp-IGV far-spacing relative-phase results also suggest disturbance propagation speeds to be a function of time-averaged vane-passage pressure gradient, as the 50% span location experienced both the highest time-averaged pressure gradient and the fastest propagation

speed. Relative-phase data for the blunt-IGV suggests disturbance propagation across the entire IGV, characteristic of no vane-passage pressure gradients or time-averaged aerodynamic loading.

Higher-harmonic amplitudes increase in the IGV trailing-edge region, and also show an overall increase in pressure magnitude with span. Second-harmonic and third-harmonic content also exhibits less differential-pressure amplitude than the first-harmonic pressure and decays quicker with upstream distance.

7 SUMMARY AND CONCLUSIONS

Numerical simulations of the IGV-rotor compression stage in the SMI rig located at AFRL were conducted using the CFD algorithm MSU-TURBO. Time-accurate results were analyzed for two different IGV trailing-edge geometries, as well as two IGV-rotor axial-spacing conditions. The original IGV geometry possessed a "blunt" trailing edge, designed to produce aerodynamic losses through base drag typical of those found in an embedded compressor stage. A new IGV geometry was also examined, utilizing a sharp trailing-edge design more typical of modern compressor vanes. The sharp trailing-edge IGV row produced aerodynamic losses though a high camber profile, resulting in diffusion-induced wake production.

Time-averaged static pressure results from MSU-TURBO indicate the sharp-IGV to be aerodynamically loaded and the blunt-IGV to be aerodynamically unloaded, as expected. When comparing time-averaged blunt-IGV results at 75% span for the close and far IGV-rotor spacing conditions, a decrease in IGV trailing-edge static pressure was observed with reduced axial spacing. A similar decrease in time-averaged static pressure was not observed for the sharp-IGV case, indicating an IGV-geometry dependence on rotor bow-shock impingement and unsteady fluid-structure interaction at the IGV trailing edge. Interestingly, the time-averaged static pressure decrease for the blunt-IGV was span dependent, strengthening the supposition that stronger nonlinear fluid-structure interactions caused by bow-shock impingement occur toward the casing.

Wakes developed from the different IGV geometries and IGV-rotor axial spacings were compared. Differences in wake characteristics influence rotor inlet incidence angle. In turn, changes in rotor incidence angle result in different rotor loadings conditions, particularly at the leading edge. Time-averaged static pressure distributions along the rotor chord indicate greater differential pressure at the rotor leading edge for the blunt-IGV cases, with the exception of the sharp-IGV case at 25% span, where flow separation on the upstream IGV was present. Observed differences in rotor loading conditions correspond to different rotor-emitted potential fields, or bow-shock characteristics. As such, rotor-induced potential disturbances are a function of both IGV trailing-edge geometry and axial-spacing conditions. Potential disturbance strength is observed to be stronger at larger spanwise locations for both sharp-IGV and blunt-IGV cases. Relative disturbance angle is also observed to increase with increasing spanwise location. Axial-spacing effects on rotor-induced pressure disturbances are also observed at all spanwise location for the blunt-IGV case; however, the sharp-IGV shows little difference in the rotor-emitted pressure disturbances between far-spacing and close-spacing conditions, except at 25% span where upstream IGV flow separation was observed.

Unsteady pressure time-series data along the IGV upper surface indicate a monotonic phase shift between vane-chord locations, consistent with constant-speed upstream disturbance propagation. Higher unsteady pressure amplitudes consistently occur at the IGV trailing edge, but decay with distance upstream on the IGV surface.

First-harmonic IGV differential-pressure results show a significant magnitude at the trailing-edge region for all cases. For the blunt-close case at 75% span IGV trailing-edge differential pressure amplitude was around 16% of the area-averaged inlet total

pressure. First-harmonic IGV surface-pressure results show pressure amplification on the IGV lower surface between $x/cv = 0.78 - 0.92$ which is not mirrored on the upper surface. This phenomenon has previously been related to IGV-row solidity. First-harmonic differential pressure along the IGV also exhibits amplification toward the trailing edge for all cases. Despite this pressure amplification, all simulations show zero differential pressure directly at the IGV trailing edge (i.e., $x/c_v = 1.0$), disputing the existence of a trailing-edge singularity. However, "singularity-like" trailing-edge pressure behavior occurs for the blunt-IGV at close-spacing conditions, for all harmonic frequencies. This "singularity-like" behavior is attributed to unsteady base drag pressure characteristics and the coexistence of a rotor bow-shock and low-pressure expansion wave in the forcing flow, these disturbances being in phase at the IGV trailing edge but forcing opposite IGV surfaces. Finally, relative-phase results indicate first-harmonic disturbances propagate along the entire length of the vane chord for the blunt-IGV case, but stop near mid-chord for the sharp-IGV case. Arrested disturbance propagation in the sharp-IGV case is attributed to rapid disturbance decay in the upstream direction, caused by a strong time-averaged static pressure gradient.

Higher-order harmonic IGV-surface pressures show similar pressure amplification at the IGV trailing edge as the first-harmonic data, with significant harmonic content occurring up to five times the blade-passing frequency. However, higher-order harmonic differential pressures decay more rapidly with upstream distance, with decay rates increasing with frequency.

Overall, spanwise results indicate a greater unsteady differential pressure with increasing span, expect for the sharp-IGV close-spacing condition where rotor-induced

forcing is largest near 50% span. The blunt-IGV exhibits a first-harmonic pressure spike in the trailing-edge region aft of $x/c_v = 0.97$, at all span locations and both axial-spacing conditions. Such pressure spikes were not observed for the sharp-IGV case and thus are attributed to flow separation caused by trailing-edge geometry. First-harmonic relative-phase results indicate rotor-induced disturbances propagate the entire length of the blunt-IGV at similar speeds at all span locations, indicative of similar time-averaged IGV loading with span. However, sharp-IGV time-averaged aerodynamic loading exhibits significant influence on first-harmonic phase data. Larger chordwise time-averaged pressure gradients result in unsteady disturbance propagation differences, as compared to the blunt-IGV case with no time-averaged vane-passage pressure gradients. Higher-order harmonics also exhibit higher unsteady differential-pressure amplitudes with increasing span.

7.1 CORRELATIONS WITH PREVIOUS INVESTIGATIONS

Sanders et al. (1998) reported increasing IGV surface-pressure amplitude at decreased IGV-rotor axial spacings for an aerodynamically loaded IGV with sharp trailing-edge geometry. Similarly, a symmetric IGV with a blunt trailing-edge geometry also exhibited increasing surface-pressure amplitude with decreasing IGV-rotor axial spacing as reported by Probasco et al. (2000), Koch et al. (2000), and Gorrell et al. (2002b). Overall, previous experimental investigations correlate with both the blunt-IGV and sharp-IGV cases presented here, which exhibited increasing IGV differential pressure with decreased IGV-rotor axial spacing.

In the present investigation, all cases exhibited significant upper-surface pressure amplitudes near the IGV trailing edge, decaying upstream along the IGV chord.

Significant upper-surface pressure harmonics were reported up to five times the rotor-passing frequency. Supporting these results, significant IGV upper-surface pressure amplitudes toward the trailing-edge region were reported by Falk et al. (2000), Sanders et al. (1998), Koch et al. (2000), and Probasco et al. (2000). In all previous investigations, the magnitude of the surface pressure also decreased with upstream distance along the IGV chord. Both Falk et al. (2000) and Sanders et al. (1998) found significant harmonic content in the surface-pressure fluctuations, with greater harmonic-content amplitudes occurring toward the IGV trailing edge, and thus supporting the harmonic-content data presented in the present investigation.

Sanders et al. (2000) reported shock segment reflection on a sharp IGV that propagated upstream and migrated toward the adjacent IGV pressure surface. This phenomenon is also observed in the present investigation as outlined in Section 5.3. Koch et al. (2000) and Probasco et al. (2000) reported that IGV differential pressure increased with increasing span locations, Corresponding to the results of Chapter 6,. However, comparisons are limited as only two spanwise locations were experimentally observed in previous experiments.

7.2   CURRENT CONTRIBUTIONS

Several previously conducted investigations provide essential improvements toward understanding rearward forcing in transonic compressors; however, several important aspects of the forcing environment remained unexamined. One such aspects is the effects of a blunt-trailing-edge geometry on IGV surface-pressure response. The current investigation has shows a blunt-IGV (as used by Probasco et al., Koch et al., and Gorrell et al.) exhibits significantly larger unsteady differential-pressure amplitudes and

harmonic content as compared to a sharp-IGV, indicating blunt-IGV surface-pressure results do not accurately represent rotor-induced forcing characteristics of a modern compressor vane. In addition, blunt-IGV base drag results in wake unsteadiness caused creating surface-pressure fluctuations not otherwise present on a sharp-trailing-edge geometry.

In addition, spanwise variations in IGV surface pressure have received little attention. The current investigation indicates rotor-induced forcing of an upstream IGV possesses significant spanwise variation. In general, differential-pressure amplitudes and harmonic content are observed to increase with span, however, the sharp IGV exhibits larger differential-pressure amplitudes near mid-span.

A definitive investigation of IGV trailing-edge pressure "singularities" caused by rearward forcing, as first proposed by Fabian et al., is disputed. First-harmonic differential-pressure results are zero directly at the trailing edge and thus the pressure "singularity" does not occur.

Finally, the current investigation shows a coupled relationship between the unsteady-pressure results and the time-averaged pressure results. This is significant as most analytical unsteady analysis uncouples the mean and perturbation terms, thus solving for the unsteady terms without the influence of time-averaged contributions.

7.3   IMPLICATIONS FOR FUTURE COMPRESSOR DESIGNS

The potential impact of the presented results on turbine engine HCF is manifold. First, IGV geometry plays a central role in vane forcing, suggesting the importance of considering the full, time-averaged, three-dimensional flowfield in turbomachine aerodynamic analysis. Second, strong spanwise vane-forcing variations exist, with these

91

variations dependent on vane geometry, forcing-function strength, and IGV-rotor axial spacing. Three-dimensional vane-forcing analyses are therefore required to include span-dependent higher-order structural modes. Third, the relationship between time-averaged and unsteady flow characteristics suggests a strong coupling that linearized unsteady aerodynamic analysis may not properly model. Finally, since increasing IGV-rotor axial spacing corresponds to both a reduction in vane-forcing amplitude and change in spanwise vane-forcing distribution, fan/compressor designs employing larger axial gaps to reduce forcing levels must consider corresponding spanwise modal forcing changes.

7.4   RECOMMENDATIONS FOR FUTURE WORK

A closer look into the rotor-induced forcing function deserves more attention as this could aid in the understanding of fluid-structure interactions. It is also recommended that a more detailed spanwise analysis be conducted, as only three span locations were observed in the present investigation.

REFERENCES

Anderson, J. D., Jr., 1995, *Computational Fluid Dynamics; The Basics with Applications*, McGraw-Hill, Inc., New York, NY.

Barter, J. W., Vitt, P. H., and Chen, J. P., 2000, "Interaction Effects in a Transonic Turbine Stage," ASME Paper 2000-GT-0376.

Beach, T., 2003, Private Communication, July.

Beam, R. M. and Warming, R. F., 1976, "An Implicit Finite-Difference Algorithm for Hyperbolic Systems in Conservation Law Form," *J. Computer Physics*, Vol. 22, pp. 87-110.

Chen, J. P. and Barter, J., 1998, "Comparison of Time-Accurate Calculations for the Unsteady Interaction in Turbomachinery Stage," AIAA Paper 98-3292.

Chen, J. P. and Briley, W. R., 2001, "A Parallel Flow Solver for Unsteady Multiple Blade Row Turbomachinery Simulations," ASME Paper 2001-GT-0348.

Creason, T. and Baghdadi, S., 1988, "Design and Test of a Low Aspect Ratio Fan Stage," AIAA Paper 88-2816.

Fabian, M. K. and Jumper, E. J., "Rearward Forcing of an Unsteady Compressible Cascade," AIAA *Journal of Propulsion and Power*, Vol. 15, No. 1, pp. 23-30, 1999.

Fabian, M. K., Falk, E. A., and Jumper, E. J., 2001, "Upstream-Propagating Potential Disturbances Interacting with a Compressible Cascade," AIAA *Journal of Propulsion and Power*, Vol. 17, No. 2, pp. 262-269.

Falk, E. A. and Darbe, R. P., 2003, "Numerical Investigation of IGV-Rotor Interactions in a F109 Turbofan Engine," AIAA Paper 03-4981.

Falk, E. A., 2000, "An Experimental Investigation of Aerodynamic Forcing in the F109 Turbofan Engine Compressor," PhD Dissertation, University of Notre Dame.

Garrison, B., 2001, "High Cycle Fatigue (HCF) Science and Technology Program Report", AFRL-PR-WP-TR-20012010, Feb.

Gorrell, S. E., Copenhaver, W. W., and Chriss, R. M., 2001, "Upstream Wake Influences on the Measured Performance of a Transonic Compressor Stage," AIAA *Journal of Propulsion and Power*, Vol. 17, pp. 43-48.

Gorrell, S. E., Okiishi, T. H., and Copenhaver, W. W., 2002a, "Stator-Rotor Interactions in a Transonic Compressor: Part 1 - Effect of Blade-Row Spacing on Performance," ASME *Journal of Turbomachinery*, Vol. 125, pp. 328-335.

Gorrell, S. E., Okiishi, T. H., and Copenhaver, W. W., 2002b, "Stator-Rotor Interactions in a Transonic Compressor: Part 2 - Description of a Loss Producing Mechanism," ASME *Journal of Turbomachinery*, Vol. 125, pp. 336-345.

Koch, P. J., Moran, J., and Wolff, J. M., 1999, "3-D Inlet Guide Vane Generated Vortical Forcing Functions," AIAA Paper 99-2677.

Koch, P. J., Probasco, D. P., and Wolff, J. M., 2000, "Transonic Compressor Influences on Upstream Surface Pressures with Axial Spacing," Technical Note, AIAA *Journal of Propulsion and Power*, Vol. 17, No. 2, pp. 474-476.

Law, C. H. and Wennerstrom, A. J., 1989, "Two Axial Compressor Designs for a Stage Matching Investigation," AFWAL-TR-89-2005.

McCormick, B. W., 1995, *Aerodynamics, Aeronautics, and Flight Mechanics*, Second Edition, John Wiley & Sons, Inc., Hoboken, N.J.

Panovsky, J., James, D. K., Hassan, K. K., 2000, "Assessment of Fan Flutter Using TURBO," Fifth National Turbine Engine High Cycle Fatigue (HCF) Conference, Chandler, A.Z.

Probasco, D. P., Leger, T. J., Wolff, J. M., Copenhaver, W. W., and Chriss, R. M., 2000,"Variations in Upstream Vane Loading With Changes in Back Pressure in a Transonic Compressor," ASME *Journal of Turbomachinery*, Vol. 122, No. 7, pp. 433-441.

Probasco, D. P., Wolff, J. M., Copenhaver, W. W., and Chriss, R. M., 1998, "Axial Spacing Effects in a Transonic Compressor on the Upstream Vane Loading," AIAA Paper 98-3431.

Probasco, D. P., Wolff, J. M., Copenhaver, W. W., and Chriss, R. M., 1997, "Unsteady Blade Row Potential Interaction in a Compression Stage," AIAA Paper 97-3285.

Sanders, A. and Fleeter, S., 1998, "An Experimental Investigation of IGV-Rotor Interactions in a Transonic Axial-Flow Compressor," AIAA Paper 98-3291.

Sanders, A. J. and Fleeter, S., 2000, "Experimental Investigation of Rotor-Inlet Guide Vane Interactions in Transonic Axial-Flow Compressor," AIAA *Journal of Propulsion and Power*, Vol. 16, No. 3, pp. 421-430.

Sanders, A., Papalia, J., and Fleeter, S., 1999, "A PIV Investigation of Rotor-IGV Interactions in a Transonic Axial-Flow Compressor," AIAA Paper 99-2674.

Solomon, W. J., Walker, G. J., and Hughes, J. D., 1999, "Periodic Transition on an Axial Compressor Stator: Incidence and Clocking Effects: Part 2 − Transition Onset Predictions," ASME *Journal of Turbomachinery*, Vol. 121, pp. 408-415.

Turner, M. G., 1996, "Multistage Turbine Simulations with Vortex-Blade Interaction," ASME *Journal of Turbomachinery*, Vol. 188, pp. 643-653.

Turner, M. G., 2003, Private Communication, July.

Van Zante, D. E., 1997, "Study of a Wake Recovery Mechanism in a High-Speed Axial Compressor Stage," NASA CR-1998-206594.

Walker, G. J., Hughes, J. D., and Solomon, W. J., 1999, "Periodic Transition on an Axial Compressor Stator: Incidence and Clocking Effects: Part 1 – Experimental Data," ASME *Journal of Turbomachinery*, Vol. 121, pp. 398-407.

Zhu, J., and Shih, T. H., 1997,"CMOTT Turbulence Module for NPARC," NASA CR 204143; ICOMP-97-10; CMOTT-97-05.

APPENDICES

A   APG TEXT INPUT FILES

Blunt-IGV, Sharp-IGV, and Rotor (default_data.txt)

/---

    This file contains the default griding parameters
        for APG. You can change the default and it will
        override the parameters that are in the APG
        script files.

        NOTE: In the parameters below
        a positive number for spacing is nondimensionalized by
        the span or the chord length, while a negative number
        is in physical units. Axial spacing on the blade is
        only nondimensionalized by the chord length.

/---------- Default Parameters For Axisymmetric Grid --------------------

#DEFINE PRECISION single
#DEFINE REF 1.0   ! reference length
#DEFINE DZ_HUB_IN 0.050   ! axial spacing at the inlet of axi grid near the hub
#DEFINE DZ_HUB_OUT 0.050   ! axial spacing at the outlet of axi grid near the hub
#DEFINE DR_HUB_IN 0.002   ! radial spacing at inlet of axi grid near the hub
#DEFINE DR_HUB_OUT 0.008   ! radial spacing at the outlet of axi grid near the hub
#DEFINE DZ_TIP_IN 0.050   ! axial spacing at the inlet of axi grid near the tip
#DEFINE DZ_TIP_OUT 0.050   ! axial spacing at the outlet of axi grid near the tip
#DEFINE DR_TIP_IN 0.002   ! radial spacing at inlet of axi grid near the tip
#DEFINE DR_TIP_OUT 0.002   ! radial spacing at the outlet of axi grid near the tip
#DEFINE DR_LE 0.002   ! radial spacing at the blade leading edge of axi grid
#DEFINE DR_TE 0.002   ! radial spacing at the blade trailing edge of axi grid
#DEFINE NSPAN 70   ! number of radial
#DEFINE SPANWISE_AXI 1,21,31,41,51,61! spanwise location to perform smoothing of axi grid

/ Data for Blade 1

#DEFINE MNXI 0   ! number of cells in inlet rectifying cell, 0 will set it to 1/2 of
                                        total cell in gap
#DEFINE MDXI 0.0   ! axial grid spacing at inlet rectifying cell, nondimensionalized
                                        by spacing at following trailing edge
#DEFINE MARCI 0.0   ! inlet rectifying cell location along curve between trailing
                                        edge and leading edge(0.5 is midpoint)

#DEFINE NX_I 10   ! number of axial points at the inlet of axi grid
#DEFINE NX_B1 40   ! number of axial points on the blade of axi grid
#DEFINE DS_LE_AXI1 0.004   ! axial spacing at the blade leading edge of axi grid
#DEFINE DS_TE_AXI1 0.004   ! axial spacing at the blade trailing edge of axi grid
#DEFINE OFFSETI11 2   ! grid offset at the inlet of axi grid
#DEFINE OFFSETR11 0.2   ! grid offset at the inlet of axi grid
#DEFINE OFFSET21 -2   ! grid offset at the outlet of axi grid
#DEFINE OFFSETR21 0.2   ! grid offset at the outlet of axi grid
#DEFINE ROOFTOP1 0   ! number of cells in the rooftop
#DEFINE ROOFSIZE1 0.000   ! size of the rooftop as a 46431250f tipclearance
#DEFINE MNXG1 10   ! number of cells before rectifying cell, 0 will set it to 1/2 of
                                        total cell in gap

```
#DEFINE MDXG1 2.                    ! axial grid spacing at rectifying cell, nondimensionalized by
                                      spacing at following trailing edge
#DEFINE MARCG1 0.6453               ! rectifying cell location along curve between trailing edge and
                                      leading edge(0.5 is midpoint)


/ Data for Blade 2

#DEFINE NX_G1 17                    ! number of axial points in gap between b1 & b2
#DEFINE NX_B2 40                    ! number of axial points on the blade of axi grid
#DEFINE NX_O 44                     ! number of axial points at the outlet of axi grid
#DEFINE DS_LE_AXI2 0.004            ! axial spacing at the blade leading edge of axi grid
#DEFINE DS_TE_AXI2 0.004            ! axial spacing at the blade trailing edge of axi grid
#DEFINE OFFSET122 2                 ! grid offset at the inlet of axi grid
#DEFINE OFFSETR12 0.2               ! grid offset at the inlet of axi grid
#DEFINE OFFSET22 -2                 ! grid offset at the outlet of axi grid
#DEFINE OFFSETR22 0.2               ! grid offset at the outlet of axi grid
#DEFINE ROOFTOP2 0                  ! number of cells in the rooftop
#DEFINE ROOFSIZE2 0.000             ! size of the rooftop as a 46431250f tipclearance
#DEFINE MNXO 20                     ! number of cells in outlet rectifying cell, 0 will set it to 1/2 of
                                      total cell in gap
#DEFINE MDXO 8.                     !   axial   grid   spacing   at   outlet   rectifying   cell,
                                      nondimensionalized by spacing at following trailing edge
#DEFINE MARCO 0.300                 ! outlet rectifying cell location along curve between trailing
                                      edge and leading edge(0.5 is midpoint)

/---------- Default Parameters For 3D Grid ---------------------------

/ Data for Blade 1

#DEFINE DS_LE1 0.002                ! axial spacing at the blade leading edge of 3D grid, not used
                                      when leading edge points is >0
#DEFINE DS_TE1 0.002                ! axial spacing at the blade trailing edge of 3D grid
#DEFINE BLADE_POINTS1 80            ! number of axial points on the blade of 3D grid
#DEFINE DSIN1 0.050                 ! axial spacing at the inlet of 3D grid
#DEFINE DSOUT1 0.050                ! axial spacing at the outlet of 3D grid
#DEFINE DTIN1 0.01                  ! tangential spacing at the inlet of 3D grid
#DEFINE DTOUT1 0.0045               ! tangential spacing at the outlet of 3D grid
#DEFINE WALLSPACING1 0.500          ! wall spacing
#DEFINE SPANWISE_3D1 1,7,11,21,31,41,51,61,65,71 ! spanwise location to perform smoothing of 3D
                                      grid
#DEFINE CELLS_THETA1 60             ! number of cells blade to blade
#DEFINE NFRONT1 20                  ! number of cells before the blade in the 3D grid
#DEFINE NBACK1 17                   ! number of cells after the blade in the 3D grid
#DEFINE LEADING_EDGE_POINTS1 10 ! number of blade leading edge points in the 3D grid
#DEFINE TRAILING_EDGE_POINTS1 30 ! number of blade trailing edge points in the 3D grid
#DEFINE TIPCELLS1 8                 ! number of cells in the tip clearance
#DEFINE TIPCLEARANCE1 0.000789474 ! Physical tip clearance
#DEFINE TIPPACKING1 0.2             ! radial spacing intip clearance at blade ndim by clearance
#DEFINE ROOFTOP1 0                  ! number of cells in the rooftop
#DEFINE ROOFSIZE1 0.000             ! size of the rooftop as a % of tipclearance
#DEFINE A_GRAPE1 0.600              ! grape coefficient
#DEFINE B_GRAPE1 0.600              ! grape coefficient
#DEFINE C_GRAPE1 0.600              ! grape coefficient
#DEFINE D_GRAPE1 0.600              ! grape coefficient
#DEFINE DMLE1 0.500                 ! control parameter for L.E cut location
#DEFINE DMTE1 0.900                 ! control parameter for T.E cut location
```

```
#DEFINE LEOFFSET1 0.300           ! control parameter for L.E periodic line
#DEFINE TEOFFSET1 1.000           ! control parameter for T.E periodic line
#DEFINE NUMIT1 200                ! control parameter for number of grape iterations


/ Data for Blade 2

#DEFINE DS_LE2 0.002              ! axial spacing at the blade leading edge of 3D grid, not used
                                    when leading edge points is >0
#DEFINE DS_TE2 0.002              ! axial spacing at the blade trailing edge of 3D grid
#DEFINE BLADE_POINTS2 80          ! number of axial points on the blade of 3D grid
#DEFINE DSIN2 0.050               ! axial spacing at the inlet of 3D grid
#DEFINE DSOUT2 0.050              ! axial spacing at the outlet of 3D grid
#DEFINE DTIN2 0.005               ! tangential spacing at the inlet of 3D grid
#DEFINE DTOUT2 0                  ! tangential spacing at the outlet of 3D grid
#DEFINE WALLSPACING2 0.500        ! wall spacing
#DEFINE SPANWISE_3D2 1,2,3,4,5,11,21,31,41,51,61     ! spanwise location to perform smoothing of
                                    3D grid
#DEFINE CELLS_THETA2 80           ! number of cells blade to blade
#DEFINE NFRONT2 18                ! number of cells before the blade in the 3D grid
#DEFINE NBACK2 90                 ! number of cells after the blade in the 3D grid
#DEFINE LEADING_EDGE_POINTS2 10   ! number of blade leading edge points in the 3D grid
#DEFINE TRAILING_EDGE_POINTS2 20  ! number of blade trailing edge points in the 3D grid
#DEFINE TIPCELLS2 8               ! number of cells in the tip clearance
#DEFINE TIPCLEARANCE2 0.000789474 ! Physical tip clearance
#DEFINE TIPPACKING2 0.015         ! radial spacing intip clearance at blade ndim by clearance
#DEFINE ROOFTOP2 0                ! number of cells in the rooftop
#DEFINE ROOFSIZE2 0.000           ! size of the rooftop as a % of tipclearance
#DEFINE A_GRAPE2 0.600            ! grape coefficient
#DEFINE B_GRAPE2 0.600            ! grape coefficient
#DEFINE C_GRAPE2 0.600            ! grape coefficient
#DEFINE D_GRAPE2 0.600            ! grape coefficient
#DEFINE DMLE2 0.700               ! control parameter for L.E cut location
#DEFINE DMTE2 0.900               ! control parameter for T.E cut location
#DEFINE DELTALECUT2 20.000        ! control parameter for L.E. cut location angle (in deg)
#DEFINE DELTATECUT2 0.000         ! control parameter for T.E. cut location angle (in deg)
#DEFINE LEOFFSET2 0.300           ! control parameter for L.E periodic line
#DEFINE TEOFFSET2 1.000           ! control parameter for T.E periodic line
#DEFINE NUMIT2 400                ! control parameter for number of grape iterations

END OF INPUT
```

B   MSU-TURBO TEXT INPUT FILES

-

Input00.txt

&PARAMETERS
num_blade_rows = 2
debug = F
gofast = T
/

&SOLUTION_PARAMETERS
num_printouts = 1
num_iter_per_printout = 270
max_num_subiter = 6
num_sgs_iter = 3
freeze_jacobian = 0
num_iter_without_fluxfix = 0
num_iter_inviscid = 0
num_iter_first_order = 0
num_iter_restart_write = 270
num_iter_zero_grad_bc = 0
temporal_accuracy = 2
spatial_accuracy = 3
limiter_flag = 1
solution_type = 2
turbulence_model = 5
symmetry_factor=0
trap_negative = F
/

&SLIDING_BC
use_conserve_bc = 0
/

&INITIAL_CONDITION
initialize_solution = 4
/

&REFERENCE_CONDITIONS
ref_length = 0.4826
ref_gamma = 1.401290
ref_pressure = 101325.00
ref_temperature = 288.150
ref_velocity = 287.567
gamma_table = 1.401290 1.401290
temp_gam_table = 288.15 388.15
gamref_t1 = 1.401290
/

&ke_MODEL_PARAMETERS
kemdl_input_type = 0
kemdl_init_option = 0
spatial_accuracy_2eq = 3
temporal_accuracy_2eq = 2
inlet_turbulence_intensity = 0.02
inlet_eddy_viscosity = 10.
use_pgrad_term = F

/

&TIME_SHIFT_BC
time_shift_bc_factor = 0.5
use_time_shift_bc = 1
initialize_time_shift_in_TURBO = T
/

&INLET_BC
inlet_bc_type = -2
/

&EXIT_BC
exit_bc_type = -1
back_pressure = 117243.27934
/

&FLUTTER
/

&TIME_STEP
cfl = 0.0
use_local_time_step = 0
num_time_steps_per_period = 270
omega_ts = -13509.0
num_blds_ts = 33
/

&OUTPUT
num_soln_per_flow_file = 3
num_iter_per_soln_dump = 9
output_format = 1
/

&INLET_PROFILE
span =
0.000685233
0.002739052
0.006155830
0.010926200
0.017037087
0.024471742
0.033209787
0.043227271
0.054496738
0.080664716
0.111427019
0.146446609
0.185339804
0.227680482
0.273004750
0.320816025
0.370590477
0.421782767
0.473832022
0.526167978

0.578217233
0.629409523
0.679183975
0.726995250
0.772319518
0.814660196
0.853553391
0.888572981
0.919335284
0.933012702
0.945503262
0.956772729
0.966790213
0.975528258
0.982962913
0.989073800
0.993844170
0.997260948
0.999314767

total_pressure =
86614.79847
89940.10803
92625.07588
94911.93001
96876.55497
98539.31041
99891.95562
100904.8672
101525.5682
101684.2879
101684.2879
101684.2879
101684.2879
101684.2879
101684.2879
101684.2879
101684.2879
101684.2879
101684.2879
101684.2879
101684.2879
101684.2879
101684.2879
101684.2879
101684.2879
101684.2879
101684.2879
101684.2879
101684.2879
101476.4004
100551.563
99028.76147

```
96994.19349
94475.3091
91422.43561
87588.80382

total_temperature =
39*288.15

tangential_angle =
39*0.0

radial_angle =
39*0.0

turbulence_intensity =
39*0.02

turbulence_length_scale =
39*0.001
/

&EXIT_PROFILE
/
```

Input01.txt

```
&BLADE_ROW_PARAMETERS
num_blades = 24
omega_bld = 0.0000
num_time_steps_stored = 100
num_adjacent_blades = 33
suction_surface = 2
use_wall_func_j = 1
use_wall_func_k = 1
transition = 0.001
x_start_hub_rotation = -9999.0
x_end_hub_rotation = -9999.0
x_start_case_rotation = 9999.0
x_end_case_rotation = 9999.0
//
```

Input02.txt

```
&BLADE_ROW_PARAMETERS
num_blades = 33
omega_bld = -13509.0000
num_time_steps_stored = 100
num_adjacent_blades = 24
suction_surface = 2
use_wall_func_j = 1
use_wall_func_k = 1
transition = 0.01
x_start_viscous_hub = -9999.0
```

```
x_start_viscous_case = -9999.0
x_start_hub_rotation = -0.00128511960404
x_end_hub_rotation = 9999.0
x_start_case_rotation = 9999.0
x_end_case_rotation = 9999.0
/
```

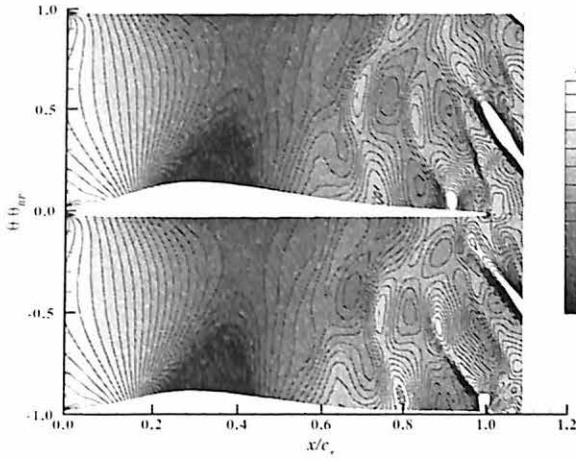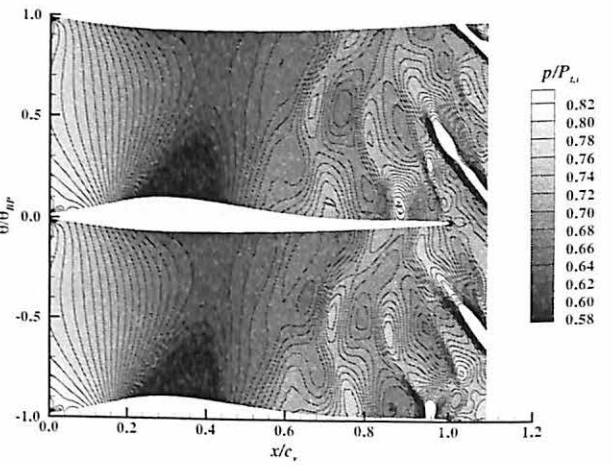# C INSTANTANOUS STATIC-PRESSURE CONTOURS

-
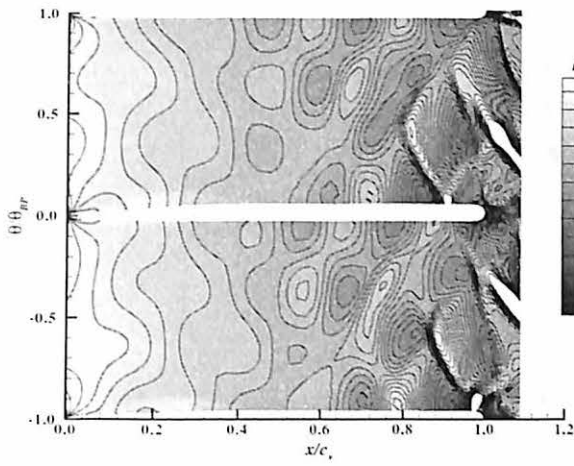
Figure C- 1 IGV Static-Pressure Contours:
Blunt-Close, 75% Span, $t = 0$.
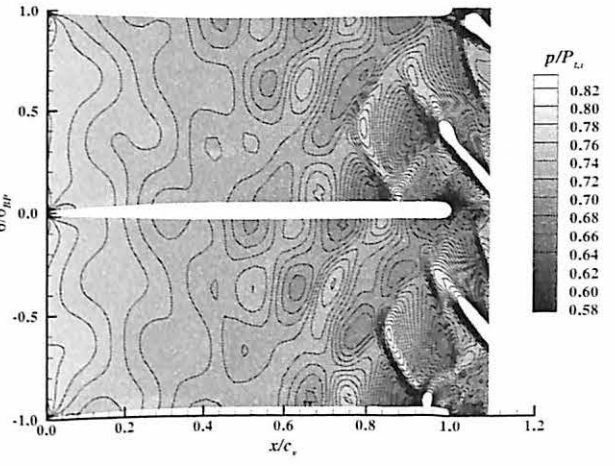
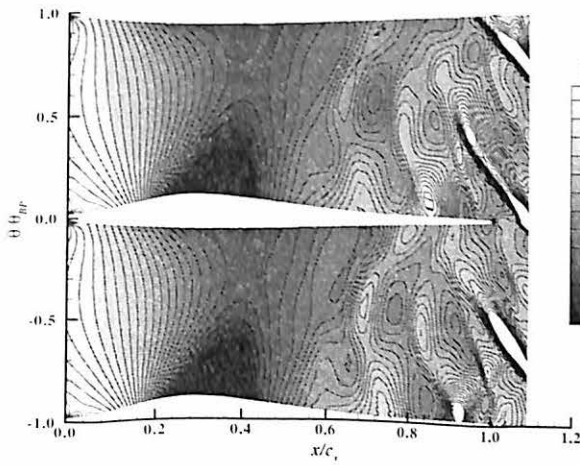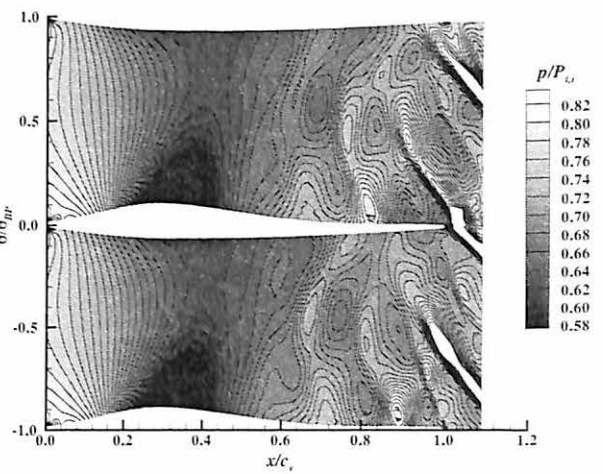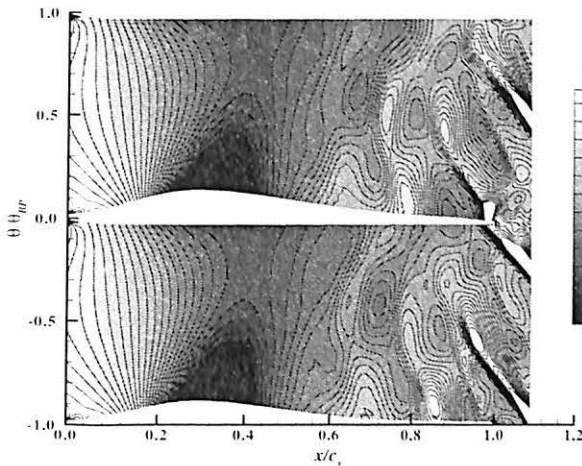**Figure C- 2 IGV Static-Pressure Contours:**
Blunt-Close, 75% Span, $t = T/6$.
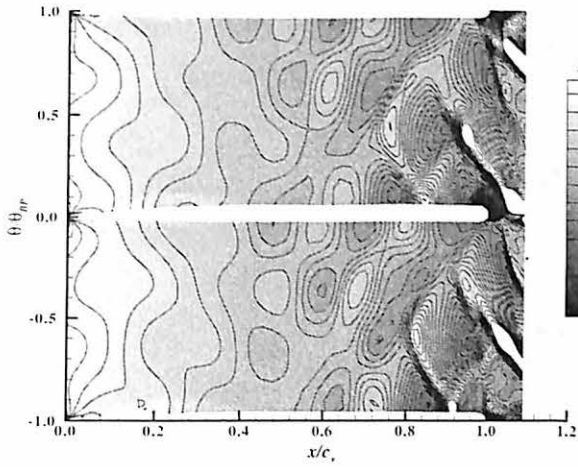
Figure C- 3 IGV Static-Pressure Contours:
Blunt-Close, 75% Span, $\underline{t} = T/3$.
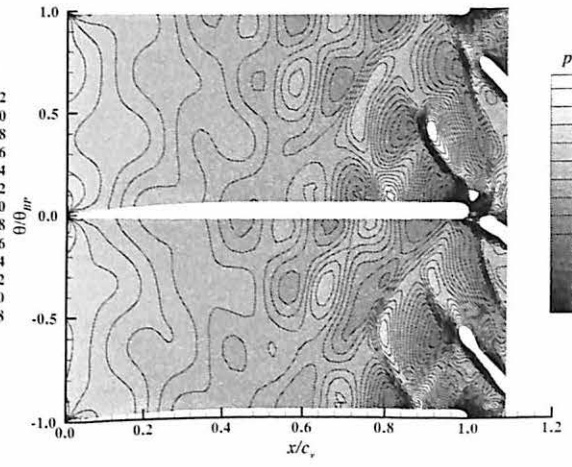
Figure C- 4 IGV Static Pressure Contours:
Blunt-Close, 75% Span, $t = T/2$.
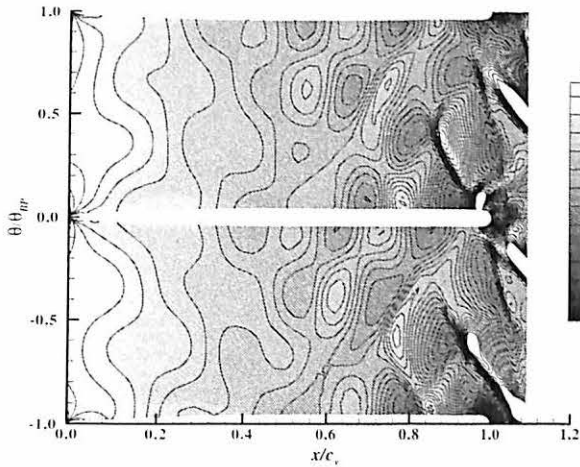
Figure C- 5 IGV Static-Pressure Contours:
Blunt-Close, 75% Span, $t = 2T/3$.
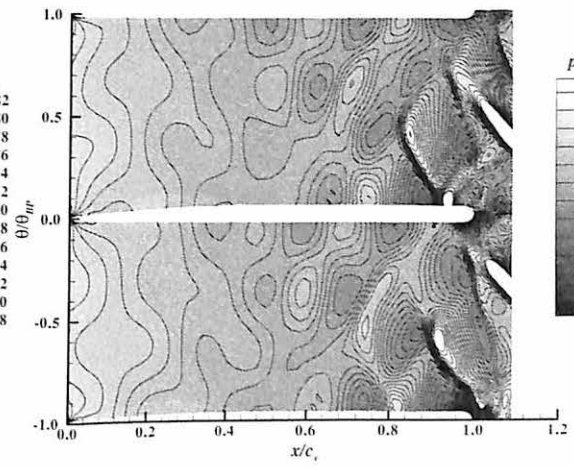
Figure C- 6 IGV Static-Pressure Contours:
Blunt-Close, 75% Span, $t = 5T/6$.

109
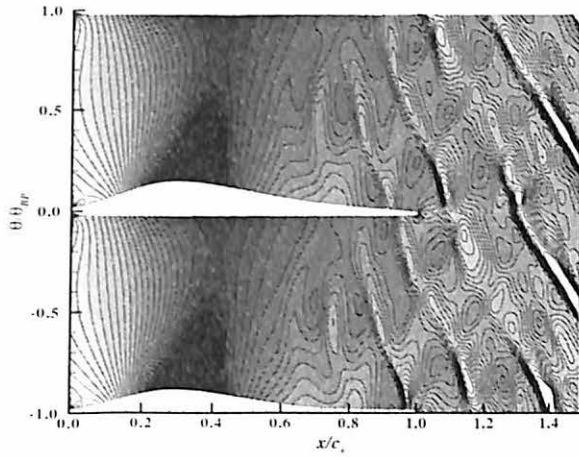
Figure C- 7 IGV Static-Pressure Contours: Sharp-Far, 75% Span, $t = 0$.
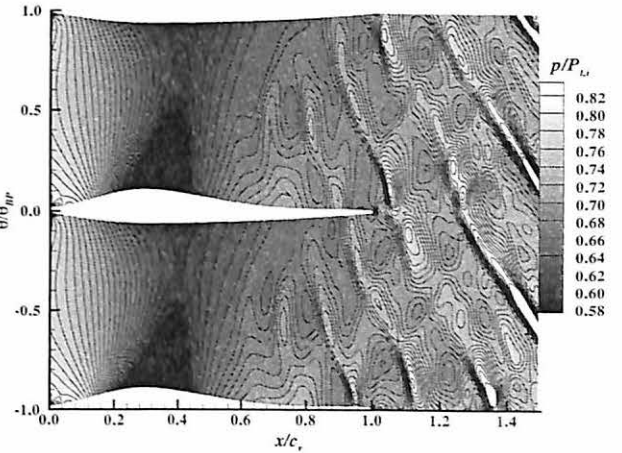
Figure C- 8 IGV Static-Pressure Contours: Sharp-Far, 75% Span, $t = T/6$.
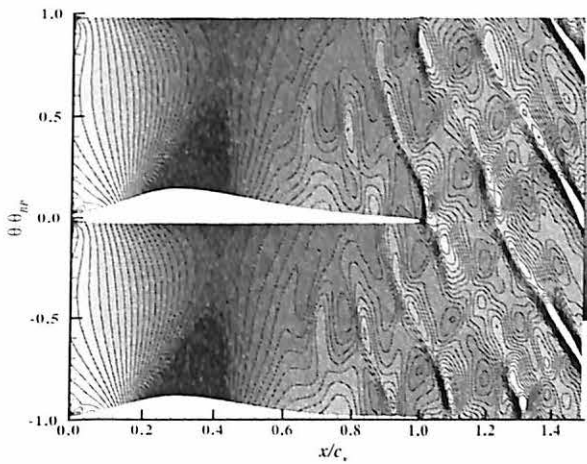
Figure C- 9 IGV Static-Pressure Contours: Sharp-Far, 75% Span, $t = T/3$.
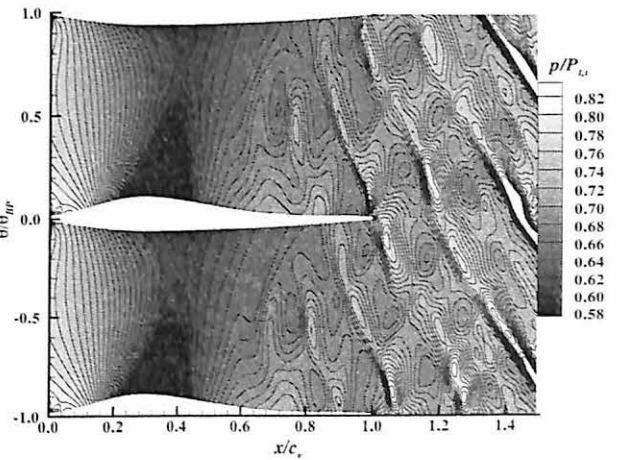
Figure C- 10 IGV Static-Pressure Contours: Sharp-Far, 75% Span, $t = T/2$.
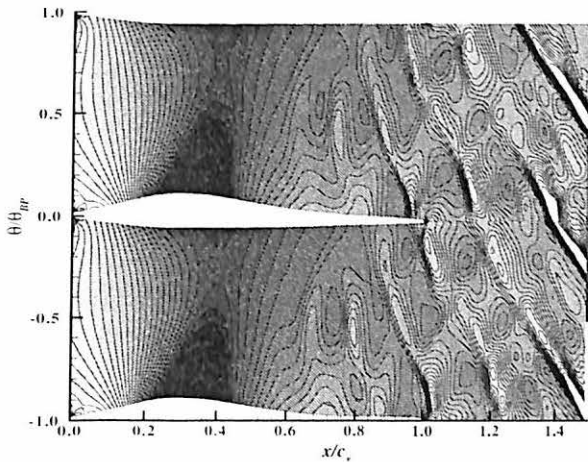
Figure C- 11 IGV Static-Pressure Contours: Sharp-Far, 75% Span, $t = 2T/3$.
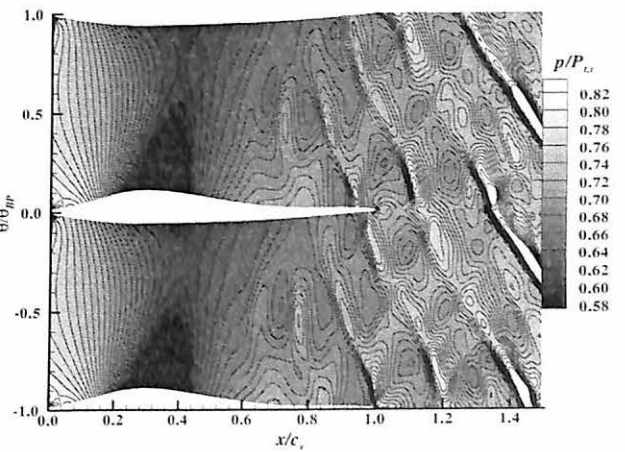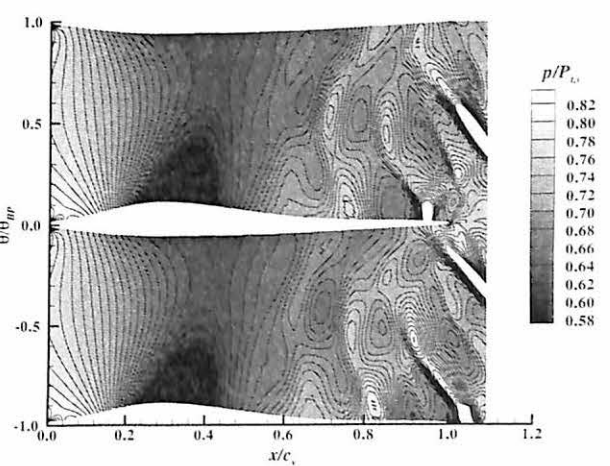

Figure C- 12 IGV Static-Pressure Contours: Sharp-Far, 75% Span, $t = 5T/6$.

110

Figure C- 13   IGV Static-Pressure Contours:
Sharp-Close, 75% Span, $t = 0$.

Figure C- 14⁻ IGV Static-Pressure Contours:
Sharp-Close, 75% Span, $t = T/6$.

Figure C- 15   IGV Static-Pressure Contours:
Sharp-Close, 75% Span, $t = T/3$.

Figure C- 16   IGV Static-Pressure Contours:
Sharp-Close, 75% Span, $t = T/2$.

Figure C- 17   IGV Static-Pressure Contours:
Sharp-Close, 75% Span, $t = 2T/3$.

Figure C- 18   IGV Static-Pressure Contours:
Sharp-Close, 75% Span, $t = 5T/6$.

111

D   IGV INSTANTANOUS DIFFERENTIAL PRESSURE
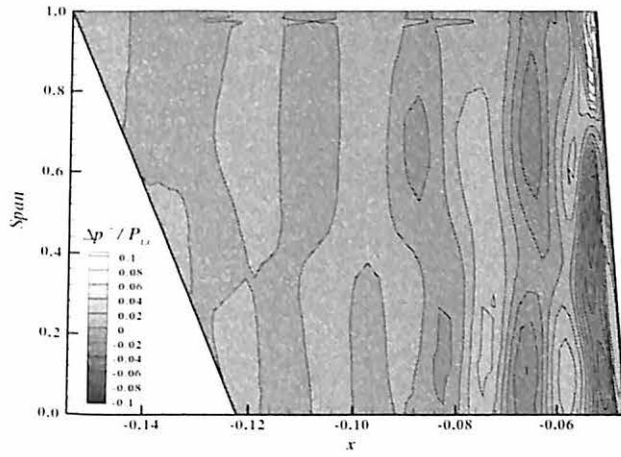
CONTOURS

**Figure D- 1   IGV Static-Pressure Contours:
Blunt-Far, $t = 0$.**
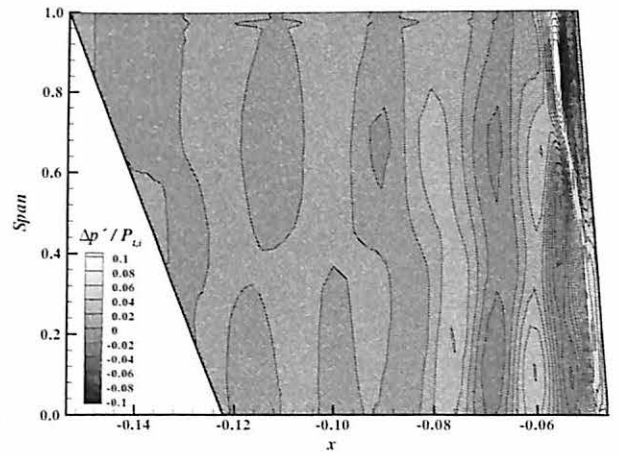
**Figure D- 2   IGV Static-Pressure Contours:
Blunt-Far, $t = T/6$.**
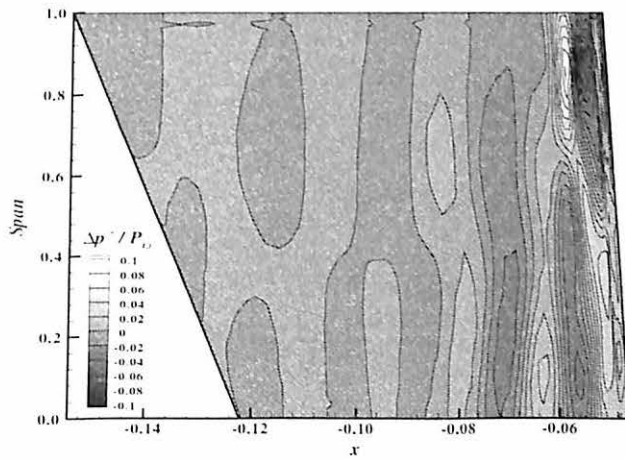
**Figure D- 3   IGV Static-Pressure Contours:
Blunt-Far, $t = T/3$.**
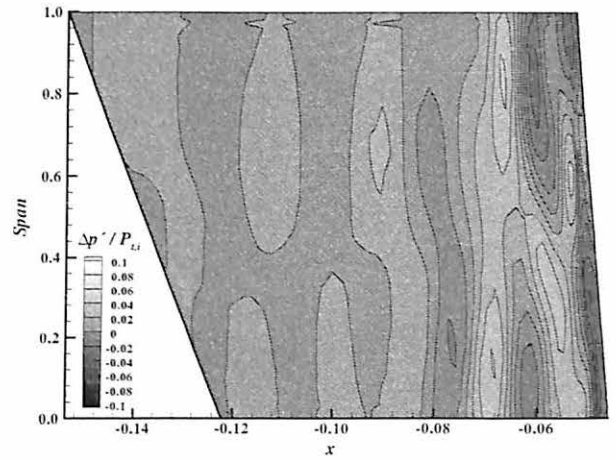
**Figure D- 4   IGV Static-Pressure Contours:
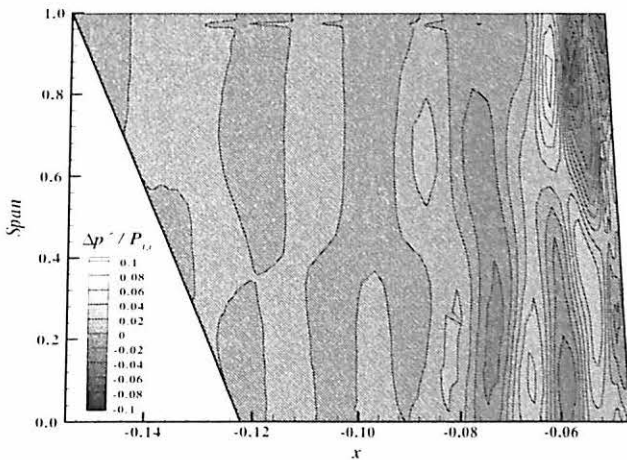Blunt-Far, $t = 2T/3$.**

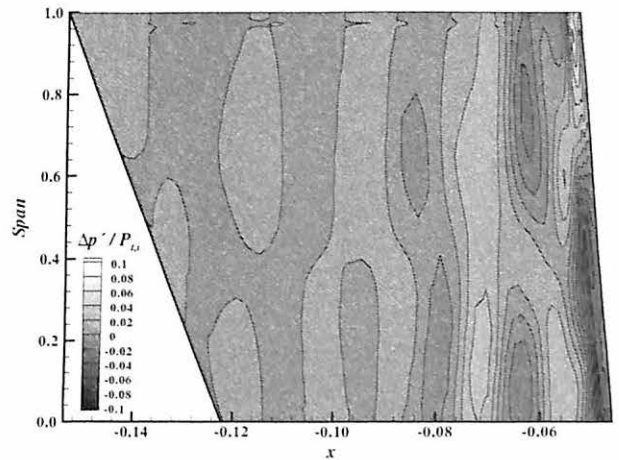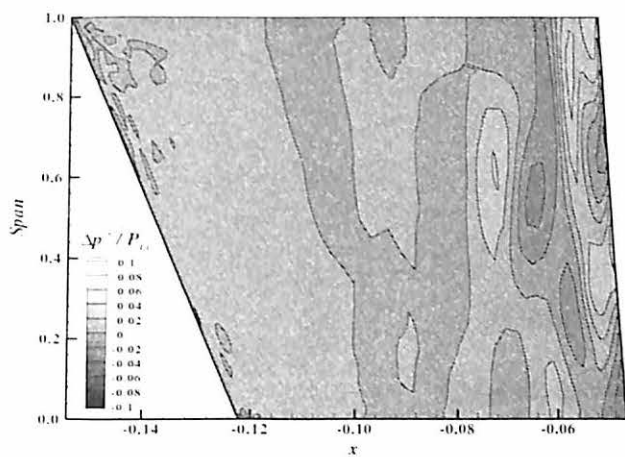**Figure D- 5   IGV Static-Pressure Contours:
Blunt-Far, $t = T/2$.**

**Figure D- 6   IGV Static-Pressure Contours:
Blunt-Far, $t = 5T/6$.**

113

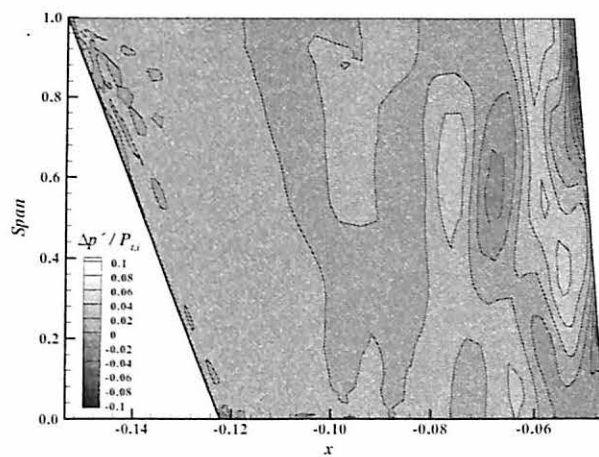**Figure D- 7** IGV Static-Pressure Contours:
Sharp-Far, $t = 0$.

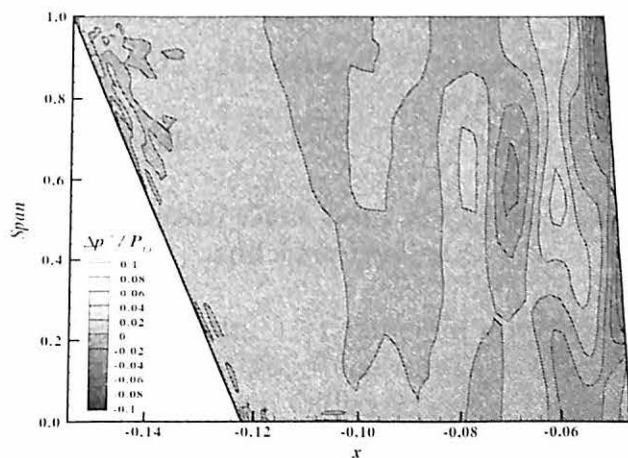**Figure D- 8** IGV Static-Pressure Contours:
Sharp-Far, $t = T/6$.

Figure D- 9 IGV Static-Pressure Contours:
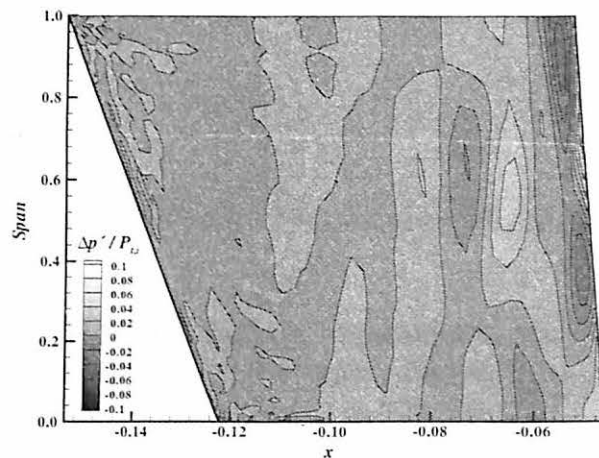Sharp-Far, $t = T/3$.

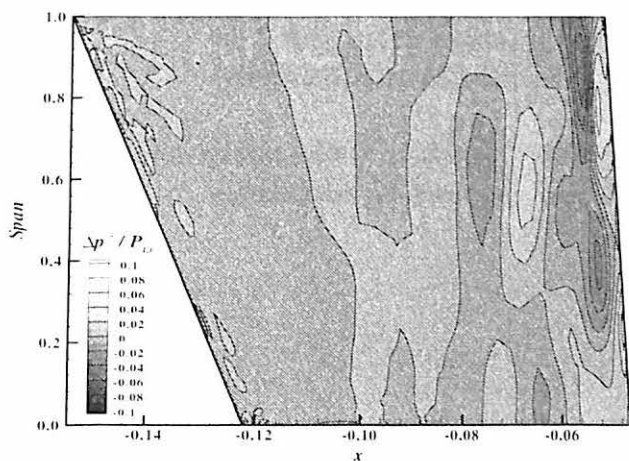**Figure D- 10** IGV Static-Pressure Contours:
Sharp-Far, $t = 2T/3$.

Figure D- 11 IGV Static-Pressure Contours:
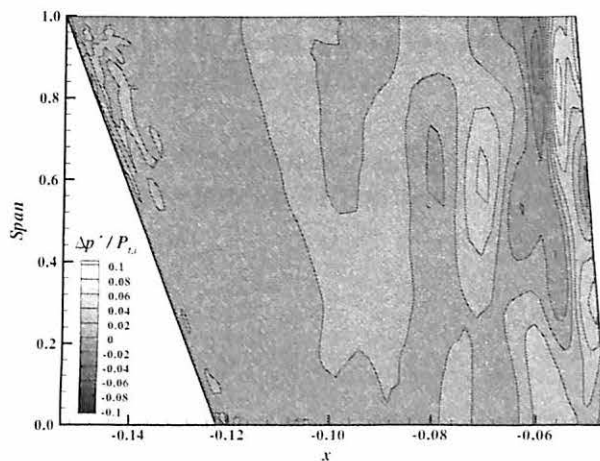Sharp-Far, $t = 2T/3$.

Figure D- 12 IGV Static-Pressure Contours:
Sharp-Far, $t = 5T/6$.

114

Vita

Robert Phillip Darbe

Candidate for the Degree of

Master of Science

Thesis: INFLUENCE OF TRAILING-EDGE GEOMETRY ON IGV FORCED RESPONSE IN A TRANSONIC COMPRESSOR

Major Field: Mechanical Engineering

Biographical:

Personal Data: Born in Edmond, Oklahoma on April 15, 1980, the son of Kimball and June Darbe

Education: Graduated from Guthrie high School, Guthrie, Oklahoma in May 1998. Received a Bachelor of Science degree in Aerospace Engineering from Oklahoma State University, Stillwater, Oklahoma in May 2002. Completed the requirements for the Master of Science degree with a major in Mechanical Engineering at Oklahoma State University in July 2004.

Experience: Employed by Fluid Engineering Services as a Laboratory Technician from 2000 to 2002. Employed by Oklahoma State University as a Research Assistant and Teaching Assistant in the Department of Mechanical and Aerospace Engineering from 2002 to 2004.

Professional Memberships: American Society of Mechanical Engineers, American Institute of Aeronautics and Astronautics, Pi Tau Sigma.